論文 / 著書情報
Article / Book Information

題目(和文)	フィラメント状分子雲の重力収縮と分裂: 等温の崩れと二次元性の顕在化
Title(English)	Gravitational Contraction and Fragmentation of Filamentary Molecular Clouds: Breakdown of Isothermality and Appearance of Two-Dimensionality
著者(和文)	鐵紘由紀
Author(English)	Hiroyuki Tetsu
出典(和文)	学位:博士(理学), 学位授与機関:東京工業大学, 報告番号:甲第10074号, 授与年月日:2016年3月26日, 学位の種別:課程博士, 審査員:中本 泰史,綱川 秀夫,井田 茂,野村 英子,佐藤 文衛
Citation(English)	Degree:Doctor (Science), Conferring organization: Tokyo Institute of Technology, Report number:甲第10074号, Conferred date:2016/3/26, Degree Type:Course doctor, Examiner:,,,,
学位種別(和文)	博士論文
Type(English)	Doctoral Thesis

Gravitational Contraction and Fragmentation of Filamentary Molecular Clouds: Breakdown of Isothermality and Appearance of Two-Dimensionality

Department of Earth and Planetary Sciences

Hiroyuki Tetsu

ABSTRACT

Observations favour a theoretical scenario in which fragmentation of radially contracting filaments takes place due to the breakdown of isothermality. On the other hand, although the filament formation and fragmentation of static filaments have been studied in detail, there is a theoretical gap between the radially contracting filament and the fragmentation. The purpose of this work is to fill and understand the theoretical gap in the context of uncovering the role of radiative transfer.

First, in order to study the role of radiation in the radially contracting filaments, we perform radially one-dimensional radiation hydrodynamics (RHD) calculations with variable Eddington factor (VEF) method. The similar calculations have been performed; however, the analysis is insufficient and there are some problems in the numerical approach and assumed initial conditions. As a result of our careful calculations and detailed analysis, the critical density, which is analytically presented by Masunaga & Inutsuka (1999), and at which the isothermality is expected to break down, is confirmed qualitatively. However, we also find that the "break down of isothermality" is not instantaneous and when fragmentations appear cannot be known by only one-dimensional simulations. Therefore, in order to understand the fragmentation process, two-dimensional RHD calculations are needed. The VEF method is too computationally expensive to perform multi-dimensional RHD calculations; thus flux-limited diffusion (FLD) approximation, which is computationally lower-cost, should be chosen. However, the traditional numerical approach based on the Newton-Raphson (NR) method has a computational drawback of the stability especially in the optically thin regime. Therefore, as the second step, four schemes for implicitly solving for the nonlinear simultaneous equations in the RHD equations with FLD, namely the NR method, simply operator splitting (SOS), modified operator splitting presented by Douglas & Rachford (1956) (DROS), and linearizing the Planck function (LIN). From some numerical tests, we find that DROS and LIN can be chosen as the alternative scheme. Third, using DROS, we perform two-dimensional RHD calculations with the FLD approximation to investigate the fragmentation process of radially contracting filamentary clouds. As a result, we find when the fragmentation occurs, which cannot be determined by one-dimensional approaches. We define the criteria for judging the appearance of two-dimensionality using the mean central density, which was approximately one order of magnitude higher than previous implicit understandings. The density when fragmentations appear is corresponding to several Jupiter mass, which is several times smaller than previously predicted. The mass is in agreement with planet mass objects observed using the microlensing effect and the candidates of the first hydrostatic cores observed by ALMA along filamentary clouds.

Our work uncovers the role of radiative transfer in the process of the contraction and the fragmentation of filamentary clouds. The neglected main factors, namely magnetic field, turbulence, and the rotation of filaments, generally support the radial structure of filaments; thus, the estimated mass is expected as the minimum value that can be formed from the filamentary molecular clouds. Based on the knowledge, the formation process of real astronomical objects, e.g., stars, brown dwarves, planetary mass objects, etc., along the filamentary structures in molecular clouds should be understood.

ACKNOWLEDGMENTS

I would like to thank my supervisor, Professor Taishi Nakamoto, for his fruitful advice. I would also like to thank members of our laboratories (Nakamoto Laboratory, Ida Laboratory, Makino Laboratory, Sato Laboratory, Nomura Laboratory, and Okuzumi Laboratory). I am grateful to all staff members, secretaries, and students in our department for their support and assistance. Finally, and foremost, I would really like to appreciate my family's support for 29 years.

Contents

List of Figures

List of Abbreviations

CFL
: Courant–Friedrichs–Lewy (condition)

CMF
: Core Mass Function

DROS
: Douglas & Rachford Operator Splitting (scheme)

FLD
: Flux-Limited Diffusion (approximation, method)

HD
: HydroDynamics

IMF
: Initial Mass Function

LTE
: Local Thermodynamic Equilibrium

LIN
: Linearization (scheme)

MHD
: Magneto-HydroDynamics

NR
: Newton–Raphson (scheme, method)

OS
: Operator Split, Operator Splitting (scheme)

RHD
: Radiation HydroDynamics

RMHD
: Radiation Magneto-HydroDynamics

SPH
: Smoothed Particle Hydrodynamics

SOS

Simple Operator Splitting (scheme)

VEF

Variable Eddington Factor (method)

VTEF

Variable Tensor Eddington Factor (method)

Glossary of Physical Symbols

a

radiation energy constant ($4\sigma/c$)

B

frequency-integrated Boltzmann function

B_ν

frequency dependent Boltzmann function

c

speed of light

C

complex Fourier constant

c_v

heat capacity at constant volume per unit volume

c_s

speed of sound

D

diffusion constant defined in RHD theory

e

gas internal energy density per unit volume

E

radiation energy density per unit volume

E_ν

frequency dependent radiation energy density per unit volume

$\boldsymbol{F}$

frequency-integrated radiation energy flux

$\boldsymbol{F}_\nu$

frequency dependent radiation energy flux

G

constant of gravitation

h
: model parameter ($= \sqrt{m/m_{\mathrm{crit}}}$)

H
: scaleheight of a filament

k_{B}
: Boltzmann constant

m
: line mass (mass of a filament per unit length)

m_{eq}
: line mass of an isothermal filament in dynamical equilibrium

m_{crit}
: critical line mass

m_{H}
: atomic mass unit

M_{frag}
: mass of fragments

M_{sun}
: mass of sun

$M_{\odot}$
: mass of sun

$\mathbf{P}$
: frequency dependent radiation pressure tensor

R
: gas constant

T
: gas temperature

T_{B}
: radiation temperature of background radiation field

T_c

gas temperature at center of a filament

T_{gas}

gas temperature

T_{rad}

radiation temperature

v

speed of fluid

$\boldsymbol{v}$

velocity of fluid

β

model parameter (dependency of opacity on temperature)

γ

specific heat ratio

γ_p

polytropic index

γ_{crit}

critical polytropic index

Γ

heating rate per unit mass

Λ

cooling rate per unit mass

κ

frequency-integrated opacity per unit volume

κ_{E}

energy mean opacity per unit volume

κ_{F}

flux mean opacity per unit volume

κ_{P}

Planck mean opacity per unit volume

κ_{R}

Rosseland mean opacity per unit volume

κ_ν

frequency dependent opacity per unit volume

μ

mean molecular weight

ν

frequency

χ

frequency-integrated mass opacity

χ_{E}

energy mean mass opacity

χ_{F}

flux mean mass opacity

χ_{P}

Planck mean mass opacity

χ_{R}

Rosseland mean mass opacity

χ_ν

frequency dependent mass opacity

χ_{10}

frequency-integrated mass opacity at 10 K

ρ

mass density of fluid

ρ_c

mass density of fluid at center of a filament

$\rho_{\rm frag}$
: mass density of fluid at center of a filament when fragmentation occurs

$\rho_{\rm crit}$
: critical mass density

$\rho_{\rm crit}^{\rm Rad}$
: critical mass density (radiation heated)

$\rho_{\rm crit}^{\rm CR}$
: critical mass density (cosmic ray heated)

ρ_{τ}
: mass density of fluid at center of a filament at which $\tau = 1$

σ
: Stephan–Boltzmann constant

τ
: optical thickness of a filament

Φ
: gravitational potential energy

Chapter 1

GENERAL INTRODUCTION

1.1 Filamentary Molecular Clouds

From many years ago to recent days, in order to understand the process of star formation, many authors assume spherical geometry and uncover it precisely (e.g., Larson, 1969; Tomida et al., 2013). However, based on both observational and theoretical researches, the more realistic condition seems to be filamentary structures in molecular clouds. Based on the observational facts, e.g., the core mass function (CMF) is similar to the initial mass function (IMF) (Könyves et al., 2010), to understand the fragmentation process of filamentary structures are indispensable to understand the early stage of star formation.

Herschel space observatory have found that the omnipresent filamentary structures in filamentary molecular clouds are the site of low-mass star formations (André et al., 2010, 2014). On the other hand, there is a theoretical scenario to explain the on-the-filament star formation. According to the scenario, a sparse molecular cloud does not globally contract to a point, but locally collapse into a lot of cores. The clouds collapse into sheet-like structures, and the sheets fragment into filamentary structures, and finally the filaments fragment into spherical objects (Miyama et al., 1987a,b; Pon et al., 2011), which corresponds to so-called hydrostatic "first cores."

The formation process of filamentary structures are still on the controversy, e.g., even if the gravity does not work in an isothermal gas, one-dimensional collision of parental clouds trigger the Kelvin–Helmholtz instability and a nonlinear bending, and then filamentary structures are formed (Klein & Woods, 1998). The dissipation of the super sonic turbulence can also create filaments (Padoan et al., 2001). Among them, motivated by the observations (e.g., Palmeirim et al., 2013), the hypothesis that the magnetic fields and the gravitational instability affect the formation process of filaments, may be preferred (André et al., 2014).

In the present paper, we do not consider the formation processes of filaments precisely. We follow the scenario based on gravitational instability and assume gravitationally unstable filaments as initial conditions. This assumption is consistent to the observational fact that the filaments that have prestellar cores and young stellar objects (YSOs), always has enough mass to gravitationally collapse (corresponds to Jeans mass in spherical geometry) (Arzoumanian et al., 2011).

1.2 Radial Contraction of Filamentary Clouds

Many researchers have uncovered the radial contraction of filaments. The approaches are roughly decided into two method: the analytical one and the numerical one.

Adopting some simplification, the self-similar solutions can be obtained analytically (e.g., Hennebelle, 2003; Tilley & Pudritz, 2003; Kawachi & Hanawa, 1998; Shadmehri & Ghanbari, 2001; Holden et al., 2009). In this approach, assuming the polytropic relation, the gravitational radial contraction of filaments have been investigated involving various processes, e.g., the magnetic field, the turbulence, the rotation, and the change of the equation of state, end so forth. This method is extremely effective to understand the essence of the processes, however, cannot deal with the isothermal firmaments well.

The other is to perform numerical simulations (e.g., Tomisaka, 1995; Nakamura, 1998; Nakamura et al., 1999; Ogochi, 2000). Among them, Ogochi (2000) perform one-dimensional RHD calculations and investigate the switch from the isothermal collapse to the semi-adiabatic one. For filamentary clouds the break down of isothermality is critical as the turning point of dynamics, thus their work has an important meaning.

An interesting fact is shown by Inutsuka & Miyama (1992). The gravitationally unstable and isothermal filaments cannot fragment, because the timescale of the fragmentation is much shorter than the timescale of the radial contraction. To fragment into cores, the isothermality of filaments must break down by any factors (see appendix G).

1.3 Fragmentation of Molecular Clouds

According to the stability analysis, which is similar to so-called the analysis of Jeans, the static filament fragments because of the gravitational instability. The length of fragments is also about the Jeans length. Even if the effects of the magnetic field, the rotation, and the turbulence, the fragmentation process are not affected strongly

(Larson, 1985; Inutsuka & Miyama, 1992; Gehman et al., 1996a,b; Matsumoto et al., 1994; Nagasawa, 1987; Nakamura et al., 1993). An isothermal filament, which has enough mass and is gravitationally contracting, does not fragment because the timescale of the radial contraction is much shorter than one of the fragmentation (Inutsuka & Miyama, 1992) because of the geometrical characteristics. In other words, if the filaments are isothermal and gravitationally contracting, filaments does not fragment, namely the two-dimensionality does not appear.

Numerical approaches have been also developed. The works assuming isothermal gas (Inutsuka & Miyama, 1997), the magnetic field (e.g., Tomisaka, 1995), the rotation (Matsumoto et al., 1997), etc. have been performed. The results are roughly speaking consistent to analytical predictions.

As shown above, if the radial contraction is sufficiently moderate, the fragmentation processes have been investigated in detail.

1.4 Theoretical Gap

The radial gravitational contraction of filamentary clouds continue forever unless the isothermality is broken down by any factors. The main factor that maintains the isothermality of filaments is radiation (radiative transfer and thermal emission/absorption). Thus, the RHD manner is needed to investigate the dynamics of filaments in detail.

Ogochi (2000) performed one-dimensional RHD calculation to investigate the evolution of the dynamics of gravitationally contracting filaments. Their idea is meaningful to fill a gap, namely the function of radiation in radially contracting filaments. However, their work involves some problems. First, indeed they perform a series of calculations, but they does not examine and discuss the results. Second, they choose Lagrange method for hydrodynamics; thus, their calculations cannot resolve the detailed structures, e.g., a shock wave front formed in the inner envelope (shown in chapter 2). Third, they does not distinguish the real dynamics to an artificial one (see appendix H), which is artificially caused and is dependent on the initial condition.

Additionally, their calculation is restricted processes to one-dimensional. Various information, e.g., when the isothermality breaks down, how the deceleration occurs, and so on. However, it is not clear that when the two-dimensionality, namely fragmentation processes, appears. The answer of the question can be given by two-dimensional calculations. Such two-dimensional calculations are performed assuming isothermal gas (Inutsuka & Miyama, 1997), primordial gas (Nakamura & Umemura, 2001), and so forth: however, those including radiative transfer have never performed. Therefore, to uncover the fragmentation process precisely, two-dimensional RHD calculations are needed.

1.5 Purpose of This Work

The purpose of this work is to consistently understand the processes of the radial contraction and the fragmentation of filamentary molecular clouds, focusing on the radiative transport.

In order to achieve the purpose, we investigate the one-dimensional contraction of filamentary clouds in detail. The idea was originally proposed by Ogochi (2000), and advanced by us using detailed calculations and considerations. The results are shown in chapter 2.

To understand the fragmentation processes more precisely, we should perform two-dimensional RHD calculations. However, there are numerical difficulties to perform RHD calculations for the collapse of filaments, which includes extremely optically thin regions. To avoid the difficulties, we compare some schemes to solve RHD equations and choose more appropriate one. This attempt and the result has an important meaning for general algorithm of RHD; thus, we show the details in chapter 3.

And then, we compose an efficient RHD algorithm. Using the code, we perform two-dimensional RHD calculations to investigate the process of the appearance of two-dimensionality during radial collapse of filaments. The work is described in chapter 4.

The existence of the magnetic field, the turbulence, the rotation, etc. influence on the dynamics of radially contracting filaments (e.g., Larson, 1985; Tomida et al., 2013). Nevertheless, though the all of this paper, we ignore such processes to extract an interesting process, namely the relation radiative transfer and the dynamics.

Chapter 2

RADIAL CONTRACTION

2.1 Introduction

Many authors have investigated the radial contraction of filamentary clouds. The approaches can be divided into the analytical one (e.g., Hennebelle, 2003; Holden et al., 2009; Kawachi & Hanawa, 1998; Shadmehri & Ghanbari, 2001; Tilley & Pudritz, 2003) and the numerical one (e.g., Nakamura, 1998; Nakamura et al., 1999; Ogochi, 2000).

From these works, it is uncovered that the isothermality is extremely critical. If filaments contract isothermally, they can collapse into infinitely thin and dense lines. The collapse is not so-called run-away that appears in spherical gas, but semi-static one, in which the gravitational force nearly balances with the pressure divergence force. On the other hand, if the isothermality breaks down, the contraction is rapidly decelerated. This is remarkable feature in contrast to spherical clouds. Therefore, is is important to consider the radiative transfer, which is essential process that keeps filaments isothermal, to investigate the radial contraction of filamentary clouds. See also appendix G for the more detailed explanation.

Masunaga & Inutsuka (1999) investigate the break down of isothermality assuming filamentary geometry. They roughly estimate dominant heating and cooling rate and obtain the "critical density" at the center of filaments, above the value the isothermality of filaments break down. Their estimation is valuable to understand the process and to predict when isothermality breaks down. However, the specific evolution of the structure of filaments is too complicated to be understood using analytical approaches.

Ogochi (2000) investigated the radial contraction of filaments using RHD simulations with VEF method (Stone et al., 1992). They performed some calculations and presented interesting implications; however, there were some problems: the low resolution, the lack of consideration to the evolution, the confusion of real "bounce" and artificial "isothermal bounce" (in detail, see this chapter and appendix H).

Based on their idea, we perform one-dimensional RHD calculations of radially contracting filaments in detail. Sufficient space resolution and deep insights uncover the dynamics of filaments that strongly depend on radiative transfer.

In this study, we employ the Variable Eddington Factor (VEF) method (Stone et al., 1992), which ensures the correct treatment of the radiative energy transfer in any optical depth medium. This property of the method is essentially desirable for our purpose because the critical density is sensitively dependent on the radiation transfer process and the optical depth.

2.2 Model

2.2.1 Gas and Dust Grains

The equation of gas is assumed as bellows. Cooling processes by radiative emission from molecular and atomic gases in the star forming clouds are less effective than that by the thermal emission from dust grains when the gas density $\rho > 10^{-19}$ g cm^{-3} (Goldsmith & Langer (1978); Nakamura (1998)), so we do not pay our attention on the chemical composition of the gas. Chemical reactions are not taken into account and the mean molecular weight, μ, is fixed to be 2.3. Also, the ratio of specific heats, γ, is fixed to be 5/3, since the rotational degrees of freedom of hydrogen molecules are not excited in the low temperature cloud in which the gas temperature is typically less than 100 K. Thus, the gas is considered to be ideal. The gas internal energy per unit volume, e, is given by $c_v T$, where c_v is the heat capacity at constant volume per unit volume. The gas pressure is given by the equation of state for ideal gas, $p = (\gamma - 1)e$. We can consider that the gas and dust grains are thermally coupled sufficiently and they have the same temperature (Goldsmith & Langer, 1978), since the cloud density is high enough (typically $\rho > 10^{-19}\,\mathrm{g\,cm^{-3}}$). Therefore, we regard the gas that involve dust grains as a radiating fluid, whose temperature is represented by T. Since the temperature of dust considered in our simulations is lower than 100 K, the radiation energy is localized in a frequency region $\nu \lesssim 10^{13}$ Hz. For the radiation in that frequency region, the mass opacity of dust grains is given by the Rayleigh-Jeans limit case; the frequency dependent mass opacity, χ_ν, is proportional to the frequency ν as $\chi_\nu \propto \nu^\beta$ where β is the power law index. Then, the Planck mean mass opacity, χ_P, which is defined using the Planck function $B_\nu(T)$ by $\chi_\mathrm{P} \equiv \int_0^\infty \chi_\nu B_\nu(T)\,d\nu / \int_0^\infty B_\nu(T)\,d\nu$, is proportional to the temperature T as $\chi_\mathrm{P} \propto T^\beta$. As the first step of studying in detail, and to extract primary features of radiation transfer, we simplify mass opacity as bellows. It is expected that $\beta = 2$ for ordinary dielectric material (van de Hulst, 1957; Draine & Lee, 1984; Miyake & Nakagawa, 1993). It is reported observationally that $1.75 \leq \beta \leq 2.5$ in the Orion Molecular Cloud-1 (Lis et al., 1998) in contrast to $-1 \leq \beta \leq 1$ in circumstellar disks around T Tauri stars in Taurus and Orion (Beckwith & Sargent, 1991). This change of the β value may be attributed to growth of the dust grain size (Miyake & Nakagawa, 1993). When we investigate a cloud in its collapsing phase, $\beta = 2$ seems to be appropriate. However, we would rather leave it as a model parameter in this study to examine the effect of the β value. Also, we take the absolute value of the mass opacity as a model parameter here, because the Planck mean mass opacity of mixed gas/dust fluid depends on the amount of dust (metalicity) as well as the size distribution of dust grains (Miyake & Nakagawa, 1993, 1995). Then, we have a model of the Planck mean mass opacity,

$$\chi_{\mathrm{P}} = \chi_{10} \left(\frac{T}{10\,\mathrm{K}} \right)^{\beta}, \tag{2.1}$$

where χ_{10} is the value at $T = 10$K. Note that T represents the common temperature of gas and dust grains. The thermodynamic character of our collapsing filaments would be characterized by the model parameters χ_{10} and β. Of course, we can adopt some opacity tables which are well developed recently. However, the main purpose of present study is not to pursue reality but to extract primary physics, especially the roles of radiation in gravitational radial collapse of filamentary molecular clouds. Therefore, above simple expression of mass opacity is more desirable than precise opacity data.

In addition, we adopt gray approximation for emission and absorption processes through dust particles and neglect scattering processes.

2.2.2 Filamentary Clouds

We adopt a simple model of a filamentary cloud to investigate the effects of radiative transfer clearly. An isolate, infinite long, axisymmetric filamentary cloud is assumed. Magnetic fields, turbulent motions, and rotation are neglected. The cylindrical coordinate (r, φ, z) is used to describe the configuration space. To simplify, we ignore all dependency on φ.

When the hydrostatic equilibrium is achieved in an isothermal filament, the density distribution is given by Ostriker (1964),

$$\rho_{\mathrm{eq}}(r, \rho_c, T) = \rho_c \left[1 + \left(\frac{r}{H(\rho_c, T)} \right)^2 \right]^{-2}, \tag{2.2}$$

where ρ_c is the density on the symmetric axis and H is the scale height defined by,

$$H(\rho_c, T) \equiv \left(\frac{2RT}{\pi G \rho_c \mu}\right)^{1/2}, \tag{2.3}$$

where R is the gas constant, G is the gravitational constant, and $m_{\rm H}$ is the mass of a hydrogen atom, respectively. The line mass of the equilibrium filament, $m_{\rm eq}$, is given by,

$$m_{\rm eq}(T) \equiv \int_0^\infty 2\pi r \rho_{\rm eq}(r)\, dr = \frac{2RT}{G\mu} \approx 17 \left(\frac{T}{10\,{\rm K}}\right) M_{\rm sun}\,{\rm pc}^{-1}. \tag{2.4}$$

The equilibrium line mass $m_{\rm eq}$ is independent of the central density ρ_c.

When the line mass of a filament is larger than the equilibrium line mass $m_{\rm eq}$, which corresponds to Bonner–Ebert mass of spherical gas (Fischera & Martin, 2012), the filament is gravitationally unstable and is expected to begin dynamical collapse. In order to let a filament collapse, we suppose that the initial density distribution of the filament is given by,

$$\rho_{\rm init}(r, \rho_c, T_{\rm init}) = \rho_c \left[1 + \left(\frac{r}{hH(\rho_c, T_{\rm init})}\right)^2\right]^{-2}, \tag{2.5}$$

where h is a non-dimensional model parameter. Since the line mass of this filament is given by $h^2 m_{\rm eq}$, the filament is gravitationally unstable when $h > 1$. We adopt $h = \sqrt{2}$ as a standard value of h, since numerical study of the fragmentation of isothermal sheet-like clouds showed that the line mass of a filament formed through the fragmentation is about twice as large as the equilibrium mass (Miyama et al., 1987a,b). Addition to above theoretical reason, most of star forming filaments observed by *Herschel* has line mass higher than $m_{\rm eq}$ (Arzoumanian et al., 2011). Therefore assuming filaments whose line mass is given by $h^2 m_{\rm eq}$ is presumable in terms of observations.

2.2.3 Heating and Cooling Processes

The balance between the heating and cooling processes determines the temperature of molecular clouds. The temperature of molecular clouds in the solar vicinity (e.g., Taurus, Orion, and ρ Ophiuchi) is about 8 – 60 K. Additionally, star-forming filaments that are observed by *Herschel* space observatory (Pilbratt et al., 2010) also show similar temperature (Arzoumanian et al., 2011), typically $\sim$ 10 K. The variation of the cloud temperature implies the variation of heating and cooling processes. These variations are dealt with as a parameter in this study.

The dust cooling rate per unit mass is given as,

$$\Lambda_{\rm dust} \equiv 4\sigma \chi_{\rm P} T^4 = 4.5 \times 10^{-2} \left(\frac{\chi_{10}}{0.02\,{\rm cm}^2\,{\rm g}^{-1}}\right) \left(\frac{T}{10\,{\rm K}}\right)^{4+\beta} {\rm erg\,g^{-1}\,s^{-1}}, \tag{2.6}$$

where σ is the Stefan-Boltzmann constant. We neglect other cooling processes (e.g., CO line cooling) for the sake of simplicity and they are less effective than the thermal emission from dusts.

That the line emission from gas is ignored.

Several possible heating sources are present in the dense clouds: interstellar UV radiation (including grain photoelectric heating), diffuse infrared radiation, cosmic rays, gas compressional heating, H_2 formation on dust grains, magnetic ion-neutral slip heating, and so forth.

Although there are several heating sources referred to above, we adopt two model heating sources in this study: the external radiation, the cosmic ray, and the compressional heating. We neglect the UV heating assuming that the UV radiation is shut out by envelope surrounding molecular cores. In typical situations, cosmic ray heating is too small to sustain the high temperature of molecular clouds e.g., 60K; however, to extract the characteristic of cosmic ray heating, we adopt such strong ray heating as a model. Additional heating (e.g., hydrogen molecular formation on dust surface, magnetic friction, and so forth) processes are neglected, both for simplification and due to their less efficiency comparing with dust heating and cooling (e.g., Goldsmith & Langer, 1978; Wolfire et al., 1995; Masunaga & Inutsuka, 1999; Koyama & Inutsuka, 2000).

2.2.4 Basic Equations

To describe such cooling and heating model, we assume the velocity of radiating fluid is non-relativistic, the gas is in local thermal equilibrium (LTE), and the equation of state is ideal. Using the total frequency-integrated form (so-called gray approximation), the moment equations of coupled RHD to order unit in v/c on a frame comoving with the radiating fluid are (Mihalas & Mihalas, 1984; Turner & Stone, 2001)

$$\frac{D\rho}{Dt} + \rho \boldsymbol{\nabla} \cdot \boldsymbol{v} = 0, \tag{2.7}$$

$$\rho \frac{D\boldsymbol{v}}{Dt} = -\boldsymbol{\nabla} p - \rho \boldsymbol{\nabla} \Phi + \frac{\rho \chi_{\mathrm{F}}}{c} \boldsymbol{F}, \tag{2.8}$$

$$\rho \frac{D}{Dt}\left(\frac{E}{\rho}\right) = -\boldsymbol{\nabla} \cdot \boldsymbol{F} - \boldsymbol{\nabla} \boldsymbol{v} : \mathbf{P} + 4\pi \rho \chi_{\mathrm{P}} B - c \rho \chi_{\mathrm{E}} E, \tag{2.9}$$

$$\rho \frac{D}{Dt}\left(\frac{e}{\rho}\right) = -p \boldsymbol{\nabla} \cdot \boldsymbol{v} - 4\pi \rho \chi_{\mathrm{P}} B + c \rho \chi_{\mathrm{E}} E + \rho \Gamma_{\mathrm{CR}}, \tag{2.10}$$

$$\frac{\rho}{c^2} \frac{D}{Dt}\left(\frac{\boldsymbol{F}}{\rho}\right) = -\boldsymbol{\nabla} \cdot \mathbf{P} - \frac{1}{c} \rho \chi_{\mathrm{F}} \boldsymbol{F}, \tag{2.11}$$

$$p = \frac{k_{\mathrm{B}}}{\mu m_{\mathrm{U}}}\rho T = (\gamma - 1)e, \tag{2.12}$$

and

$$\nabla^2 \Phi = 4\pi G\rho. \tag{2.13}$$

Here fluid variables ρ, $\boldsymbol{v}$, p, and e are the material mass density, fluid velocity, scalar isotropic gas pressure, gas energy per unit volume, respectively. Radiation variables E, $\boldsymbol{F}$, $\mathbf{P}$, B, and c, are the total frequency-integrated radiation energy per unit volume, flux, pressure tensor, Planck function, and speed of light, respectively. In the equation (2.12), k_B, μ, m_{U}, γ, and T are the Boltzmann constant, mean molecular weight, atomic mass unit, specific heat ratio, and temperature of fluid, respectively. In the equation of Poisson, G is the gravitational constant. Here Lagrange differential is described as $D/Dt \equiv (\partial/\partial t + \boldsymbol{v} \cdot \boldsymbol{\nabla})$. The energy mean, Planck mean, and flux mean opacities are defined by

$$\chi_{\mathrm{E}} \equiv \int_0^\infty \chi_\nu E_\nu \, d\nu \Big/ \int_0^\infty E_\nu \, d\nu, \tag{2.14}$$

$$\chi_{\mathrm{P}} \equiv \int_0^\infty \chi_\nu B_\nu \, d\nu \Big/ \int_0^\infty B_\nu \, d\nu, \tag{2.15}$$

and

$$\chi_{\mathrm{F}} \equiv \int_0^\infty \chi_\nu F_\nu \, d\nu \Big/ \int_0^\infty F_\nu \, d\nu, \tag{2.16}$$

where χ_ν, E_ν, B_ν, and F_ν are the frequency-dependent mass absorption opacity, the radiation energy density, the Planck function, and the absolute value of the radiation flux within a frequency interval $\nu - (\nu + d\nu)$, respectively. The cosmic ray heating rate per unit mass is represented by Γ_{CR}. We assume that the value of Γ_{CR} is a constant always and everywhere.

In this study, we assume that $\chi_{\mathrm{E}} = \chi_{\mathrm{P}} = \chi_{\mathrm{F}}$ for the sake of simplicity. The validity of this assumption is briefly discussed in appendix A.

The set of RHD equations given here is not completed, because an equation that describes the time evolution of the radiation pressure tensor $\mathbf{P}$ is absent. But that equation ($D\mathbf{P}/Dt = \cdots$) introduces another unknown terms (higher order moments of the intensity), hence the system of equations would not be completed (the closure problem; Mihalas & Mihalas, 1984). To close the RHD equations, any relations that corresponds the equation of state in hydrodynamics is required. A method to obtain the relation is explained later.

2.3 Analytical Prediction

The gravitationally collapsing filaments are isothermal in the early phase, but the isothermality breaks down at a certain time. Then the filaments enter the non-isothermal phase; the thermodynamical transition occurs during the gravitational collapse. And the thermodynamical transition of the filaments depends on the radiative transfer since it is the primary energy transport process in the clouds. Masunaga & Inutsuka (1999) analytically found the condition at which the isothermality breaks down focusing on the thermodynamical transition of the collapsing filaments. They assume that the main heating source is the diffuse infrared radiation and the compression heating. In this subsection, we review a part of their analytical approach to figure out essential physics clearly. Additionally, we extend it for filaments, in which the main heating source is cosmic ray.

Initial Isothermality

In order to investigate the departure from the isothermal state, it should be clarified first why the filaments are isothermal in the early phase. Before the gravitational collapse starts, the balance between the heating and cooling is achieved. And that is the case as well at the center of the filament, so we have $\Gamma_{\rm heat} = \Lambda_{\rm cool}$, where $\Gamma_{\rm heat}$ and $\Lambda_{\rm cool}$ are arbitrary heating and cooling rates at the center. Since the filament is optically thin in an early phase, $\Lambda_{\rm cool}$ can be substituted by the dust cooling $\Lambda_{\rm dust}$. On the other hand, the initial heating rate is given by $\Gamma_{\rm heat} = \Gamma_{\rm abs}$ (when the filament is heated by external radiation), where $\Gamma_{\rm abs} \equiv c\chi E$, or $\Gamma_{\rm heat} = \Gamma_{\rm CR}$ (when the filament is hearted by cosmic rays), where $\Gamma_{\rm CR}$ is the heating rate due to cosmic ray. The filament can hold its isothermality during the gravitational collapse as long as the energy balance $\Gamma_{\rm heat} = \Lambda_{\rm cool}$ is held. And when a heating source that disturbs the energy balance appears, the isothermality breaks down.

Break Down of Isothermality

The time at which the isothermality breaks down can be specified by the central density and the isothermal temperature, since the density distributions of collapsing filaments in the isothermal phase can be approximated by the equilibrium distribution defined by equation (2.2), which is characterized by the central density ρ_c and the temperature T. We call the central density at which the isothermality breaks down, "the critical density" or simply $\rho_{\rm crit}$. The critical density depends on the initial isothermal temperature and the type of the heating source. In the followings, we show an analytical expression of the critical density.

The optical depth of a filament is defined as

$$\tau \equiv \int_0^\infty \chi_\mathrm{P}\, \rho(r)\, dr \simeq \rho_\mathrm{c}\, \chi_\mathrm{P} H(\rho_\mathrm{c}, T). \tag{2.17}$$

The dust cooling rate depends on τ, because the radiation energy emitted from dust grains is trapped in the filament when the filament is opaque, or it can escape freely when the filament is transparent. To treat the problem generally, we introduce the effective cooling rate Λeff, which depends on the optical depth τ. When the filament is optically thin ($\tau < 1$), the effective cooling rate per unit mass should be identical to the dust cooling rate Λ_dust. On the contrary, when the filament is optically thick ($\tau > 1$), the effective cooling rate is reduced. Since the radiative diffusion approximation is valid in the optically thick media, the radiative energy flux is given as $\boldsymbol{F} = -\frac{c}{3\rho\chi_\mathrm{R}}\nabla E$, where $E = aT^4$, a is the radiation energy constant ($a = 4\sigma/c$), and χ_R is the Rosseland mean opacity which is assumed to be comparable to χ_P here because we assume $\chi_\nu \propto \nu^\beta$ (see appendix A). Then, we can approximate the effective cooling rate in the optically thick regime as,

$$\Lambda_\mathrm{eff}^\mathrm{thick} = \frac{1}{\rho}\boldsymbol{\nabla}\cdot\boldsymbol{F} = \frac{1}{\rho}\boldsymbol{\nabla}\cdot\left(-\frac{c}{3\rho\chi_P}\nabla E\right). \tag{2.18}$$

Assuming a convex energy distribution ($\nabla^2 E < 0$), the equation above can be evaluated as $\Lambda_\mathrm{eff}^\mathrm{thick} \simeq c\chi_\mathrm{P} aT^4/3(\rho\chi_\mathrm{P})^2 H^2$, where we adopt the scale height H as a characteristics scale. Substituting τ^2 for $3(\rho\chi_\mathrm{P}H)^2$, we obtain the approximate expression of the cooling rate in the optically thick regime $\Lambda_\mathrm{eff}^\mathrm{thick} \simeq \Lambda_\mathrm{dust}/\tau^2$. Combining expressions for the optically thin and the thick cases, the effective cooling rate for any optical depth case is given by,

$$\Lambda_\mathrm{eff} = \frac{\Lambda_{dust}}{\max(1, \tau^2)}. \tag{2.19}$$

Since Λ_eff depends on τ, we should know if the filament is optically thin or thick. We define the density ρ_τ at which τ becomes unity: $\frac{\pi}{4}\rho_\tau\chi_\mathrm{P}H(\rho_\tau, T) = 1$. Solving the equation, we have

$$\rho_\tau = 1.18 \times 10^{-12} \left(\frac{\chi_{10}}{0.02\,\mathrm{cm^2 g^{-1}}}\right)^{-2} \left(\frac{T}{10\,\mathrm{K}}\right)^{-(1+2\beta)} \mathrm{g\,cm^{-3}}. \tag{2.20}$$

For the filaments whose central densities are higher than ρ_τ, the expression for the optically thick case $\Lambda_\mathrm{eff}^\mathrm{thick}$ should be applied, and the expression for the optically thin case $\Lambda_\mathrm{eff}^\mathrm{thin}$ should be applied for the filaments with lower central density than ρ_τ.

Critical Density for Radiation Heated Filaments

When the filament is heated by the radiation with the temperature $T_{\rm B}$, the primary heating source in an early phase of the collapse is the radiation heating $\Gamma_{\rm abs,B} = c\,\chi_{\rm P}\,aT_{\rm B}^4$. Since this heating energy is transported by the radiation, the heating rate is reduced in an optically thick region. The reduced heating rate can be estimated as $\Gamma_{\rm abs,B}/\tau^2$. Thus, if there is no heating source except for the radiation heating from the boundary, the energy balance with the initial temperature $\Lambda_{\rm eff}(T_{\rm init}) = \Gamma_{\rm abs,B}(T_{\rm init})$ is held and the filament is expected to hold the isothermality. However, if the additional heating source, for example, the compressional heating, $\Gamma_{\rm dyn}$, which is defined as $-(p/\rho)\boldsymbol{\nabla}\cdot\boldsymbol{v}$, becomes comparable to $\Gamma_{\rm abs,B}$, the energy balance with the initial temperature cannot hold any more. Hence, we can expect that the isothermality breaks down when the additional heating rate $\Gamma_{\rm dyn}$ becomes the same order with $\Lambda_{\rm eff}$.

Masunaga & Inutsuka (1999) defined the critical density, at which the isothermality breaks down, by $\Lambda_{\rm eff} = \Gamma_{\rm dyn}$. Using expressions derived before, they present the critical density of mainly radiation heated filaments, which is called $\rho_{\rm crit}^{\rm Rad}$ in present paper, as follows:

$$\rho_{\rm crit}^{\rm Rad} = \begin{cases} \rho_s \left(\frac{T_{\rm init}}{T_s}\right)^{6+2\beta} & \text{for } T_{\rm init} \le T_s, \\ \rho_s \left(\frac{T_{\rm init}}{T_s}\right)^{(4-2\beta)/3} & \text{for } T_{\rm init} \ge T_s, \end{cases} \tag{2.21}$$

where ρ_s and T_s are,

$$\rho_s = 2.85 \times 10^{-13} \left(\frac{\chi_{10}}{0.02\,{\rm cm^2 g^{-1}}}\right)^{-\frac{10}{7+4\beta}} {\rm g\,cm^{-3}}, \tag{2.22}$$

and

$$T_s = 13.3 \left(\frac{\chi_{10}}{0.02\,{\rm cm^2 g^{-1}}}\right)^{-\frac{4}{7+4\beta}} {\rm K}, \tag{2.23}$$

respectively. Here their original formulae are rewritten for convenience of comparing analytical predictions to numerical results, nevertheless equations (2.21)–(2.23) are identical to them.

Dependence of $\rho_{\rm crit}^{\rm Rad}$ and ρ_τ on initial temperature is shown in figure 2.1 (left panel). Conceptual expected evolution tracks of filaments that collapse from different initial conditions ($T > T_s$ and $T < T_s$) are overlapped. Figure 2.1 shows that the line of the critical density $\rho_{\rm crit}$ intersects the line of ρ_τ at $T_{\rm init} = T_s$. Notice that filaments whose initial temperature $T_{\rm init}$ is higher than T_s become opaque before exceeding the critical density. Then the filaments hold isothermal even though they are opaque. Moreover, in the case of $\beta = 2$, the $\rho_{\rm crit}$ has a remarkable property that the critical density for $T_{\rm init} > T_s$ is independent of the initial temperature of the filament.

It is an interesting subject to examine effects of the absolute value of the opacity χ_{10} on the critical density. Figure 2.2 shows $\rho_{\rm crit}$ in the case of relatively more opaque, $\chi_{10} = 10^{-4}\,{\rm cm^2\,g^{-1}}$, and transparent, $\chi_{10} = 1\,{\rm cm^2\,g^{-1}}$. It is seen that T_s and ρ_s shift to the upper-right side of the panel in opaque case. Therefore, the filament with $T_{\rm init} = 40$ K becomes non-isothermal in its optically thin phase. On the contrary, in transparent case, the T_s and ρ_s shift to the left side of the panel. Hence, even the cloud with $T_{\rm init} = 8$ K can hold isothermality for a while in its optically thick phase.

Critical Density for Cosmic Ray Heated Filaments

The expression of $\rho_{\rm crit}^{\rm Rad}$ should be changed partially if main heating source is cosmic ray. When the filament is heated by cosmic rays, the heating rate $\Gamma_{\rm CR}$ is supposed to be constant per unit mass of fluid. The initial energy balance is achieved as $\Lambda_{\rm dust}(T_{\rm init}) = \Gamma_{\rm CR}(T_{\rm init})$. This equation is broken down if (1) the additional heating rate becomes the same order with $\Lambda_{\rm dust}(T_{\rm init})$ or (2) the effective cooling rate $\Lambda_{\rm eff}(T_{\rm init})$ declines due to the optical depth τ. The first condition leads to the same expression with that of the radiation heated filaments, $\rho_{\rm crit}^{\rm Rad}$ (for $T_{\rm init} < T_s$). The second condition is met when $T_{init} > T_s$ and the filament becomes optically thick. Hence, the critical density for $T_{\rm init} > T_s$ becomes identical to ρ_τ. Thus, we have the critical density for cosmic ray heated filaments,

$$\rho_{\rm crit}^{\rm CR} = \begin{cases} \rho_s \left(\frac{T_{\rm init}}{T_s}\right)^{6+2\beta} & \text{for } T_{\rm init} \le T_s, \\ \rho_s \left(\frac{T_{\rm init}}{T_s}\right)^{-(1+2\beta)} & \text{for } T_{\rm init} \ge T_s, \end{cases} \tag{2.24}$$

where ρ_s and T_s are given by equations (2.22) and (2.23). Dependence of $\rho_{\rm crit}^{\rm CR}$ and ρ_τ on initial temperature is also shown in figure 2.1 (right panel). It is seen that the temperature should be raised in the optically thick region. The high $\Gamma_{\rm abs}$ in the region is caused by the radiation emitted from dust grains. It reflects the fact that the emitted radiation cannot escape from the optically thick region freely.

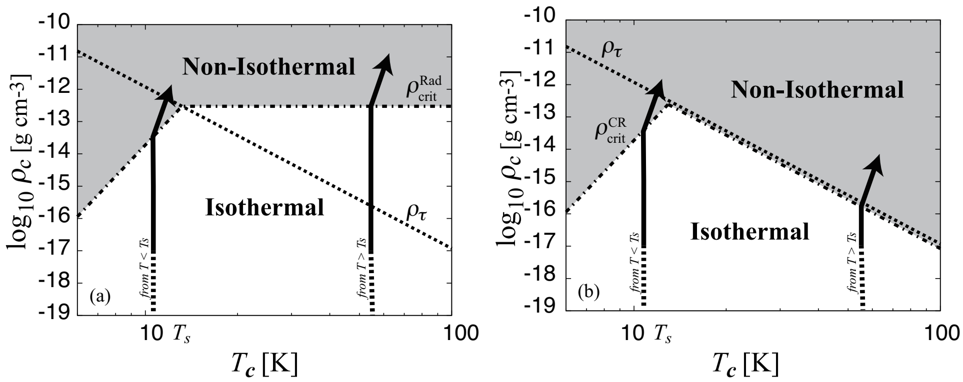

Figure 2.1: Critical density expected analytically. The horizontal axis means the central temperature and the vertical axis means the central density. The left panel represents radiation heated filaments ($\rho_{\rm crit}^{\rm Rad}$) and the right panel represents cosmic ray heated filaments ($\rho_{\rm crit}^{\rm CR}$). To help comprehending figures, conceptual evolution tracks are overlapped. Respective arrows mean the tracks of respective filaments, which have individual initial conditions. From the bottom to the top in figures, it is expected for the central density and the temperature of filaments to evolve roughly along thick solid allows. Here, assumed opacity is $\chi_{10} = 0.02\,{\rm cm}^2\,{\rm g}^{-1}$.

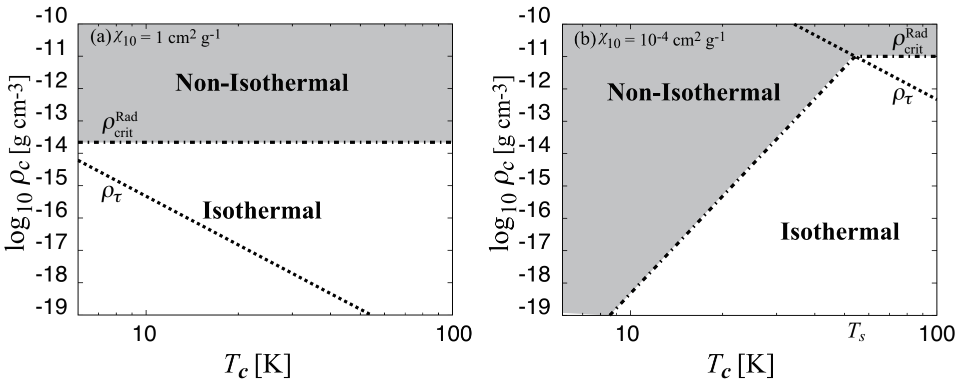

Figure 2.2: Critical density expected analytically. Radiation heated filaments that have the higher opacity (*left*: $\chi_{10} = 1\,\mathrm{cm^2\,g^{-1}}$) and the lower opacity (*right*: $\chi_{10} = 10^{-4}\,\mathrm{cm^2\,g^{-1}}$) are assumed. See also the legend of figure 2.1.

2.4 Method

In the present work, we perform radiation hydrodynamics simulations on the cylindrical coordinate to investigate the evolution of filamentary clouds. We adopt ZEUS-2D (Stone & Norman, 1992) as the self-gravitational hydrodynamics solver and VEF method (Stone et al., 1992) to obtain the closure relation.

2.4.1 Hydrodynamics: ZEUS

We adopt ZEUS (Stone & Norman, 1992; Hayes et al., 2006) to solve self-gravitational hydrodynamics equations. This code is based on operator-splitting, Euler staggered mesh, and finite difference method. We extracted the hydrodynamics and gravity solver from the original ZEUS code, which is the originally radiation magneto-hydrodynamics code.

The reason why we adopt the code is following. First, the scalability. Thanks to operator-splitting formalization, we can simply introduce specific physics using specialized numerical approaches. Second, the reliability. There are some radiative hydrodynamics algorithm in astrophysics e.g., Enzo (Bryan et al., 2014), GADGET (Springel, 2005; Petkova & Springel, 2009), and RAMSES (Teyssier, 2002; Commerçon et al., 2011). Comparing with these codes, ZEUS is not inferior as HD code (examined in Iliev et al., 2006, 2009, in the context of cosmology). Third, two-dimensional cylindrical coordinate (RZ) can be used. The code ZEUS is written with covariant formalism, therefore we can select arbitrary coordinate.

2.4.2 Closure Relation: VEF

In order to close the system of basic equations, a closure relation is required. In the one-dimensional simulations, we adopt Variable Eddington Factor (VEF) or Variable Tensor Eddington Factor (VTEF) methods (Stone et al., 1992; Hayes & Norman, 2003). This method is relatively more complicated and time-consuming than other method, e.g., M1 closure (e.g., González et al., 2007) and FLD (e.g., Turner & Stone, 2001). However, optically intermediate (not thin nor thick) problems can be solved without artificial approximation such as flux-limiter used in the FLD theory. The problems we solve in this chapter are one-dimensional; thus, we choose this method to obtain the closure relation.

In this method, the Eddington factor tensor is gained solving the radiative transfer equation

$$\mathbf{f} \equiv \frac{\mathbf{P}}{E} = \frac{\int_0^\infty I\boldsymbol{nn}\,d\Omega}{\int_0^\infty I\,d\Omega}, \tag{2.25}$$

and close moment equations using this (Stone et al., 1992; Gnedin & Abel, 2001; Hayes & Norman, 2003), where I is the frequency integrated intensity, $\boldsymbol{n}$ is the unit vector of the direction of a ray, and Ω is the solid angle. Then, we have a closure relation

$$\mathbf{P} = \mathbf{f}E. \tag{2.26}$$

Adding the equation (2.26) to basic equations, we can complete the set of RHD equations.

In order to evaluate the variable Eddington factor $\mathbf{f}$, the intensity must be provided. The intensity can be obtained by solving the radiative transfer equation.

The speed of light is so fast that the radiation field in our problem achieves steady distribution in a short period of time, which is much shorter than the time scale of hydrodynamic motions. Thus, we can ignore the time dependence of the intensity. Then, in a three-dimensional space, the intensity depends on six independent variables, i.e., three from the configuration space, two from the directions, and one from the frequency. In the case of axially symmetric infinite long cylinder, the intensity depends on four independent variables, which are the radial distance r, the directions $\boldsymbol{n}$, and the frequency ν.

The change of the frequency-dependent intensity I_ν along a ray is described by the radiative transfer equation,

$$\frac{dI_\nu}{ds} = -\rho\chi_\nu I_\nu + \rho\chi_\nu S_\nu, \tag{2.27}$$

where ds is an element of the length along the ray and S_ν is the frequency dependent source function. Since the dominant opacity source is the dust grain, we can assume that the local thermodynamic equilibrium is achieved. Moreover, we can ignore the scattering effects because the scattering coefficient is much smaller than the absorption coefficient in the low frequency region in which we are interested. Therefore, we have $S_\nu = B_\nu(T)$.

Integrating the frequency dependent radiative transfer equation (2.27) over the frequency, we have the frequency integrated radiative transfer equation,

$$\frac{dI}{ds} = -\rho\chi_I I + \rho\chi_{\mathrm{P}} B(T), \tag{2.28}$$

where χ_I is the intensity mean opacity defined by $\chi_I = \int_0^\infty \chi_\nu I_\nu\,d\nu \,/\, \int_0^\infty I_\nu\,d\nu$ and $B(T)$ is the frequency integrated Planck function. We assume that $\chi_{\mathrm{I}} = \chi_{\mathrm{P}}$. This assumption is valid enough, because the temperature difference in the calculation domain is small

(Preibisch et al. 1995). The equation (2.28) is solved in the computational domain along lines of a ray to evaluate the variable Eddington factor in the equation (2.25). To define rays on the cylindrical coordinate, we adopt so-called tangent plane method (Stone et al., 1992). To calculate the set of linear equations, which is due to the divergent terms, we adopt a direct method because the problem is one-dimensional; thus, there is no difference between a direct method and an iterative method.

2.4.3 Initial and Boundary Condition

As the initial condition, it is assumed that the matter (gas and dusts) and photons are in thermal equilibrium and spatially isothermal. Based on the analytical prediction of the critical density, and to avoid the artificial "isothermal bounce" (see appendix H), we start calculations from the initial central density $\rho_{\mathrm{c,init}} = 10^{-4}\rho_{\mathrm{crit}}^{\mathrm{Rad}}$. In order to see the effects of initial temperature, i.e., the input energy coming from outside the filament, T_{init} is changed in a range of 8 – 60 K and the intensity of the radiation heating and the cosmic ray heating are changed to meet the initial temperature as well. The filaments are assumed to be static at the initial time ($\boldsymbol{v} = 0$ at $t = 0$). We suppose that $h = \sqrt{2}$, and $\beta = 2$.

Imposed boundary conditions are as follows. At innermost grid ($r = 0$), $dq/dr = 0$, and $f_q = 0$, for both fluid and radiation, where q represents a scalar physical quantity (e.g., density ρ) and f_q represents a flux physical quantity which has the radial direction (e.g., radial velocity v_r). On the other hand, at outermost grid, conditions for fluid and radiation are defined separately: $dq/dr = 0$ and $df_q/dr = 0$ for fluid, while $q = const.$ and $(1/r)\,\partial\,(r f_q)\,/\partial r$ for the radiation.

In both the radiation heated model and the cosmic ray heated model, radiation energy density is fixed at the outer boundary, while the cosmic ray heating rate is constant, independently of time and place. In the radiation heated model, $E = aT_{\mathrm{init}}^4 = aT_B^4$ at the outer boundary and $\Gamma_{\mathrm{CR}} = 0$ everywhere. On the other hand, in the cosmic heated model, the initial and boundary value of the radiation energy density is set to zero, while $\Gamma_{\mathrm{CR}} = (4\chi\sigma T^4)_{T=T_{\mathrm{init}}}$ everywhere. We employed 200 Eulerian grids along the radial direction. To resolute initial density distribution, the size of calculation area L_{r} is 10 times the initial scale height. To resolve the eventual structure, which formed after isothermality is broken off, the non-uniform grid interval is adopted. The grid interval increases as $r_i = \epsilon r_{i-1}$ ($i = 1,\, 2,\, 3\cdots$), where ϵ is a constant and $r_0 = 10^{12}$ cm. The dependence of results on the number and interval of grids is discussed in appendix B.

2.5 Results

We perform RHD simulations of gravitationally collapsing filaments under several conditions. The unit of length is chosen to be the initial scale height, H_0, given by,

$$H_0 \equiv H(\rho_{\rm c,init}, T_{\rm init}) \simeq 3.9 \times 10^3 \left(\frac{\rho_{\rm c,crit}}{10^{-18}{\rm gcm}^{-3}}\right)^{-1/2} \left(\frac{T_{\rm init}}{10{\rm K}}\right)^{1/2} {\rm AU}, \tag{2.29}$$

the unit of the velocity, v_0, is the sound velocity of the initial temperature given by,

$$v_0 \equiv \left(\frac{\gamma k_{\rm B} T_{\rm init}}{\mu m_{\rm H}}\right)^{1/2} \simeq 1.9 \times 10^4 \left(\frac{T_{\rm init}}{10{\rm K}}\right)^{1/2} {\rm cm\,s^{-1}}, \tag{2.30}$$

the unit of time is,

$$t_0 \equiv \frac{H_0}{v_0} \simeq 1.0 \times 10^5 \left(\frac{\rho_{\rm c,init}}{10^{-18}{\rm gcm}^{-3}}\right)^{-1/2} {\rm yr}, \tag{2.31}$$

and the unit of heating/cooling rate is,

$$\Gamma_0 \equiv \frac{v_0^2}{t_0} \simeq 1.2 \times 10^{-4} \left(\frac{\rho_{\rm c,init}}{10^{-18}{\rm gcm}^{-3}}\right)^{1/2} \left(\frac{T_{\rm init}}{10\,{\rm K}}\right) {\rm erg\,g^{-1}\,s^{-1}}. \tag{2.32}$$

2.5.1 Radial Profiles of Radiation Heated Filaments

Here, the dynamical evolution of filaments heated by external radiation is shown. The cosmic ray heating is not included in simulations described in this subsection ($\Gamma_{\rm CR} = 0$). As two typical cases, the evolution of filaments, whose temperature are $T_{\rm init} = T_{\rm B} = 10\,{\rm K}$ and $T_{\rm init} = T_{\rm B} = 40\,{\rm K}$, are described in this subsection. As a fiducial case, we assume $\chi_{10} = 0.02\,{\rm cm^2\,g^{-1}}$ here.

The Case for $T_{\rm init} = 10$ K

The temporal evolution of central density ρ_c is displayed in figure 2.3. For convenience, alphabet letters are labeled at some given times. As the time goes on, the central density rises up ($t/t_0 < 1.2$). But after $t/t_0 \sim 1.2$ (point E), the temperature increase is weaken temporarily. And it can be considered that the deceleration is caused by the departure from the isothermal state. Hereinafter we call such deceleration "bounce."

The profiles of the collapsing filament whose initial temperature is 10 K, which correspond to alphabets A, B, C, G, and H ($\log_{10} \rho_c = -16, -14, -12, \text{and} -11$) are shown in figure 2.4, while D, E, and F (around bounce) are shown in figure 2.5. The noteworthy features are described in detail below.

The evolution of density distribution is shown in panels (a) of figures 2.4 and 2.5. In terms of the characteristics of density profile, a collapsing filament can be divided into three parts: a *core filament*, an *inner envelope*, and an *outer envelope*. Here, the core filament is defined as a region within about $r < H(\rho_c, T_c)$ where the density is almost constant. As the central density ρ_c rises, the radius of the core filament, i.e., the scale height H decreases the following equation (2.3) as long as the temperature distribution is uniform. In the inner envelope, the density is in proportion to the radius as $\rho \propto r^{-4}$. The density distribution in the core filament and the inner envelope regions can be well approximated by $\rho_{\rm eq}(r, \rho_c, T_c)$ everywhere, if the temperature is constant. In fact, the absolute ratio of the gravity to the pressure gradient force is unity in those regions (panels (d)), though it is 2 (i.e., $h^2 = 2$) everywhere at the initial state. On the contrary, the outer envelope that is divided from inner envelope by shock wave front does not change significantly. The dynamical timescale of outer envelope is shorter than the central region; thus, it seems to be affected by only initial and the boundary conditions. In the innermost region of outer envelope, $r_{\rm shock} < r < H(\rho_{\rm init}, T_{\rm init})$, where $r_{\rm shock}$ is the position of the shock wave front, the density is in proportion to the radius as $\rho \propto r^{-1}$ because the infall can be approximated by the free fall into an extremely thin filament.

The evolution of velocity distributions is displayed in panels (b). Notice that the negative velocity means the inward flow. In the core region, velocity is constantly zero. In the inner envelope region, the speed of infall reaches the super sonic one and the absolute value monotonically increase with the increasing radius. After the appearance of bounce, the shock wave front appears at the end of inner envelope region. In the outer envelope region, the absolute value of the velocity monotonically decreases with the increasing radius.

The temperature distributions at several times are plotted in panels (c). The filament holds the isothermal temperature distribution $T = T_{\rm init}$ in an early phase ($t/t_0 \lesssim 1.2$). In a later phase ($t/t_0 \gtrsim 1.2$), the temperature begins to rise up mainly in the core region. After that, a steep increase in temperature appears around the shock wave front. Note that although the maximum temperature around the shock wave front exceeds the temperature in the core filament, the front locates outside of scale height H; thus, density is significantly lower than center, therefore the region has lower energy than the core filament. That is because, the shock wave does not affect the thermal and dynamic evolution of the core filament.

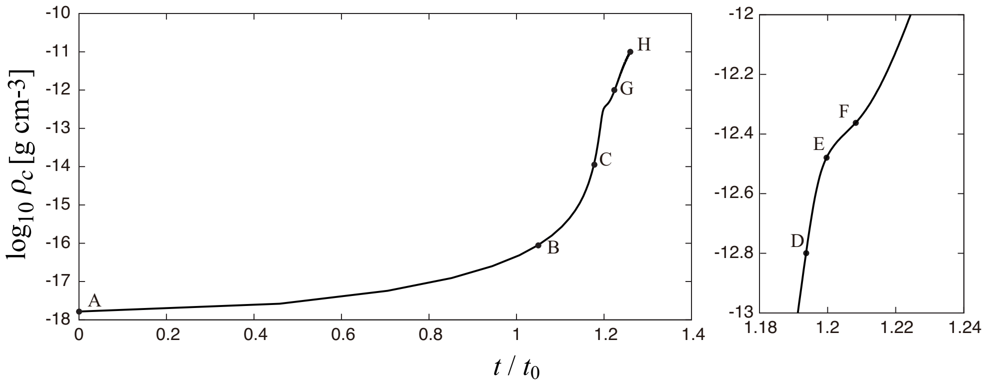

Figure 2.3: Evolution of the central density. The radiation heated model from $T_{\rm init} = 10\,{\rm K}$ is assumed. The horizontal axis means the time and the vertical axis means logarithm of the central density. The right panel is a magnified view of one part of the left panel. Eight points are labeled with alphabet letters in order of time (A: $t = 0$ yr, B: $t = 8.182 \times 10^4$ yr, C: $t = 9.183 \times 10^4$ yr, D: $t = 9.303 \times 10^4$ yr, E: $t = 9.351 \times 10^4$ yr, F: $t = 9.417 \times 10^4$ yr, G: $t = 9.536 \times 10^4$ yr, H: $t = 9.821 \times 10^4$ yr).

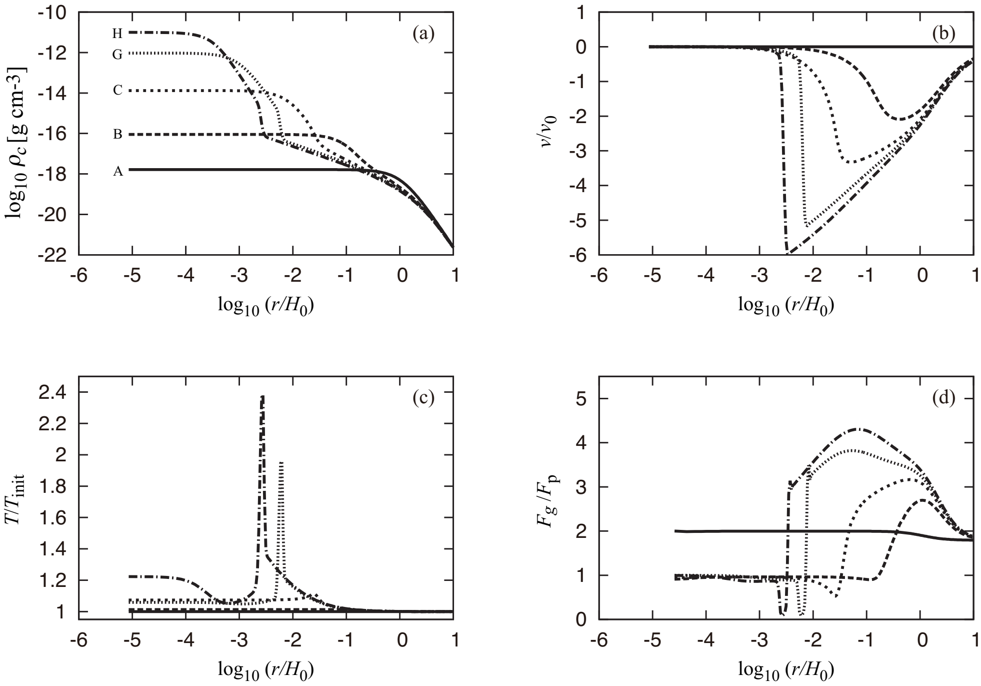

Figure 2.4: Evolutionary sequences of the radial profile of physical quantities. The distributions of (a) the density, (b) the velocity, (c) the temperature, and (d) the ratio of the gravity force $F_{\rm p} \equiv |-\nabla p/\rho|$ to the pressure gradient force $F_{\rm g} \equiv |\boldsymbol{g}|$ are shown. Alphabet letters, A, B, C, G, and H correspond to them in figure 2.3. The initial temperature of the cloud is 10 K.

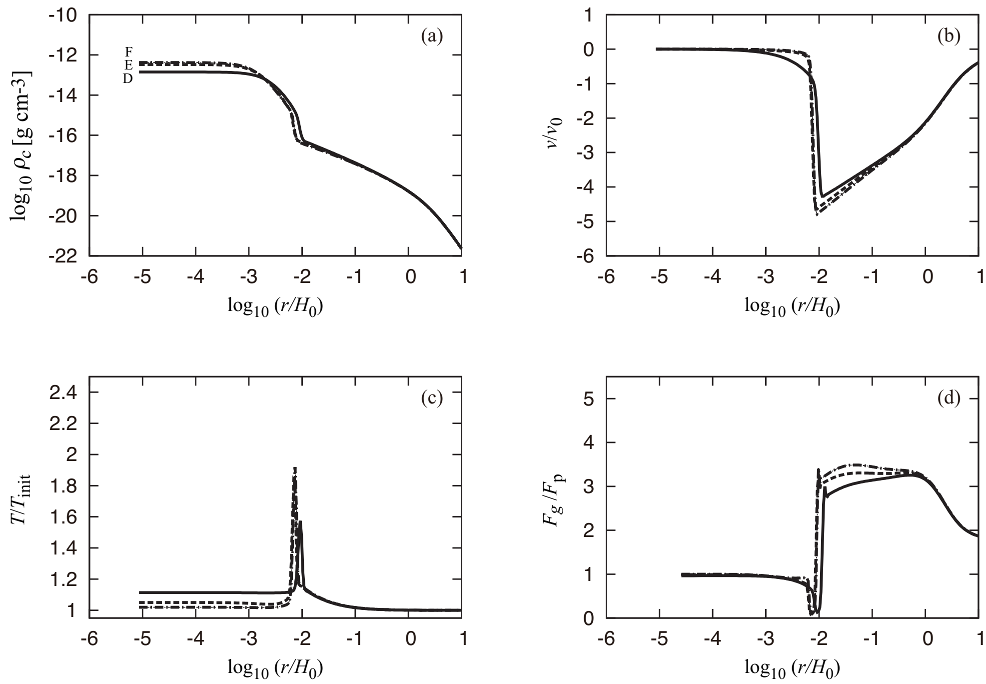

Figure 2.5: Evolutionary sequences of the radial profile of the physical quantities. The physical quantities of points that correspond to D, E, and F in figure 2.3 are shown. See also the legend of figure 2.4.

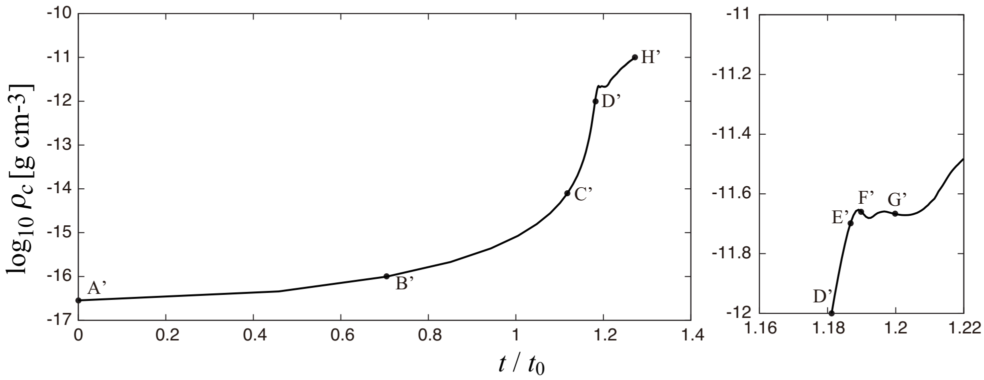

Figure 2.6: Evolution of the central density. The radiation heated model from $T_{\rm init}$ = 40 K is assumed. See also the legend of figure 2.3. Here nine points are labeled using alphabet letters with a prime mark (A': $t = 0$ yr, B': $t = 1.320 \times 10^4$ yr, C': $t = 2.094 \times 10^4$ yr, D': $t = 2.214 \times 10^4$ yr, E': $t = 2.223 \times 10^4$ yr, F': $t = 2.229 \times 10^4$ yr, G': $t = 2.248 \times 10^4$ yr, H': $t = 2.384 \times 10^4$ yr).

The Case for $T_{\rm init} = 40$ K

The temporal evolution of the central density ρ_c is displayed in figure 2.6. In a similar manner to figure 2.3, alphabet letters with a prime mark are labeled at some given times. The profiles in the collapsing filament whose initial temperature is 40 K, which correspond to alphabets A, B, C, D, and H ($\log_{10} \rho_c = -16, -14, -12,$ and-11) are shown in figure 2.7, while E, F, and G (around bounce) are shown in figure 2.8. Although the rough features are similar to, a clearer bounce appears than the case of $T_{\rm init} = 10$ K.

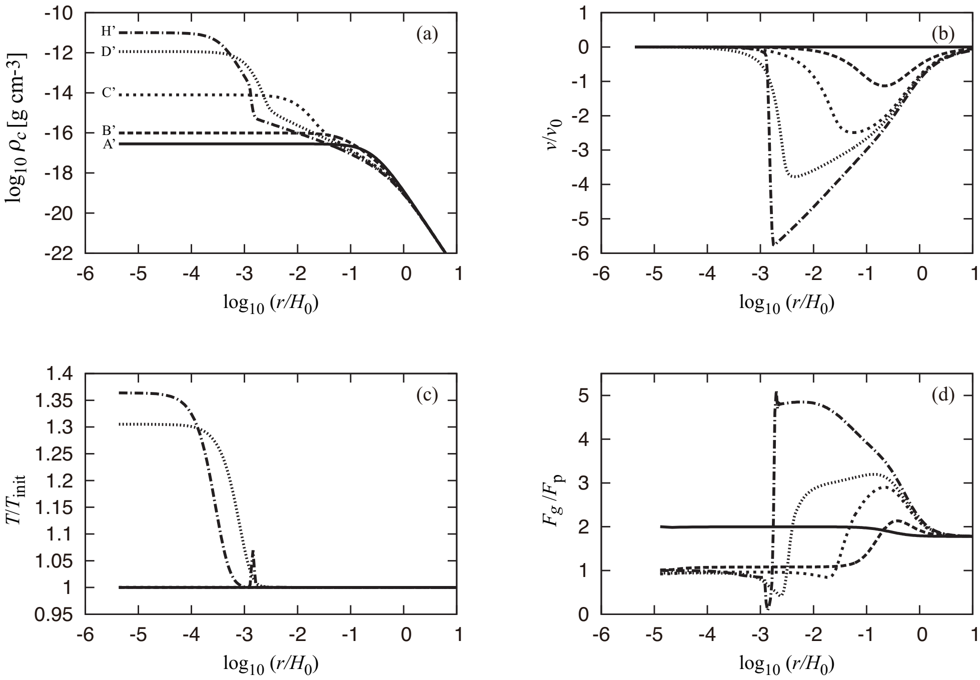

Figure 2.7: Evolutionary sequences of the radial profile of some physical quantities. Alphabet letters with a prime mark, A', B', C', D', and H' correspond to them in figure 2.6. The initial temperature of the cloud is $T_{\rm init} = 40$ K. See also the legend of figure 2.4.

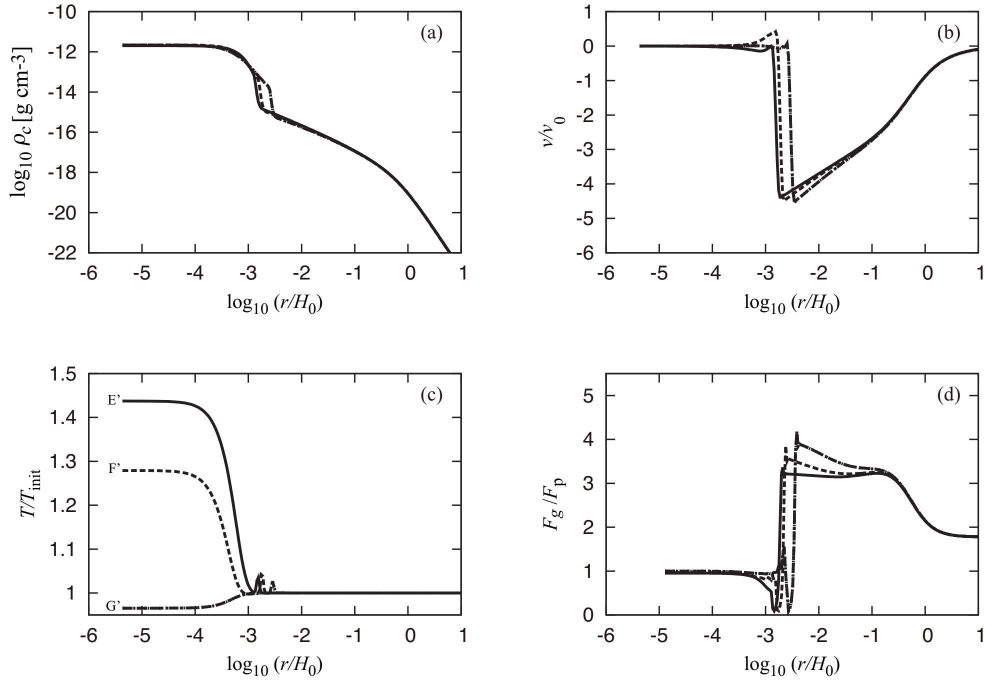

Figure 2.8: Evolutionary sequences of radial profile of some physical quantities. Physical quantities of points that correspond to E', F', and G' in figure 2.6 are shown. See also legend of figure 2.4.

2.5.2 The Central Temperature–Density Relation

The collapse of the filament can be characterized by the central density, $\rho_{\rm c}$, and the central temperature, $T_{\rm c}$. Using them, evolution tracks of radiation heated filaments whose opacity is $\chi_{10} = 0.02\,{\rm cm^2 g^{-1}}$ are shown in figure 2.9. Each track represents the evolution of each filament with different initial temperature $T_{\rm init}$. Tracks rise up vertically during the isothermal collapse and turn to the right when the isothermality on the axis breaks down. If the initial temperature is higher than about 13 K, the break down of the isothermality occurs at about 10^{-13} g cm^{-3} and that critical density is independent of the initial temperature. On the contrary, if $T_{\rm init} \lesssim 13$ K, the density at which the bounce occurs decreases as the initial temperature decreases. This behaviour can be understood by considering the dependence of the heating and cooling processes on the density and the temperature, which is discussed in §2.3. Dotted and dash-dotted lines displayed in the figure 2.9, which are defined by the density ρ_τ at which $\tau = 1$ and the critical density $\rho_{\rm crit}^{\rm Rad}$, respectively, are introduced (the equations (2.20) and (2.21)). The density at which tracks depart from isothermal phase are consistent with $\rho_{\rm crit}^{\rm Rad}$.

The similar evolution tracks of clouds whose opacity are low ($\chi_{10} = 10^{-4}\,{\rm cm^2 g^{-1}}$) and high ($\chi_{10} = 1\,{\rm cm^2 g^{-1}}$) are shown in figure 2.10. These are also consistent with analytical predictions, shown in figure 2.2.

The $T_{\rm c} - \rho_{\rm c}$ relation for the cosmic ray heated filamentary clouds ($T_{\rm B} = 0$ K and $\Gamma_{\rm CR} \neq 0$) is also shown in figure 2.11. It is seen that the central temperature of clouds whose initial temperature is higher than 13 K departs from isothermal collapse at the analytically predicted density, which is shown in figure 2.1.

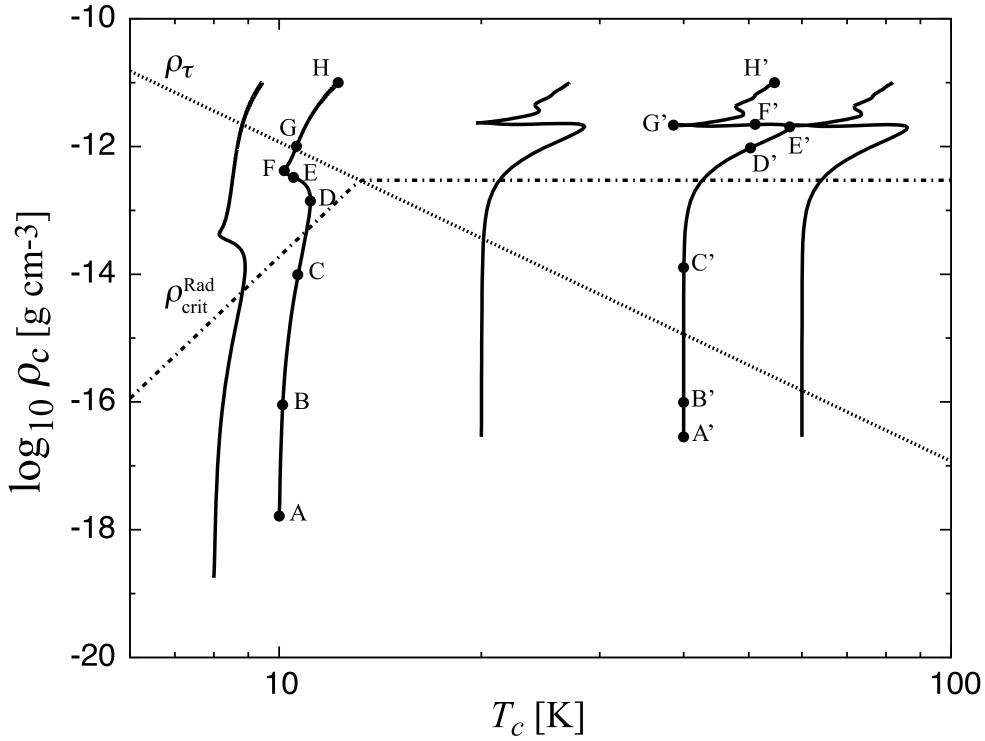

Figure 2.9: Evolution tracks of the central density and the central temperature of filamentary clouds heated by the external radiation. The dash-dotted line and the dotted line represent the critical density ($\rho_{\rm crit}^{\rm Rad}$) and the density at which the optical depth becomes unity (ρ_τ), respectively. Alphabet letters corresponds to them in figures 2.3 and 2.6.

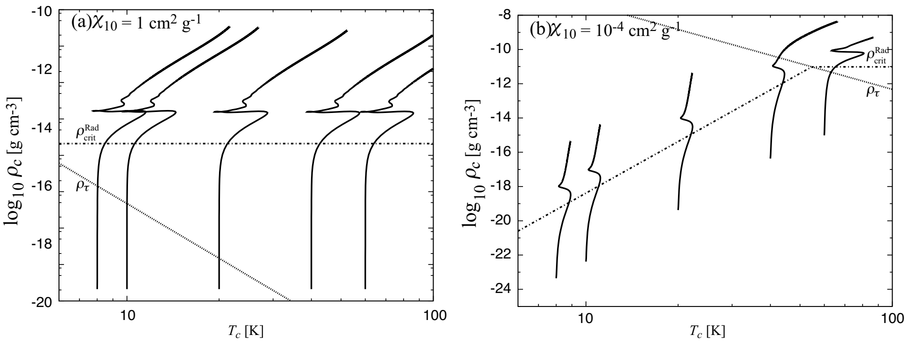

Figure 2.10: Evolution tracks of the central density and the central temperature of filamentary clouds heated by the external radiation. Here, *right*: $\chi_{10} = 1\,\mathrm{cm}^2\,\mathrm{g}^{-1}$ and *left*: $\chi_{10} = 10^{-4}\,\mathrm{cm}^2\,\mathrm{g}^{-1}$. See also legend in figure 2.9.

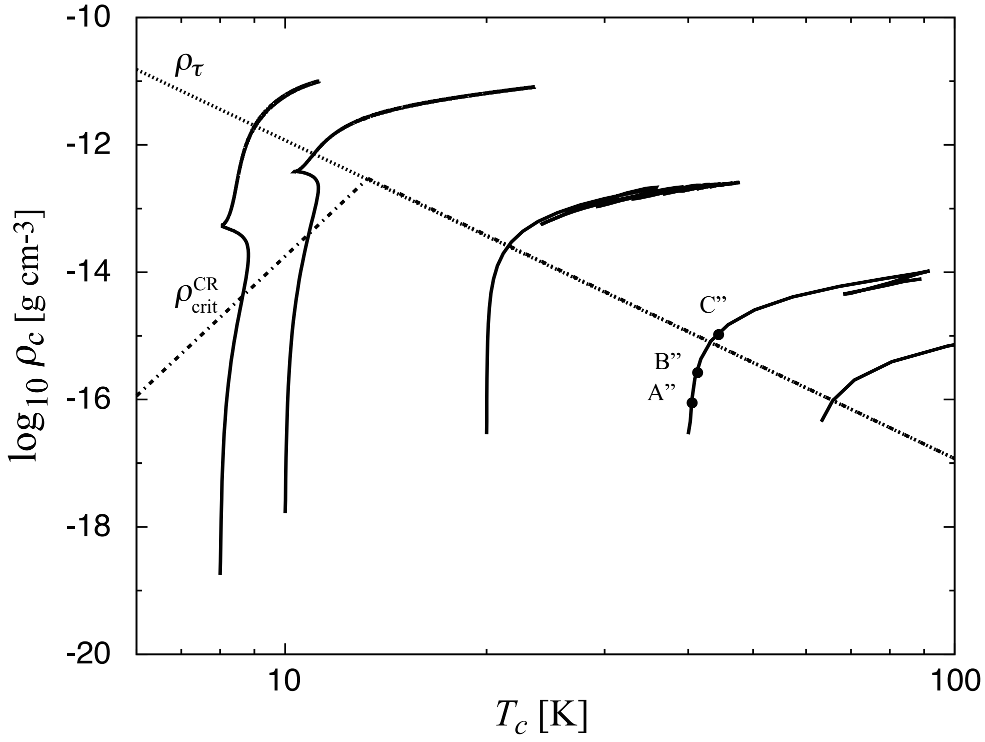

Figure 2.11: Evolution tracks of the central density and the central temperature of filamentary clouds heated by the cosmic ray. The dash-dotted line and the dotted line represent the critical density ($\rho_{\rm crit}^{\rm CR}$) and the density at which the optical depth becomes unity (ρ_τ), respectively. Some points are labeled with alphabet letters with the double prime mark to reference later e.g., in figure 2.16.

2.5.3 The Implication of Critical Density

The Heating and Cooling rates

The $T_c - \rho_c$ relation represented in figures 2.9, 2.10, and 2.11 indeed roughly reproduces some characteristics predicted in §2.3 analytically. However, they show some complex features including bounces; thus, it is not clear how, when, and where, heating/cooling processes take place.

To uncover the details, it is useful to see the profile evolution of heating/cooling rate simply. In particular, the most important factors are compressional heating rate $\Gamma_{\rm dyn}$ and effective cooling rate $\Lambda_{\rm eff}$ described in §2.3. We show their profile evolution of radiation heated filaments as follows. Note that, in this section we regard the optical depth as $\tau = \int_r^\infty \rho \chi_{\rm P} dr$, which is needed to define $\Lambda_{\rm eff}$.

In figure 2.12, the profile evolution of $\Gamma_{\rm dyn}$ and $\Lambda_{\rm eff}$ is shown. Their initial temperature is 10 K. Alphabets are identical to them defined in figure 2.3. Focusing on the central region ($r < H$), noteworthy features are following. While $\Lambda_{\rm eff} \gg \Gamma_{\rm dyn}$ is maintained during the period (A - C), the compressional heating rate is approaching the value of the effective cooling rate and eventually they establish $\Lambda_{\rm eff} \sim \Gamma_{\rm dyn}$ in density range (C - D), which includes $\rho_{\rm crit}$. In the phase of (D - E), in which density increase and temperature decrease, $\Lambda_{\rm eff} \gg \Gamma_{\rm dyn}$ is established again. In the phase after filaments become optically thick (F - G), on the one hand heating rate does not change significantly, on the other hand the cooling rate decreases efficiently; therefore, filaments evolve maintaining the relation $\Lambda_{\rm eff} \sim \Gamma_{\rm dyn}$.

In figure 2.13, same figures except for initial temperature are shown. The initial temperature is 40 K. Alphabets are identical to them defined in figure 2.6. Focusing on the central region ($r < H$), noteworthy features are following. While $\Lambda_{\rm eff} \gg \Gamma_{\rm dyn}$ is maintained during the period (A' - C'), they are $\Lambda_{\rm eff} \sim \Gamma_{\rm dyn}$ in density range (C' - D'), which includes $\rho_{\rm crit}$. In contrast to the results of $T_{\rm init} = 10$K, $\Lambda_{\rm eff}$ is decreasing as well as $\Gamma_{\rm dyn}$ is increasing in this phase. In the phase of (D' - G'), while $\Lambda_{\rm eff}$ keeps almost same profile, $\Gamma_{\rm dyn}$ is decreasing drastically; thus, $\Lambda_{\rm eff} \gg \Gamma_{\rm dyn}$ is established. Interestingly, the term $-p\nabla \cdot \boldsymbol{v}$ acts not only as compressional heating but also as expansion cooling, thus the $\Gamma_{\rm dyn}$ can be negative. After that, filaments collapse maintaining $\Lambda_{\rm eff} \lesssim \Gamma_{\rm dyn}$, as seen in phase (H').

Based on above two results, the numerical results are interpreted that indeed the behaviors of heating/cooling, which are analytically predicted in §2.3, are realized.

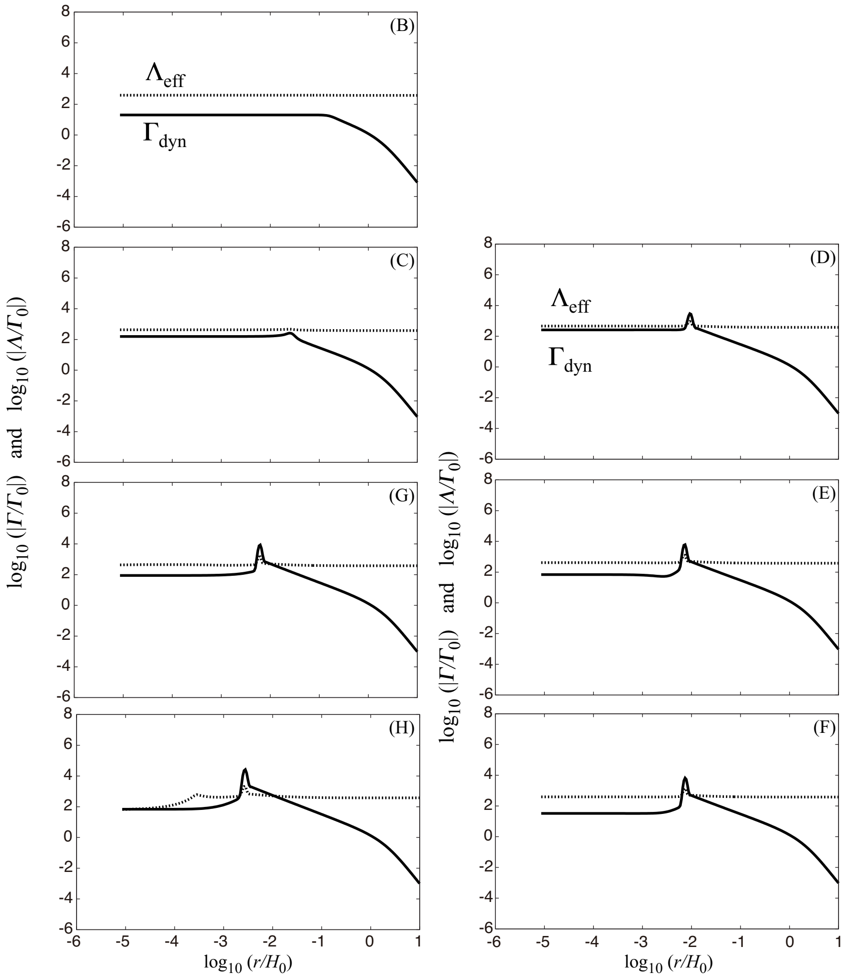

Figure 2.12: Evolution of the radial profile of heating and cooling rates. The initial temperature of the cloud is $T_{\rm init} = 10$ K. Alphabet letters correspond to them in figure 2.3.

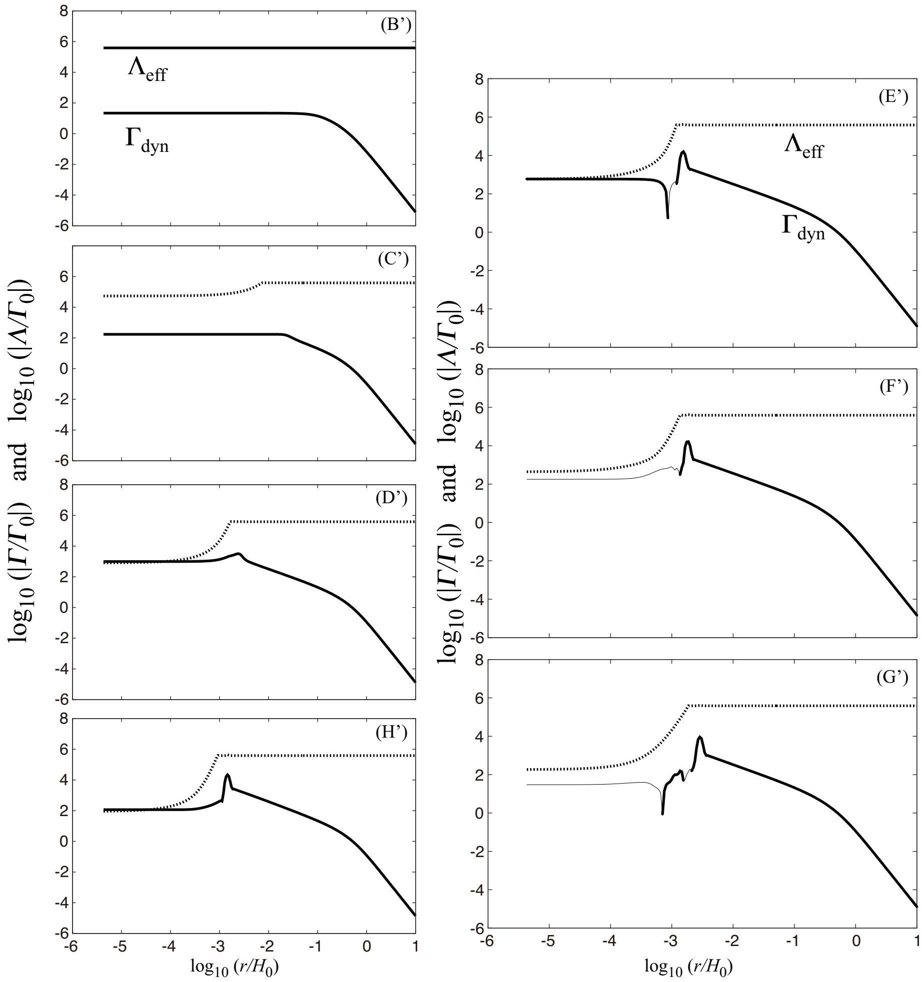

Figure 2.13: Evolution of the radial profile of heating and cooling rates. The initial temperature of the cloud is $T_{\rm init} = 40$ K. Alphabet letters correspond to them in figure 2.6. Note that the case of $\Gamma_{\rm den} < 0$ is represented with thin solid curves, while $\Gamma_{\rm den} > 0$ is represented with thick solid curves.

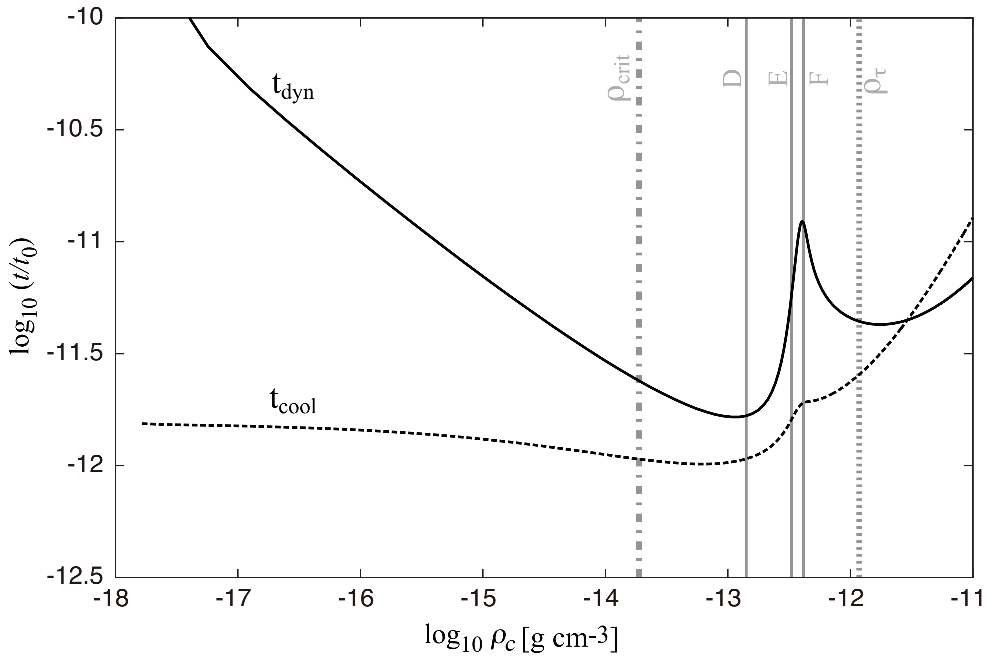

Figure 2.14: Evolution of Timescales. The initial temperature of the cloud is $T_{\rm init} = 10$ K. Gray perpendicular lines denote characteristic densities. Alphabet letters correspond to them in figure 2.3.

The Timescales

On the other hand, to verify the reliability of the analytical prediction $\rho_{\rm crit}$, which is the indicator of breakdown of isothermality, it is useful to compare the timescales at the center of filaments. In figures 2.14 and 2.15, the dynamical (= compressional heating) timescale defined as $t_{\rm dyn} \equiv e/(de/dt)$ and the cooling timescale $t_{\rm cool} \equiv e/\Lambda_{\rm eff}|_{r=0}$ are shown. The initial temperature is 10 K and 40 K in respective figures.

As mentioned in §2.3, the analysis predicts following features. Initially, $t_{\rm cool}$ should exceed $t_{\rm dyn}$ drastically. As time advances, the difference should be narrowed with density increasing. When $\rho_c \sim \rho_{\rm crit}$ is achieved, the timescales should be comparable.

Numerical results shown in figures 2.14 and 2.15 reproduce the prediction qualitatively. Based on this fact, it is implicated that the value of $\rho_{\rm crit}$ can be used as a good indicator of the breakdown of isothermality.

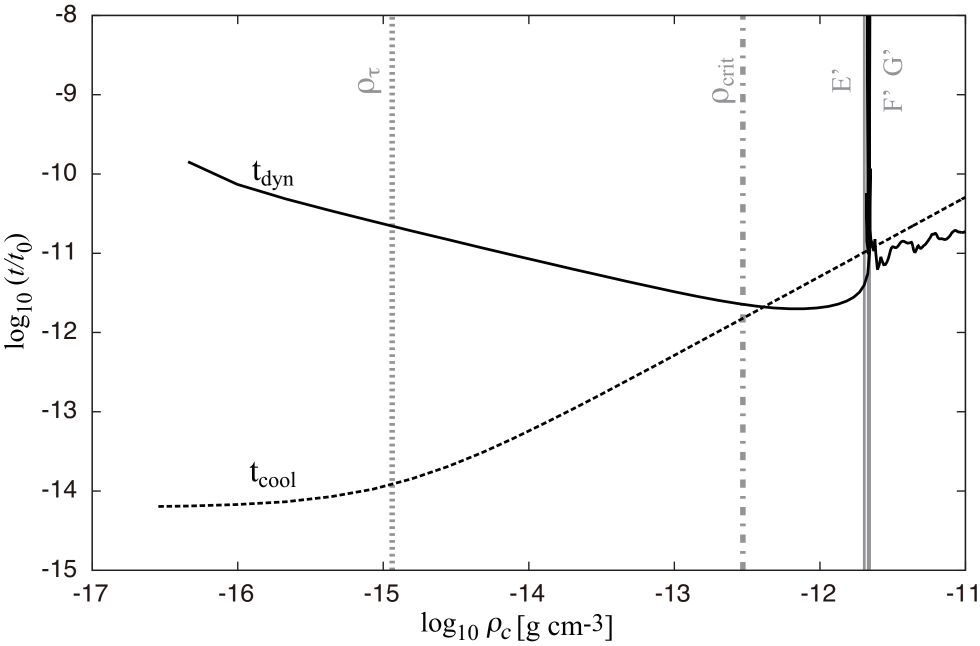

Figure 2.15: Evolution of Timescales. The initial temperature of the cloud is $T_{\mathrm{init}} = 40$ K. Gray perpendicular lines denote characteristic densities. Alphabet letters correspond to them in figure 2.6.

However, following three points should be noted carefully. First, there are non-negligible differences of the behavior between $T_{\rm init} = 10\,{\rm K}$ and $T_{\rm init} = 40\,{\rm K}$. Second, the appearance of "breakdown of isothermality" in the case of $T_{\rm init} = 10\,{\rm K}$ is much more moderate than in the case of $T_{\rm init} = 40\,{\rm K}$. Third, $\rho_{\rm crit}$ is just the indicator of the density, at which not the fragmentation occurs but the isothermality breaks down.

Again, first, there are non-negligible differences of the timescale behavior between the case of $T_{\rm init} = 10\,{\rm K}$ and $T_{\rm init} = 40\,{\rm K}$, which is itemized as follows:

1. The difference between $t_{\rm cool}$ and $t_{\rm dyn}$ in the case of $T_{\rm init} = 10\,{\rm K}$ is much less than the one in the case of $T_{\rm init} = 40\,{\rm K}$.

2. In the case of $T_{\rm init} = 10\,{\rm K}$, the magnitude relation $t_{\rm dyn} > t_{\rm cool}$ is maintained till ρ_c sufficiently exceeds ρ_τ. On the other hand, in the case of $T_{\rm init} = 40\,{\rm K}$, the relation is reversed shortly after ρ_c exceeds $\rho_{\rm crit}$.

3. During the "bounce", which is the deceleration caused by the increase in temperature, the amount of the rise in $t_{\rm dyn}$ is less than one digit in the case of $T_{\rm init} = 10\,{\rm K}$. However, in the case of $T_{\rm init} = 40\,{\rm K}$, $t_{\rm dyn}$ reaches infinity. In the other words, the central region of the filament keeps contracting even though non-isothermality may decrease the velocity when $T_{\rm init} = 10\,{\rm K}$, meanwhile the region experiences the expansion when $T_{\rm init} = 40\,{\rm K}$.

4. The deceleration is more moderate and continuous in the case of $T_{\rm init} = 10\,{\rm K}$ than the one in the case of $T_{\rm init} = 40\,{\rm K}$ (see also figures 2.3 and 2.6). Therefore, during bounce, the density increases about a half digit in the case of $T_{\rm init} = 10\,{\rm K}$ (D - F), while stay about the same value in the case of $T_{\rm init} = 40\,{\rm K}$ (E' - G').

The filament whose initial temperature is 8 K resembles 10 K, while ones whose initial temperature are 20 K and 60 K resembles 40 K. Therefore, it is suggested that whether pattern a filament shows is determined by whether $T_{\rm init} < T_s$ or not.

Second, the appearance of "breakdown of isothermality" in the case of $T_{\rm init} = 10\,{\rm K}$ is much more moderate than in the case of $T_{\rm init} = 40\,{\rm K}$. It is difficult to define the moment at which the isothermality breaks down clearly in the case of lower initial temperature, because $t_{\rm cool} \sim t_{\rm dyn}$ is usually kept. For example, if we define the word *comparable* as $t_{\rm cool}/t_{\rm dyn} < 10$, these timescales are *comparable* when $0.01\rho_{\rm crit} \lesssim \rho_c \lesssim 100\rho_{\rm crit}$ in the case of $T_{\rm init} = 10\,{\rm K}$. Therefore, it should be understood to interpret the value of $\rho_{\rm crit}$ as isothermality breakdown that the value could involve such uncertainty, particularly in the case of $T_{\rm init} < T_s$.

Third, even if the isothermality breaks down at $\rho_{\rm crit}$ instantaneously, $\rho_{\rm crit}$ is just the indicator of the density at which isothermality breaks down. As mentioned in §2.3, $\rho_{\rm crit}$ can be different from ρ_τ. Additionally, it is not always true that the dynamically characteristic density is nearly equal to $\rho_{\rm crit}$. Independently of the initial temperature, the densities at which the dynamical timescale is at minimum (around D or E') and maximum value (around F or G') is about one digit higher than $\rho_{\rm crit}$. It is difficult to judge when the fragmentation appears from this one-dimensional calculations.

2.5.4 The Evolutionary Phase

The relation between the temperature and the density at the center of filaments, which is shown in figures 2.9, 2.11, and 2.10, is useful to compare our numerical results with previous works. However, the evolutionary tracks show some complex features, and it is difficult to understand only on these figures. In this subsection, we define some evolutionary phases shown in figures 2.9, 2.11, and 2.10, and describe the characteristics of them.

Radiation Heated Filaments

In the case of radiation heated filaments, we divide the evolution into four phases: 1) quasi-isothermal, 2) first increase of the temperature, 3) decrease of the temperature, and 4) re-contraction. Detailed descriptions are following.

1) Quasi-isothermal phase: We define this phase as the period from initial condition to the break down of the relation $\Gamma_{\rm dyn} \ll \Lambda_{\rm eff}$. This phase corresponds to the region from A to $\rho_{\rm crit}$ ($T_{\rm init} = 10\,{\rm K}$) and from A' to $\rho_{\rm crit}$ ($T_{\rm init} = 40\,{\rm K}$) in figure 2.9. In this phase, the isothermality is roughly established. The gravitational force and the pressure gradient force is balanced in the core filament, while the inner and outer envelope infall freely. The sharp increase of temperature, which is expected when $\Gamma_{\rm dyn}$ exceeds $\Lambda_{\rm eff}$, has not started yet; therefore, filaments are not decelerated and the shock wave does not appear. Filaments whose initial temperature are sufficiently low ($T_{\rm init} = 8\,{\rm K}$ and $10\,{\rm K}$) show slight increase of temperature in this phase; however, $\Gamma_{\rm dyn}$ does not exceed $\Lambda_{\rm eff}$. The cause of this behavior is the fact that compressional heating is indeed smaller than other heating/cooling, however, not equal to zero. The increase of temperature can be evaluated assuming the following condition:

$$\rho \frac{d}{dt}\left(\frac{e}{\rho}\right) = -p\nabla\cdot\boldsymbol{v} - 4\pi\rho\chi B + c\rho\chi E + \rho\Gamma_{\rm CR} = 0. \tag{2.33}$$

Rewriting as

$$4\pi\chi B_{\mathrm{B}} \equiv c\chi E + \Gamma_{\mathrm{CR}} \tag{2.34}$$

and approximate compression heating roughly as

$$-p\nabla\cdot\boldsymbol{v} \sim \frac{p}{t_{\mathrm{ff}}}, \tag{2.35}$$

where

$$t_{\mathrm{ff}} \equiv \frac{1}{2\sqrt{G\rho_c}}, \tag{2.36}$$

we obtain

$$\rho_c = \left(\frac{2\chi\sigma}{\sqrt{G}c_s^2}\right)^2 \left(T^4 - T_{\mathrm{B}}^4\right)^2, \tag{2.37}$$

where c_s is isothermal sound speed. This estimation fits the temperature increase in this phase well.

The collapse of filaments whose initial temperature is low ($T_{\mathrm{init}} < T_s$) are decelerated slightly because of this increase of the temperature (polytropic index $\gamma_p > 1$). Mainly due to this effect, the behavior of filaments whose initial temperature is low ($T_{init} < T_s$) is different from ones whose initial temperature is high ($T_{init} > T_s$) around ρ_{crit} in figure 2.9.

2) First increase of the temperature phase: We define this phase as the period, in which $\Gamma_{\mathrm{dyn}} \sim \Lambda_{\mathrm{eff}}$; therefore, the temperature increases significantly, namely $\rho_c \sim \rho_{\mathrm{crit}}$. This phase corresponds to the region from C to D and from C' to D' in figure 2.9. Polytropic index $\gamma_p > 1$ therefore F_g/F_p decrease rapidly.

3) Decrease of the temperature phase: We define this phase as the period after the relation $\Gamma_{\mathrm{dyn}} \ll \Lambda_{\mathrm{eff}}$ is reestablished. This phase corresponds to the region from D to F and from E' to G' in figure 2.9. As mentioned, in filamentary molecular clouds, if polytropic index exceeds unit slightly, pressure decrease acceleration; therefore, Γ_{dyn} decreases as the temperature increase. Thus, the temperature tends to be the boundary value again, which results in the decrease of the temperature. Additionally, if F_g/F_p decreases sufficiently in phase 2), the excess deceleration causes the expansion of the core filament. In this case, the central temperature can be lower than the initial temperature. Because the timescale of the cooling in this phase is much shorter than the dynamical time scale (see figures 2.14 and 2.15), the relation between the temperature and the density at the center is not adiabatic. This interesting feature is due to cylindrical geometry and radiative energy transfer, and can be revealed only by RHD simulations.

By the way, a shock wave appears at the outside of scale height (in calculations presented here, typically at $r \sim 3H$). This is conspicuous, however, does not affect significantly on the dynamics of filaments. See also appendix B.

4) Re-contraction phase: We define this phase as the period after the phase 3). This phase corresponds to the region from F to H and from G' to H' in figure 2.9. In the case that filaments are optically thin (corresponding to F - G), the compression heat can escape from the system freely, therefore quasi-isothermal collapse occurs again and the evolution tracks get to be nearly vertical. On the other hand, in the case that filaments are optically thick (corresponding to G-H and G'-H'), filaments collapse on the timescale of radiation cooling though they are no longer isothermal strictly. This phase is similar to so-called Kelvin-Helmholtz contraction in the context of the pre-main sequence contraction.

Note that, filaments are expected to fragment into spherical cores after sufficient radial deceleration (Inutsuka & Miyama, 1997). As shown in figures 2.14 and 2.15, filaments are decelerated significantly before phase 4); thus, it might be meaningless to consider this phase precisely assuming cylindrical geometry.

Cosmic Ray Heated Filaments

In the case of cosmic ray heated filaments, we can divide the evolution into two regimes; whether the central region of a filament is optically deep or not. Optically thin filaments, which correspond to them whose central density is $\rho_c < \rho_\tau$, evolve in the similar way to radiation heated filaments. On the other hand, in optically thick filaments, the process that determines the central temperature is different from radiation heated them. It is always expected that $\Gamma_{\rm CR} = const.$ everywhere, whereas $\Lambda_{\rm eff}$ decreases with the increase of the density and increases with the decrease of the temperature as follows:

$$\Lambda_{\rm eff} = \frac{4\pi\chi T^4}{\tau^2} \propto \rho^{-1} T. \tag{2.38}$$

Therefore $\Lambda_{\rm eff} \sim \Gamma_{\rm CR}$ is expected, unless other heating processes (e.g., compressional heating) exceed them. Consequently the $T_c - \rho_c$ relation is expected as

$$\rho_c \propto T. \tag{2.39}$$

This relation seems to be valid in figure 2.11, e.g., after C". The profile evolution of a cosmic ray heated filament, whose initial temperature is 40 K, is shown in figures 2.16 and 2.17. Indeed it is seen that temperature increase occurs when filaments become optically thick, independent of compression heating.

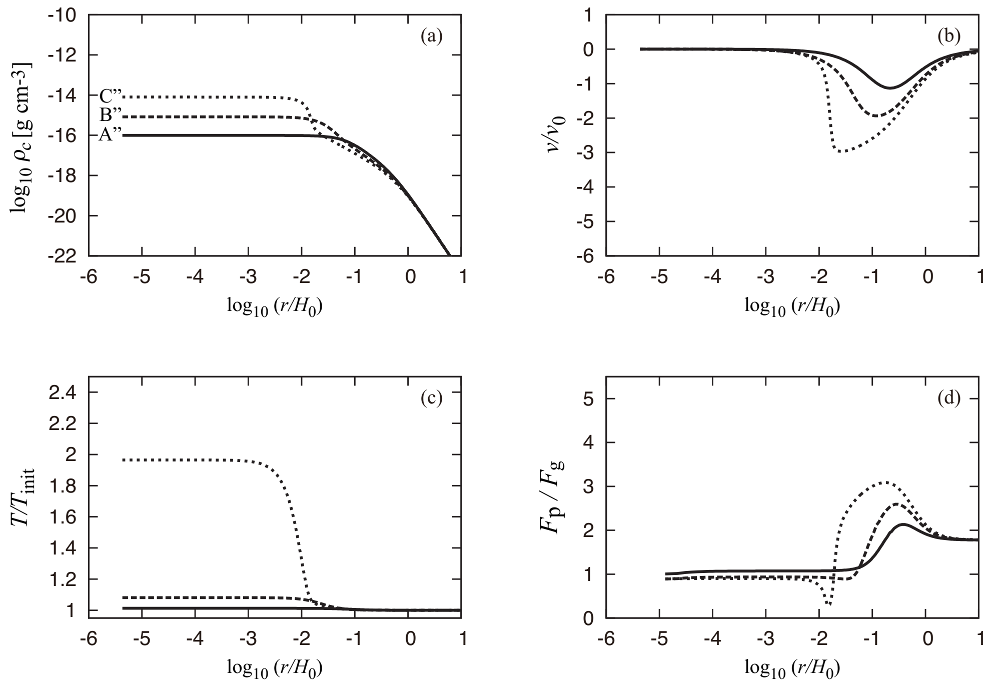

Figure 2.16: Evolutionary sequences of the radial profile of some physical quantities of filaments heated by the cosmic ray, which correspond to 40 K. Alphabet letters correspond to them in figure 2.11.

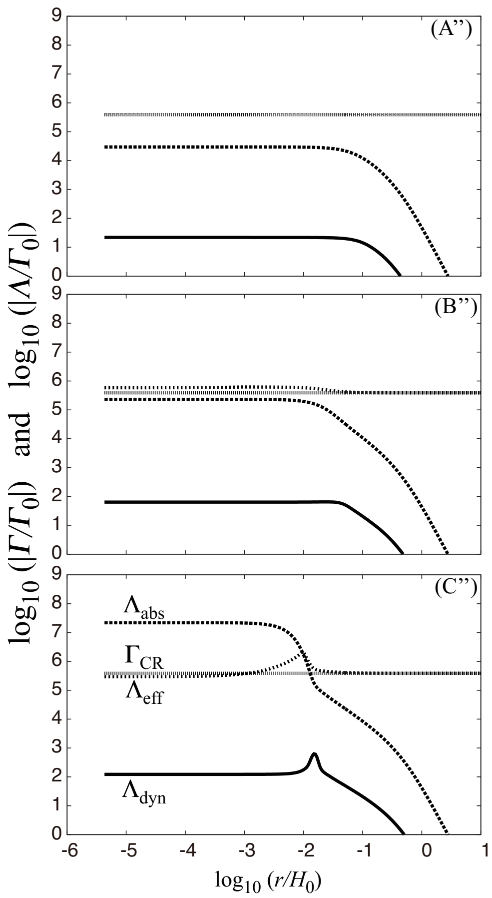

Figure 2.17: Evolution of the radial profile of heating and cooling rates of filaments heated by the cosmic ray that corresponds to 40 K. Alphabet letters correspond to them in figure 2.11.

2.6 Discussion

2.6.1 Mass of Fragments — the Demand for 2DRHD —

The collapsing filaments may fragment into many pieces due to the gravitational instability. The fragmentation process as well as the gravitational collapse characterizes the mass of fragments. The mass may have a connection with the initial mass function of the stellar mass, the mass of brown dwarfs and free-floating planets, and so forth. Thus, the mass of the fragment is an interesting target.

The fragmentation process of the collapsing filaments was investigated by Inutsuka & Miyama (1997) with the smoothed particle hydrodynamics simulations, assuming isothermality. According to their simulations, the filaments, whose line mass is much larger than the equilibrium line mass $m_{\rm eq}$, are not likely to fragment because the time scale of radian contraction is much shorter than one of the fragmentation. On the contrary, the nearly equilibrium filaments fragment into pieces. The separation of the fragments is about 8 times as long as the scale height of the initial filament (Inutsuka & Miyama, 1992). We estimate the mass of the fragments can be expected as follows,

$$M_{\rm frag} \simeq 8 m_{\rm eq}(T) H(\rho_{\rm frag}, T), \tag{2.40}$$

where $\rho_{\rm frag}$ is the central density at which the fragmentation of filaments takes place.

The next question is when the fragmentation occurs. The time at which the fragmentation takes place determines the mass of the fragments. Previously, the mass was investigated as the opacity limited fragmentation mass (Rees, 1976; Silk, 1977). In addition, Masunaga & Inutsuka (1999) reexamine the mass from a different point of view: the fragment mass is determined by the departure from the isothermal collapse, since the radial collapse is expected to be slowed down at that time. Substituting $\rho_{\rm crit}$ defined as equations (2.21) and (2.24) to $\rho_{\rm frag}$ and $T_{\rm init}$ to T in the equation (2.40), they have the fragment mass as a function of the initial temperature. If filamentary clouds are heated by external radiation, then the fragment mass is given by,

$$M_{\rm frag}^{\rm Rad} \approx 0.007 M_{\rm sun} \left(\frac{\chi_{10}}{0.02\,{\rm cm^2\,g^{-1}}} \right)^{-\frac{1}{7+4\beta}} \begin{cases} \left(\frac{T_{\rm init}}{T_s}\right)^{-\frac{3+2\beta}{2}} & \text{for } T_{\rm init} \le T_s, \\ \left(\frac{T_{\rm init}}{T_s}\right)^{\frac{5+2\beta}{6}} & \text{for } T_{\rm init} \ge T_s. \end{cases} \tag{2.41}$$

When filamentary clouds are heated by cosmic rays, the fragment mass is given by,

$$M_{\rm frag}^{\rm CR} \approx 0.007 M_{\rm sun} \left(\frac{\chi_{10}}{0.02\,{\rm cm^2\,g^{-1}}} \right)^{-\frac{1}{7+4\beta}} \begin{cases} \left(\frac{T_{\rm init}}{T_s}\right)^{-\frac{3+2\beta}{2}} & \text{for } T_{\rm init} \le T_s, \\ \left(\frac{T_{\rm init}}{T_s}\right)^{2+\beta} & \text{for } T_{\rm init} \ge T_s. \end{cases} \tag{2.42}$$

However, our calculations imply that regarding $\rho_{\rm crit} = \rho_{\rm frag}$ is not the best quantitative estimation. As discussed in subsection 2.5.3, the deference between $\rho_{\rm crit}$ and $\rho_{\rm frag}$ is not negligible. At least, the density at which the timescale of contraction starts to increase is about one digit higher than $\rho_{\rm crit}$. It should be noted that the fragmentation mass estimated from equations (2.41) and (2.42) involves such uncertainty. Fragments that have several times smaller mass than equations (2.41) and (2.42) could be expected. In addition, slight increase in temperature and deceleration is started before central density reaches $\rho_{\rm crit}$. The influence on $\rho_{\rm frag}$ and mass distribution of fragments is not clear. Therefore, to investigate the fragmentation process precisely, two or three dimensional radiation hydrodynamics simulations that can reproduce the transitions from radial collapse to fragmentation are needed. Based on this motivation, we will present the results of two-dimensional RHD simulations in chapter 4.

2.7 Conclusion of This Chapter

We performed one dimensional radiation hydrodynamics (RHD) simulations using ZEUS-2D with variable Eddington Factor method (VEF) to study the gravitational collapse of filaments in molecular clouds with careful treatments of radiative transfer effects. The followings are main conclusions of this study.

1. The critical density presented in (Masunaga & Inutsuka, 1999), which represents the density at which isothermality break down, is confirmed qualitatively as follows. In the early phase of evolution, namely till compression heating overtake other heating/cooling processes, filaments collapse isothermally. In radiation heated model, after compression heating rate gets to be comparable to effective radiation cooling rate, isothermality breaks down. Note that optical thickness does not affect on the departure from isothermal condition. On the other hand, in cosmic ray heated model, after *either* compression heating rate gets to be comparable to effective radiation cooling rate *or* filaments are optically thickened, isothermality breaks down.

2. The evolution of filaments, which involves complex behavior e.g. bouncing, is investigated specifically. We classified it into evolutionary phases.

3. The implications of the critical density are discussed quantitatively. Indeed the critical density, which is predicted analytically, is valuable as the indicator of appearance of non-isothermality. However, the analysis might involve considerable uncertainty to regard critical density as the density at which fragmentations take

place. To clarify in what condition fragmentations appear, a solution is to perform two dimensional RHD simulations, which will be presented in chapter 4.

Chapter 3

METHOD DEVELOPMENT

3.1 Introduction

Radiation plays a very important role in many astrophysical and astronomical systems as a force, for energy transport, and as a basis for performing synthetic observations. For instance, in the context of star formation, we cannot discuss the thermal structure of collapsing clouds and protostars, the retardation of growth due to radiation, etc. without considering radiation (e.g., Larson, 1969; Masunaga et al., 1998; Masunaga & Inutsuka, 2000; Bate, 2010, 2011). To understand such complicated astrophysical problems, numerical approaches are indispensable. The problem we want to solve, namely the gravitational collapse and fragmentation of filamentary clouds, is not the exception.

The calculation of radiation is highly time-consuming. Ideally, the radiation field can be obtained by solving the equation of radiative transfer, which is the Boltzmann equation for photons. However, the solution of this equation is equivalent to solving a problem of the time evolution of a specific intensity, which is essentially the distribution function of the photons that depends on six variables (space, direction, and frequency). Although various methods for fully solving the equation of radiative transfer have been improved (e.g., the Monte Carlo method (Nayakshin et al., 2009) and the characteristic method (e.g., Nakamoto et al., 2001)), they are computationally too intensive to be coupled with hydrodynamics. Therefore, the equations of radiation hydrodynamics (RHD) are constructed by taking the angular moments of the transfer equation (Mihalas & Mihalas, 1984). To solve the moment equations, a closure relation corresponding to the equation of state in hydrodynamics is needed. For closure, the flux-limited diffusion (FLD) approximation (Alme & Wilson, 1974; Levermore & Pomraning, 1981; Turner & Stone, 2001), M1 closure (Dubroca & Feugeas, 1999; González et al., 2007; Hanawa &

Audit, 2014), and variable tensor Eddington factor (VTEF) (Stone et al., 1992; Hayes & Norman, 2003) have been adopted in recent astrophysical RHD calculations. In various RHD algorithms, FLD has been adopted (e.g., Turner & Stone, 2001; Whitehouse & Bate, 2004; Whitehouse et al., 2005; Hayes et al., 2006; Krumholz et al., 2007; Reynolds et al., 2009; Commerçon et al., 2011; Yang & Yuan, 2012; Commerçon et al., 2014; Kolb et al., 2013) because of its simplicity, robustness, and the low computational cost, although this method has some drawbacks e.g., beaming cannot be reproduced. The M1 closure defined using a higher-order moment than FLD can reproduce anisotropic problems better; nevertheless, this relatively complicated method is being developed but not implemented in many codes (e.g., González et al., 2007; Skinner & Ostriker, 2013). The VTEF can be used to solve for the transfer equation locally and to obtain the relation between the radiation pressure tensor and the radiation energy density. Thus, it has the advantage of accurately describing the angular dependence of the radiation field. However, this approach is seldom adopted because solving the transfer equation requires significant computational resources, especially for multidimensional problems, except for the optically thin regime (Gnedin & Abel, 2001; Petkova & Springel, 2009). The elimination of the angular dependence from the basic equations by taking the moment and the adoption of the gray approximation (dealing only with frequency-integrated quantities) for the RHD equations lead to a time evolution problem that are dependent on the spatial variables and independent of the angular variables, which is equivalent to hydrodynamics.

On the other hand, RHD calculations have a constraint on the time step size. Because the time scale of the processes related to radiation is often much smaller than that of hydrodynamics, an impractically small time step size is required to perform stable calculations explicitly. Therefore, the major approach is to split stiff terms from the basic equations and solve them implicitly. Thanks to the implicit manner, the constraint is reduced to the Courant–Friedrichs–Lewy (CFL) condition of the fluid; however, the numerical treatment tends to be difficult because of divergent and highly nonlinear terms. Most algorithms solve them using the Newton–Raphson (NR) scheme (e.g., Stone et al., 1992; Hayes et al., 2006; González et al., 2007; Reynolds et al., 2009; Tomida et al., 2013). Although the rate of convergence is quadratic if the prediction of the exact solution is sufficiently correct, the prediction is not necessarily easy, and sometimes the convergence becomes considerably worse. Some algorithms utilize simple operator splitting (SOS) to split the divergent terms from the equations including a nonlinearity and then solve them independently without any iterations (Turner & Stone, 2001; Whitehouse & Bate, 2004; Yang & Yuan, 2012). This approach drastically simplifies the problems to be solved, though a critical error is caused because of operator splitting. To reduce this error sufficiently, the time step size must be shortened to the time scale of radiative transfer, which is impractically severe in RHD calculations. Another approach is the linearization (LIN) of equations using a Taylor expansion (Commerçon et al., 2011; Kolb et al., 2013; Commerçon et al., 2014; González et al., 2015). Although the LIN method does not require any iterations and does not cause the error due to operator splitting, a truncation error must arise. If the error is not negligible, the time step size also has to be shortened.

When RHD calculations using the above schemes are performed, the computational cost is defined for respective reasons. In some cases, the cost becomes too large to perform calculations in a feasible computational time. For instance, SOS, which was intentionally or not implemented in RHD algorithms developed by Turner & Stone (2001), Whitehouse & Bate (2004), and Yang & Yuan (2012), required extremely small time step size beyond their expectation. To avoid such accidents, it is needed to investigate and understand the characteristics of these schemes in detail. To clarify the characteristics of these schemes in terms of the numerical cost, we perform two test calculations, namely, the thermal relaxation mode and radiating shock, in the present work. Although there are various factors that affect the numerical cost, we evaluate it using the number of iterations (if necessary) and the constraint on the time step size to obtain a sufficient accuracy. We choose FLD as closure because it is adopted in many RHD codes. Additionally, we add an alternative operator splitting scheme proposed by Douglas & Rachford (1956) (hereafter, DROS). It is the first attempt to apply this scheme to the RHD algorithm, which is expected to expand the range of applications of operator splitting.

Based on the results of test calculations, we choose the better scheme to perform two-dimensional RHD simulations in the regime of $e/E \gg 1$ to investigate the fragmentation of filamentary molecular clouds.

3.2 Equations of Radiation Hydrodynamics

In the present paper, we assume that the velocity of radiating fluid is nonrelativistic, the gas is in local thermodynamic equilibrium (LTE), and the equation of the gas is that for the ideal gas. Using the total frequency-integrated form (the so-called gray approximation), the moment equations of coupled RHD to the order of unity in v/c on a frame comoving with the radiating fluid are given by (Mihalas & Mihalas, 1984; Turner

& Stone, 2001)

$$\frac{D\rho}{Dt} + \rho\boldsymbol{\nabla}\cdot\boldsymbol{v} = 0, \tag{3.1}$$

$$\rho\frac{D\boldsymbol{v}}{Dt} = -\boldsymbol{\nabla}p + \frac{\kappa_{\mathrm{F}}}{c}\boldsymbol{F}, \tag{3.2}$$

$$\begin{aligned}\rho\frac{D}{Dt}\left(\frac{E}{\rho}\right) &= -\boldsymbol{\nabla}\cdot\boldsymbol{F} - \boldsymbol{\nabla}\boldsymbol{v} :\mathbf{P} \\ &\quad +4\pi\kappa_{\mathrm{P}}B - c\kappa_{\mathrm{E}}E,\end{aligned} \tag{3.3}$$

$$\rho\frac{D}{Dt}\left(\frac{e}{\rho}\right) = -p\boldsymbol{\nabla}\cdot\boldsymbol{v} - 4\pi\kappa_{\mathrm{P}}B + c\kappa_{\mathrm{E}}E, \tag{3.4}$$

$$\frac{\rho}{c^2}\frac{D}{Dt}\left(\frac{\boldsymbol{F}}{\rho}\right) = -\boldsymbol{\nabla}\cdot\mathbf{P} - \frac{1}{c}\kappa_{\mathrm{F}}\boldsymbol{F}, \tag{3.5}$$

and

$$p = \frac{k_{\mathrm{B}}}{\mu m_{\mathrm{U}}}\rho T_{\mathrm{gas}} = (\gamma - 1)e. \tag{3.6}$$

Here, the fluid variables ρ, $\boldsymbol{v}$, p, and e are the material mass density, the fluid velocity, the scalar isotropic gas pressure, and the gas energy per unit volume, respectively. The radiation variables E, $\boldsymbol{F}$, $\mathbf{P}$, B, and c, are the total frequency-integrated radiation energy per unit volume, the radiation energy flux, the pressure tensor, the Planck function, and the speed of light, respectively. In equation (3.6), k_B, μ, m_{U}, γ, and T_{gas} are the Boltzmann constant, the mean molecular weight, the atomic mass unit, the specific heat ratio, and the temperature of the fluid, respectively. Here, the Lagrange differential is expressed as $D/Dt \equiv (\partial/\partial t + \boldsymbol{v}\cdot\boldsymbol{\nabla})$. The energy mean, Planck mean, and flux mean opacities are defined by

$$\kappa_{\mathrm{E}} \equiv \int_0^\infty \kappa_\nu E_\nu \, d\nu \Big/ \int_0^\infty E_\nu \, d\nu, \tag{3.7}$$

$$\kappa_{\mathrm{P}} \equiv \int_0^\infty \kappa_\nu B_\nu \, d\nu \Big/ \int_0^\infty B_\nu \, d\nu, \tag{3.8}$$

and

$$\kappa_{\mathrm{F}} \equiv \int_0^\infty \kappa_\nu F_\nu \, d\nu \Big/ \int_0^\infty F_\nu \, d\nu, \tag{3.9}$$

where ν is the frequency, κ_ν, E_ν, B_ν, and F_ν are the frequency dependent absorption opacity per unit volume, the radiation energy density, the Planck function, and the absolute value of the radiation energy flux within the frequency interval of ν – $(\nu + d\nu)$, respectively.

In this study, we assume that $\kappa_{\mathrm{E}} = \kappa_{\mathrm{P}} = \kappa_{\mathrm{F}}$ for simplicity. Moreover, the adoption of an ideal equation of state, the gray approximation, and the comoving frame is also just for simplicity and brevity. The selection of more sophisticated approaches (e.g., multigroup radiation (e.g., González et al., 2015), the mixed-frame approach (Krumholz et al., 2007), etc.) does not affect the essential logic presented in this paper.

The set of RHD equations given here is not complete because an equation that describes the time evolution of the radiation pressure tensor $\mathbf{P}$ is absent. However, this equation ($D\mathbf{P}/Dt = \cdots$) introduces other unknown terms (higher-order moments of the intensity); hence, the system of equations would not be complete. This is called the *closure problem*. To close the moment equation, some relations among E, $\boldsymbol{F}$, and $\mathbf{P}$, which are called *closure relations*, are needed. In the present paper, we adopt the FLD approximation as the closure relation, which was originally proposed by Alme & Wilson (1974) and generalized by Levermore & Pomraning (1981):

$$\boldsymbol{F} = -D\boldsymbol{\nabla} E, \tag{3.10}$$

where $D \equiv c\lambda/\kappa$. An arbitrary function λ is called a flux-limiter, which limits the radiation flux as $|\boldsymbol{F}| \to cE$ in the streaming (optically thin) limit and asymptotically approaches $\lambda \to 1/3$ in the diffusion (optically thick) limit. In this study we employ

$$\lambda\left(R\right) = \frac{2+R}{6+2R+R^2}, \tag{3.11}$$

which was given by Levermore & Pomraning (1981), where

$$R \equiv \frac{|\boldsymbol{\nabla} E|}{\kappa E}. \tag{3.12}$$

By adding the closure relation (3.10) to equations (3.1) – (3.6), the equations are closed, where equation (3.5) is replaced with equation (3.10). Using Levermore's FLD theory, the radiation pressure tensor is given by

$$\mathbf{P} = \mathbf{f}E, \tag{3.13}$$

with the Eddington factor tensor $\mathbf{f}$ defined as

$$\mathbf{f} = \frac{1}{2}\left(1-f\right)\mathbf{I} + \frac{1}{2}\left(3f-1\right)\hat{\boldsymbol{n}}\hat{\boldsymbol{n}}, \tag{3.14}$$

where $\hat{\boldsymbol{n}} \equiv \boldsymbol{\nabla} E/\left|\boldsymbol{\nabla} E\right|$, and $\mathbf{I}$ is the unit tensor. The nondimensional scalar function f called the Eddington factor is defined as

$$f = \lambda + \lambda^2 R^2. \tag{3.15}$$

3.3 Implicit Schemes to Solve the RHD Equations

The moment equations of RHD in equations (3.1)–(3.5) include extremely stiff terms because of the matter-radiation interaction and radiative transfer. Therefore, the use of a straightforward explicit manner that needs a sufficiently small time step size to satisfy the CFL condition for stability is practically too inefficient. To avoid this problem, most RHD algorithms split the stiff terms from the energy equations and implicitly solve the separated equations (e.g., Hayes et al., 2006; Commerçon et al., 2011; Kolb et al., 2013; Bryan et al., 2014). In the same way, we explicitly solve

$$\frac{D\rho}{Dt} + \rho\boldsymbol{\nabla}\cdot\boldsymbol{v} = 0, \tag{3.16}$$

$$\rho\frac{D\boldsymbol{v}}{Dt} = -\boldsymbol{\nabla}p + \frac{\kappa}{c}\boldsymbol{F}, \tag{3.17}$$

$$\rho\frac{D}{Dt}\left(\frac{E}{\rho}\right) = 0, \tag{3.18}$$

and

$$\rho\frac{D}{Dt}\left(\frac{e}{\rho}\right) = 0, \tag{3.19}$$

and implicitly solve

$$\frac{\partial E}{\partial t} = -\boldsymbol{\nabla}\cdot\boldsymbol{F} - \boldsymbol{\nabla}\boldsymbol{v}:\mathbf{P} + 4\pi\kappa B - c\kappa E, \tag{3.20}$$

and

$$\frac{\partial e}{\partial t} = -p\boldsymbol{\nabla}\cdot\boldsymbol{v} - 4\pi\kappa B + c\kappa E, \tag{3.21}$$

afterwards (Hayes et al., 2006). During an implicit update, ρ and $\boldsymbol{v}$ are explicitly dealt with (i.e., fixed at the previous value). Here, we include a compression heating term in equation (3.21) according to the scheme of Hayes et al. (2006), although the term can be included in equation (3.19) because it is not stiff. For simplicity, κ and λ are explicitly dealt with.

We do not constrain the specific method to solve the equations (3.16)–(3.19), because the present work focuses on a scheme that implicitly solves equations (3.20) and (3.21). So, ZEUS (Stone & Norman, 1992; Hayes et al., 2006) is adopted for that.

Equations (3.20) and (3.21) are nonlinear owing to the Planck function and need matrix calculations owing to the flux divergence term. In the following subsections, we introduce some schemes to solve such nonlinear simultaneous equations based on a finite difference method on grids: NR, operator splitting, and LIN, and show their implementation in this work.

3.3.1 Newton–Raphson Iteration Scheme

The NR iteration scheme is a popular method for solving nonlinear simultaneous equations because of its efficiency. Some astrophysical RHD algorithms also adopt this scheme to solve the equations of energy implicitly (e.g., Hayes et al., 2006; Reynolds et al., 2009; Tomida et al., 2013, for the FLD approximation). In a similar way, we implement the NR scheme as follows. We define the functions $f_i^{(a)}$ as follows:

$$\begin{aligned} f_i^{(1)} = E_i^{n+1} - E_i^n \\ -\Delta t(4\pi\kappa_i B_i^{n+1} - c\kappa_i E_i^{n+1} \\ -\boldsymbol{\nabla}\cdot\boldsymbol{F}_i^{n+1} - \boldsymbol{\nabla}\boldsymbol{v} :_i \mathbf{P}_i^{n+1}), \end{aligned} \tag{3.22}$$

and

$$\begin{aligned} f_i^{(2)} = e_i^{n+1} - e_i^n \\ -\Delta t(-4\pi\kappa_i B_i^{n+1} + c\kappa_i E_i^{n+1} \\ -p_i\boldsymbol{\nabla}\cdot\boldsymbol{v}_i), \end{aligned} \tag{3.23}$$

where the subscript i means the grid number. The superscripts n and $n+1$ represent before and after the implicit update, respectively. The time step size is Δt. To obtain an acceptable numerical solution that should approximately satisfy $f_i^{(1)} = f_i^{(2)} = 0$ at all grid points,

$$\mathbf{J}_f\left(\boldsymbol{x}\right)\boldsymbol{\delta x} = -\boldsymbol{f}\left(\boldsymbol{x}\right) \tag{3.24}$$

iteratively calculated until the error becomes sufficiently small. In equation (3.24), $\boldsymbol{x}$ is the vector $(E_i, e_i)^{\mathrm{T}}$, $\boldsymbol{\delta x}$ is the correction vector, and $\mathbf{J}_f$ is the Jacobian matrix. Equation (3.24) is a set of simultaneous linear equations, which requires the calculation of a sparse band matrix using some iterative method (e.g., the conjugate gradient method) in the multidimensional problem. However, we use a direct method because it releases us from considering the accuracy of calculating the matrix, and the numerical tests performed in present study are one-dimensional. In this paper, convergence is achieved when all values of $\delta e_i/e_i$ and $\delta E_i/E_i$ become less than the criterion $\varepsilon = 10^{-5}$. If the iteration does not converge in 20 cycles, the NR iteration is said to not converge.

The rate of the convergence of NR scheme is quadratic if the prediction of the solution is adequately correct. Additionally, the results are assumed to be more reliable because the degree of approximations is lower than those in other two schemes. However, the iteration does not always converge. In some algorithms, the iteration is restarted with a smaller Δt when the NR iteration does not converge for a defined criterion (e.g., Hayes et al., 2006; Tomida et al., 2013). This approach actually improves the convergence, but inevitably causes a longer calculation time. In particular, the convergence becomes fatally worse in problems that involve extremely optically thin regions, as shown in the following section and appendix E.

3.3.2 Operator Splitting Scheme

The approach of operator splitting or a fractional step, which divides a complex problem involving various physics into some simpler problems that can be dealt with more easily, is also commonly used to compose astrophysical algorithms (Ciarlet & Lions, 1990; Stone & Norman, 1992). In accordance with this scheme, we can drastically simplify equations (3.20) and (3.21). In this subsection, we first introduce the previously used SOS scheme. Then, we present an alternative operator splitting scheme developed by Douglas & Rachford (1956), which is expected to provide better performance. The use of the latter scheme is the first attempt in RHD algorithms.

Simple Operator Splitting Scheme

Consider the differential equation

$$\frac{dy}{dt} = \mathcal{L}_1(y) + \mathcal{L}_2(y), \tag{3.25}$$

where $\mathcal{L}_1$ and $\mathcal{L}_1$ are different operators that represent different processes. According to operator splitting scheme, the time-implicit finite difference approximation of equation (3.25) is divided into

$$\frac{y^{n+1/2} - y^n}{\Delta t} = L_1\left(y^{n+1/2}\right), \tag{3.26}$$

and

$$\frac{y^{n+1} - y^{n+1/2}}{\Delta t} = L_2\left(y^{n+1}\right), \tag{3.27}$$

where L_1 and L_2 are the finite difference approximations of $\mathcal{L}_1$ and $\mathcal{L}_2$ respectively. In the present paper, we call this the SOS scheme. This scheme is unconditionally stable, and the accuracy is first-order (Ciarlet & Lions, 1990).

We apply the SOS scheme to equations (3.20) and (3.21) as follows. First, from the time step n (just after the explicit update) to the intermediate one $n + 1/2$, we solve

$$\begin{aligned}\frac{E_i^{n+1/2} - E_i^n}{\Delta t} &= -\boldsymbol{\nabla}\boldsymbol{v}_i\mathbf{:}\mathbf{P}_i^{n+1/2} \\ &\quad +4\pi\kappa_i B_i^{n+1/2} - c\kappa_i E_i^{n+1/2},\end{aligned} \tag{3.28}$$

and

$$\frac{e_i^{n+1/2} - e_i^n}{\Delta t} = -p_i^{n+1/2} \boldsymbol{\nabla} \cdot \boldsymbol{v}_i \\ -4\pi\kappa_i B_i^{n+1/2} + c\kappa_i E_i^{n+1/2}. \tag{3.29}$$

Next, from the time step $n + 1/2$ to $n + 1$, we solve

$$\frac{E_i^{n+1} - E_i^{n+1/2}}{\Delta t} = -\boldsymbol{\nabla} \cdot \boldsymbol{F}_i^{n+1}, \tag{3.30}$$

and

$$\frac{e_i^{n+1} - e_i^{n+1/2}}{\Delta t} = 0. \tag{3.31}$$

Note that step $n + 1/2$ is an intermediate numerical step; thus, it does not correspond to a time series (namely, $t^{n+1} - t^{n+1/2} = t^{n+1/2} - t^n = \Delta t$).

Because the opacity is explicitly dealt with, equations (3.28) and (3.29) lead to a local quadratic equation with one unknown variable (Turner & Stone, 2001), which can be easily solved using an analytical method. In the present study, we solve it using Ferrari's method. If the opacity is implicitly dealt with, we can iteratively solve using the NR method, bisection method, etc. On the other hand, equation (3.30) is a simple diffusion equation, which is expressed using simultaneous linear equations, and can be solved using proper methods. In the present study, we solve it using a direct method for the same reasons as equation (3.24).

This scheme has attractive advantages. The separation of a complex problem into some simple problems allows us to choose a numerical scheme that is more efficient, more robust, and easier to implement. Additionally, we do not need to take care of the convergence of an iteration scheme. However, the scheme has a critical disadvantage, namely, SOS is not valid if Δt is too large. To obtain sufficiently correct solution, Δt must be smaller than the radiation time scale. In the time-explicit operator splitting scheme used in, e.g., magnetohydrodynamics, the CFL condition constrains Δt to be smaller than the physical time scale. On the other hand, the time-implicit operator splitting scheme described here has no such constraints; thus, the error due to SOS tends to be extremely large when solving problems involving RHD. To avoid this problem, a sufficiently small time step size is needed, which is typically $D/(\Delta x)^2$ (Turner & Stone, 2001; Whitehouse & Bate, 2004). If such a small time step size can be adopted, some explicit methods that do not need matrix calculations would be better.

Douglas and Rachford Operator Splitting Scheme

To reduce the error due to operator splitting, we modify SOS without losing consistency by adding $L_2\left(y^n\right)$ to the R.H.S. of equation (3.26) (resp. (3.27)) with a positive (resp. negative) sign as follows:

$$\frac{y^{n+1/2}-y^n}{\Delta t}=L_1\left(y^{n+1/2}\right)+L_2\left(y^n\right), \tag{3.32}$$

and

$$\frac{y^{n+1}-y^{n+1/2}}{\Delta t}=L_2\left(y^{n+1}\right)-L_2\left(y^n\right). \tag{3.33}$$

This kind of operator splitting is classified into the scheme developed by Douglas & Rachford (1956) in the context of an advection diffusion problem; thus, we call this the DROS scheme in the present paper. This scheme is unconditionally stable, and the accuracy is first-order (Douglas & Rachford, 1956; Ciarlet & Lions, 1990). The terms on the R.H.S. are partially implicitly and partially explicitly dealt with; neverthless, equation (3.32) resembles the original equation in equation (3.25). Thus, a reduction in the error is expected compared with SOS. From this point of view, equation (3.33) can be interpreted as a modification to guarantee numerical stability. The improvement from SOS to DROS is outstanding, especially when the system is roughly in equilibrium, i.e., $dy/dt=\mathcal{L}_1\left(y\right)+\mathcal{L}_2\left(y\right)\sim 0$. The SOS scheme breaks the equilibrium and artificially changes y, whereas the DROS scheme does not significantly do so.

Using the DROS scheme, we modify equations (3.28)–(3.31) as follows. First, from the time step n to $n+1/2$, we solve

$$\begin{aligned}\frac{E^{n+1/2}-E^n}{\Delta t}&=-\boldsymbol{\nabla}\boldsymbol{v}:\mathbf{P}^{n+1/2}\\&+4\pi\rho\kappa B^{n+1/2}-c\rho\kappa E^{n+1/2}-\boldsymbol{\nabla}\cdot\boldsymbol{F}^n,\end{aligned} \tag{3.34}$$

and

$$\begin{aligned}\frac{e^{n+1/2}-e^n}{\Delta t}&=-p^{n+1/2}\boldsymbol{\nabla}\cdot\boldsymbol{v}\\&-4\pi\rho\kappa B^{n+1/2}+c\rho\kappa E^{n+1/2}.\end{aligned} \tag{3.35}$$

Next, from the time step $n+1/2$ to $n+1$, we solve

$$\frac{E^{n+1}-E^{n+1/2}}{\Delta t}=-\boldsymbol{\nabla}\cdot\boldsymbol{F}^{n+1}+\boldsymbol{\nabla}\cdot\boldsymbol{F}^n, \tag{3.36}$$

and

$$\frac{e^{n+1}-e^{n+1/2}}{\Delta t}=0. \tag{3.37}$$

The additional term $\boldsymbol{\nabla} \cdot \boldsymbol{F}^n$ is already known from equation (3.36) in the previous time step. Namely, the differences between SOS and DROS in a code implementation are very small.

3.3.3 Linearization

A major factor that makes numerical treatment difficult is the existence of a Planck function, which is highly nonlinear. Therefore, we can approximately linearize the function using a Taylor expansion and remove this difficulty (Hayes & Norman, 2003; Commerçon et al., 2011).

We approximate the Planck function $B^{n+1} = (\sigma/\pi)\left(T_{\mathrm{gas}}^{n+1}\right)^4$, where σ is the Stefan–Boltzmann constant, using following approximation

$$\left(T_{\mathrm{gas}}^{n+1}\right)^4 \approx 4\left(T_{\mathrm{gas}}^{n}\right)^3 T_{\mathrm{gas}}^{n+1} - 3\left(T_{\mathrm{gas}}^{n}\right)^4, \tag{3.38}$$

assuming that the changes in the gas temperature are small within a time step. Using the above approximation, equations (3.20) and (3.21) lead to a set of simultaneous linear equations with only E_i^{n+1} (Commerçon et al., 2011). In the present study, we solve it using a direct method for the same reasons as equation (3.24).

The truncation error due to the approximation in equation (3.38) increases as Δt increases. The term that is affected by the error is $4\pi\kappa B$; thus, if the term is dominant and Δt is larger than $\min\left(e, E\right)/4\pi\kappa B$, the energy exchange between the fluid and the radiation can no longer be expressed correctly. To reduce the error, an adequate reduction in Δt is required, which leads to an increase in the calculation time (see appendix F).

3.4 Numerical Tests

The purpose of this work is to compare the numerical cost of the four schemes described in the previous section. Although various factors that would determine the "numerical cost" can be assumed, we define this term using the number of iterations and the size of Δt, which are needed to obtain a sufficiently correct solution. Namely, we assume that the value of the "numerical cost" is proportional to these factors. To evaluate the cost of the four schemes, the following two numerical tests are solved. The first test is a problem on the thermal relaxation mode of radiation (Mihalas & Mihalas, 1984). This problem involves the thermal relaxation between the fluid and the radiation field; thus, it is useful to verify whether or not the interaction is correctly reproduced. Additionally, the small number of variables that determine the character of the relaxation is needed; thus, we can carry out a parameter study by changing the optical thickness and Δt. The second test is a problem on radiating shock (Mihalas & Mihalas, 1984). This problem involves not only the matter-radiation interaction but also dynamic fluid motion with a shock wave. Additionally, this problem was used as a numerical test of RHD algorithms by many authors (e.g., Ensman, 1994; Turner & Stone, 2001; Hayes et al., 2006; Yang & Yuan, 2012); thus, we can directly compare our results with their results.

3.4.1 Thermal Relaxation Mode

Consider a field of temperature perturbations imposed on a infinite, static, homogeneous, and gray medium, which is initially in radiative equilibrium, and $e \gg E$. The fluctuations should be quasistatically smoothed out by the radiation at a ratio defined by $n\left(k\right) = -\left(\partial\phi/\partial t\right)/\phi$, where ϕ is the amplitude of a mode whose wave number is k.

According to the linear analysis presented by Spiegel (1957), the dispersion relation for the thermal relaxation mode of a radiating fluid is given by

$$n(k)_{\mathrm{ana}} = \nu\left[1 - \left(\frac{\kappa}{k}\right)\cot^{-1}\left(\frac{\kappa}{k}\right)\right], \tag{3.39}$$

where

$$\nu = \frac{16\sigma\kappa\left(T^0_{\mathrm{gas}}\right)^3}{c_v}. \tag{3.40}$$

In equation (3.40), T^0_{gas} and c_v represent the unperturbed temperature and the heat capacity at a constant volume per unit volume, respectively. On the other hand, assuming isotropic media in which the Eddington approximation can be invoked, the rate is replaced by the following (Unno & Spiegel, 1966):

$$n_{\mathrm{Edd}}(k) = \frac{\nu}{1 + 3\left(\kappa/k\right)^2}. \tag{3.41}$$

Because FLD cannot express the anisotropy of the radiation in the case where $|\nabla E|$ is extremely small, n_{Edd} instead of n_{ana} is expected as the numerical solution. In such a semi-uniform radiation field, R defined by equation (3.12) is tiny and independent of the optical depth. Thus, the flux-limiter becomes 1/3, which is identical to the case of the diffusion limit, even if the media is optically thin. Therefore, $f \to 1/3$, which leads to the identical result of the Eddington approximation.

We calculate this problem using $\rho = 1.65 \times 10^{-14}\,\mathrm{g\,cm^{-3}}$, $\kappa = 3.3 \times 10^{-16}\,\mathrm{cm^{-1}}$, and $T^0_{\mathrm{gas}} = 10\,\mathrm{K}$. To obtain $c_v = \rho\mathcal{R}/\{\mu(\gamma - 1)\}$, we assume $\mu = 2.3$ and $\gamma = 5/3$, where $\mathcal{R}$ is the gas constant of an ideal gas. The above assumptions resemble an environment

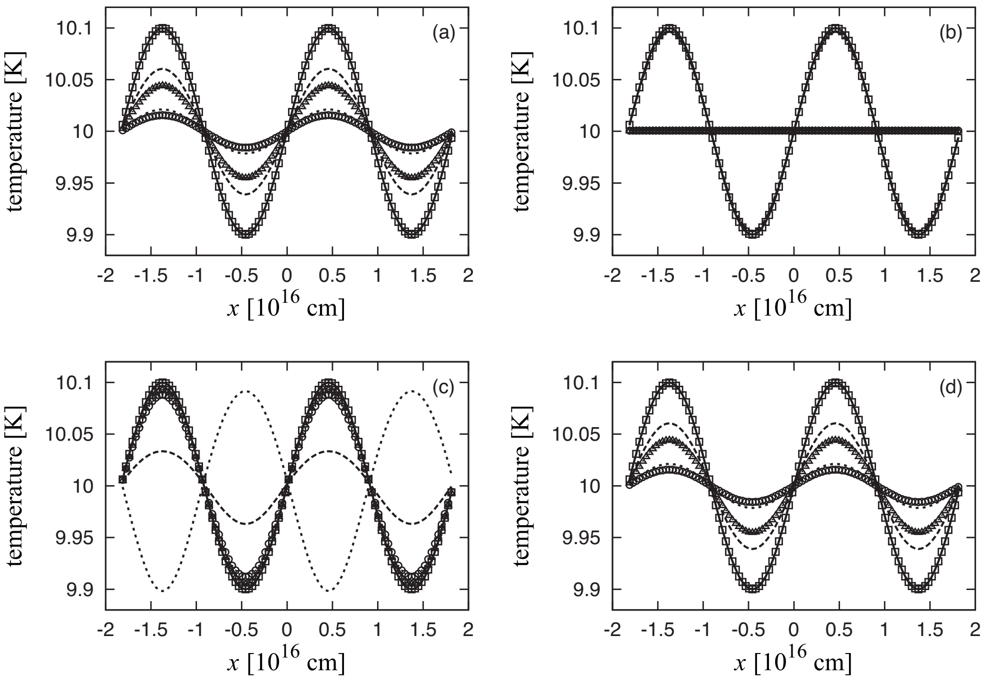

Figure 3.1: Evolution of the temperature profiles in the thermal relaxation mode, where $\Delta t = 3 \times 10^8$ s. Solid curves (resp. open squares), long dashed curves (resp. open triangles), and short dashed curves (resp. open circles) represent the gas (reps. radiation) temperature at $(0.0, 0.6, \text{and}\, 2.4) \times 10^{10}$ s, respectively. The schemes used are (a) the NR method, (b) SOS, (c) DROS, and (d) LIN.

established in the early phase of protostar formation. The initial amplitude of the fluctuations is 1%. The computational domain $L = 3.662 \times (10^{14},\, 10^{16},\, 10^{18})$ cm involves two sine waves, which correspond to $k/\kappa = 100, 1, 0.01$. We uniformly divide the domain into 100 grids. To mimic an infinite wave, a periodic boundary condition is imposed.

The evolution of the temperature profiles, where $k/\kappa = 1$, obtained using the NR method, SOS, DROS, and LIN are shown in figures 3.1 ($\Delta t = 3 \times 10^8\,$s) and 3.2 ($\Delta t = 3 \times 10^6\,$s). Here, the "radiation temperature" is defined by $\{cE/\left(4\sigma\right)\}^{1/4}$. The results obtained by the NR method and LIN are similar and independent of Δt, and their relaxation rates are identical to $n_{\rm Edd}$ within 1%. On the contrary, the SOS results are remarkably different, and the relaxation rate is significantly wrong because of the error due to operator splitting. In contrast to SOS, DROS gives an incorrect solution for $\Delta t = 3 \times 10^8\,$s but a better one for $\Delta t = 3 \times 10^6\,$s.

To compare the four schemes, we change Δt and k/κ and check whether or not $n_{\rm Edd}$ is reproduced. Hereafter, we use the expression "correct" in this subsection instead of

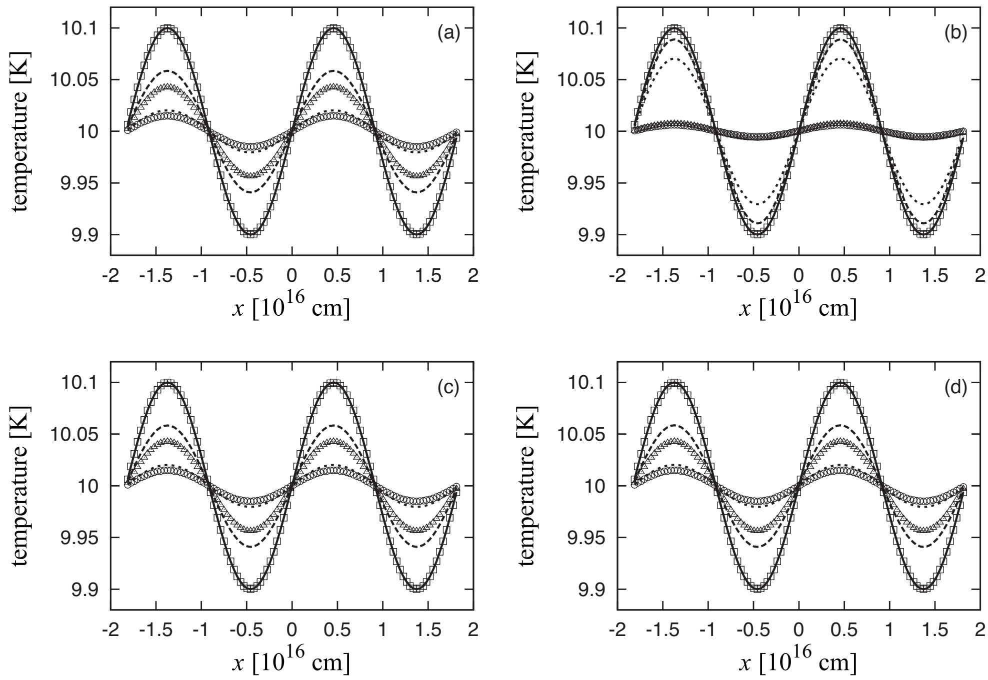

Figure 3.2: Evolution of the temperature profiles in the thermal relaxation mode, where $\Delta t = 3 \times 10^6$ s. The description of panels and curves are the same as those in figure 3.2 but for a different time step size.

saying that the obtained thermal relaxation rate became identical to $n_{\rm Edd}$ to an accuracy of 1% after the proper time from the initial condition. The results obtained using the NR method, SOS, DROS, and LIN are shown in figures 3.3, 3.4, 3.5, and 3.6, respectively. The definitions of three types of lines are shown in the figures, where $\Delta x = L/100$ and c_s is the speed of sound. Here, R that is needed to define D is replaced with k/κ.

The iteration does not converge for the NR method and NaN or the negative energy appears for other schemes in the case of $\Delta t > 1/n_{\rm Edd}$, which is reasonable because the relaxation time scale is $1/n_{\rm Edd}$. From figure 3.3, we can see that the convergence of the NR iteration is extremely bad for the optically thin problems. In figure 3.7, the relations between $n_{\rm NR}$ and $\varepsilon_{\rm max}^{n_{\rm NR}}$ for various optical thickness and values of Δt during an update from $t = 0$ to $t = \Delta t$ are shown, where $n_{\rm NR}$ is the number of NR iterations and

$$\varepsilon_{\rm max}^{n_{\rm NR}} \equiv \max_i \left[\left| \frac{e_i^{n_{\rm NR}+1} - e_i^{n_{\rm NR}}}{e_i^{n_{\rm NR}}} \right|, \left| \frac{E_i^{n_{\rm NR}+1} - E_i^{n_{\rm NR}}}{E_i^{n_{\rm NR}}} \right| \right]. \tag{3.42}$$

Here, the terminating condition is omitted. The time step size is evaluated using $\Delta t_{\rm c} \equiv \Delta x/c$ and $\Delta t_{\rm fluid}$, which is given using the fluid CFL condition (e.g., the ZEUS algorithm (Stone & Norman, 1992)) and is nearly equal to $\Delta x/c_s$. If the wavelength is optically thick, the NR iteration converges well within several cycles. However, for a smaller optical thickness and Δt, it is more difficult for the NR iteration to converge (see also appendix E). From figure 3.4, it is observed that the error due to SOS is critical. As shown in figures 3.1 and 3.2, SOS cannot reproduce the relaxation process at all unless Δt is shortened to $\Delta x^2/D$, which is practically unrealistic. From figure 3.5, it is shown that DROS reproduces the correct solution if $\Delta t < 0.001/n_{\rm Edd}$; namely, the modification from SOS to DROS relaxes the constraint on Δt. From figure 3.6, we can see that LIN is overwhelmingly more robust than the other schemes. Correct solutions are obtained independent of the optical thickness, with the use of a larger value of Δt, and without any iterations. This is because the change in the temperature in one time step is sufficiently small and the constraint of the linearizing approximation is well satisfied in this test problem.

According to this problem, LIN is the most efficient scheme with respect to the numerical cost. If the wavelength is optically thin, the convergence of the NR method is critically worse and significantly inferior to LIN; thus, DROS is the second-best. On the other hand, if the wavelength is optically thick, the NR method is the second-best because the NR iteration converges within several cycles. In any case, SOS is not practically useful.

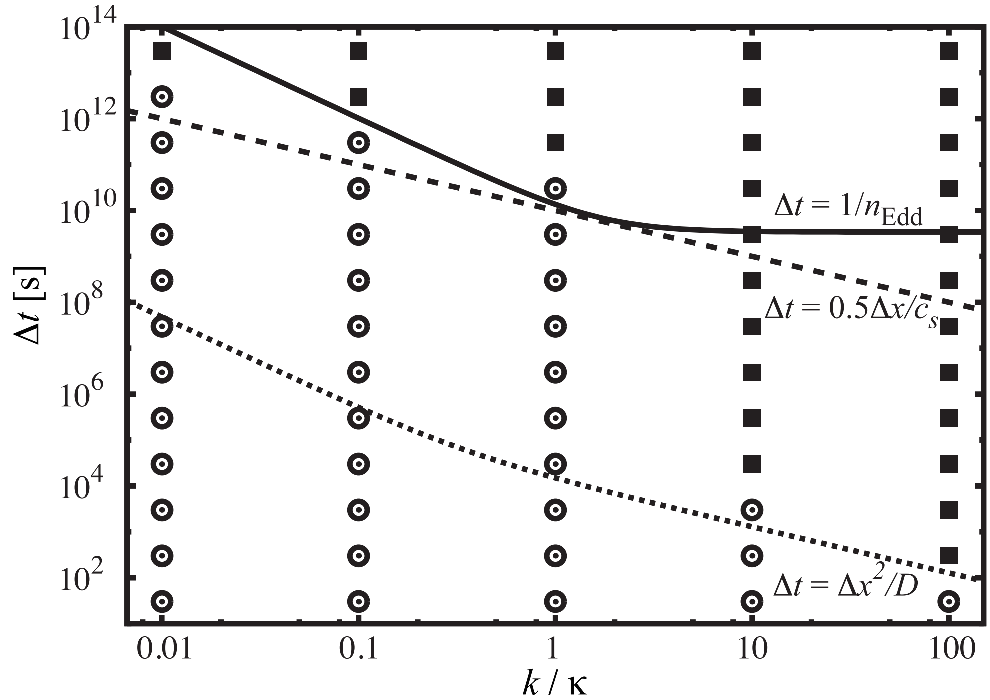

Figure 3.3: Results of the thermal relaxation mode. Open circles mean that "correct" solutions are obtained. Filled squares indicate that the NR iteration does not converge within the criteria defined in the text body. Here, the NR scheme is used.

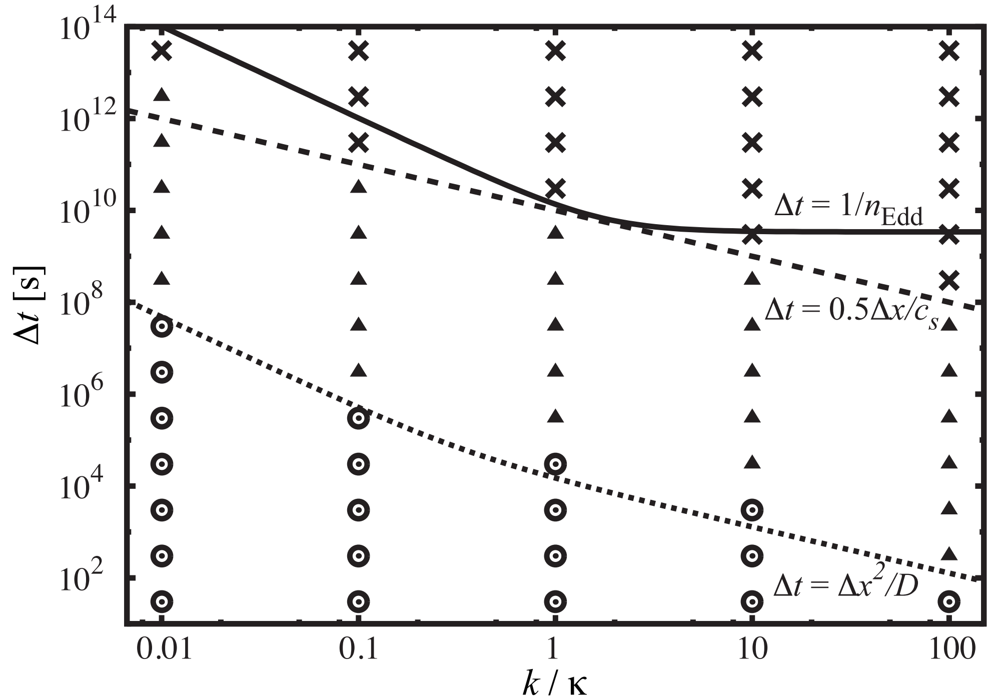

Figure 3.4: Results of the thermal relaxation mode. Filled triangles mean that "incorrect" solutions are obtained. Crosses exhibit that NaN or a negative energy appears. The other marks are the same as those in figure 3.3. Here, SOS is used.

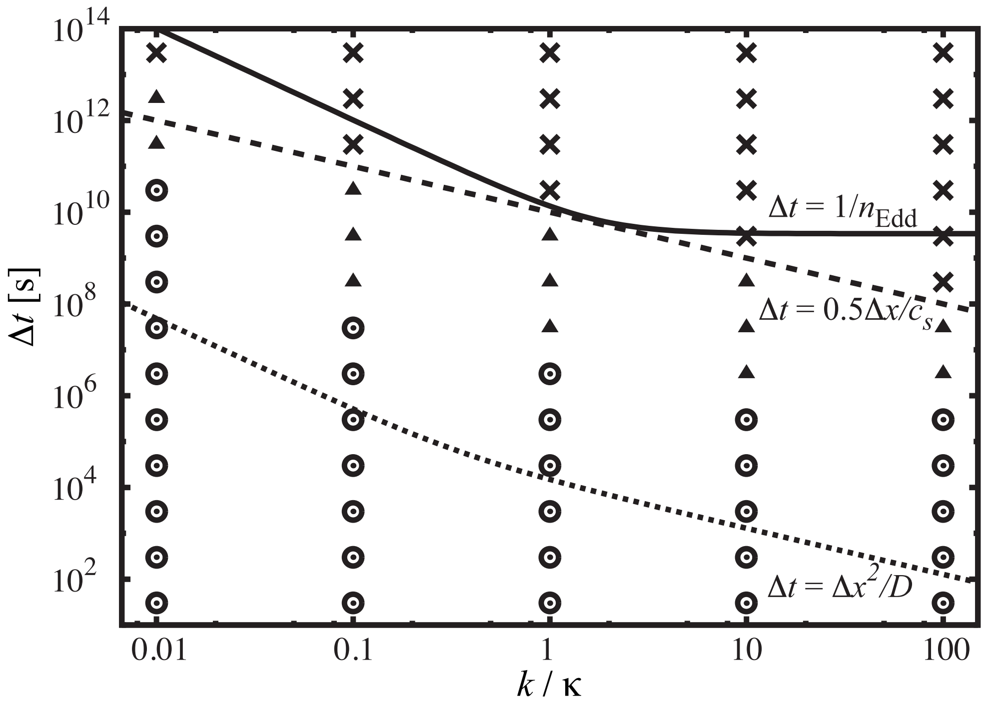

Figure 3.5: Results of the thermal relaxation mode. The marks are the same as those in figures 3.3 and 3.4. Here, DROS is used.

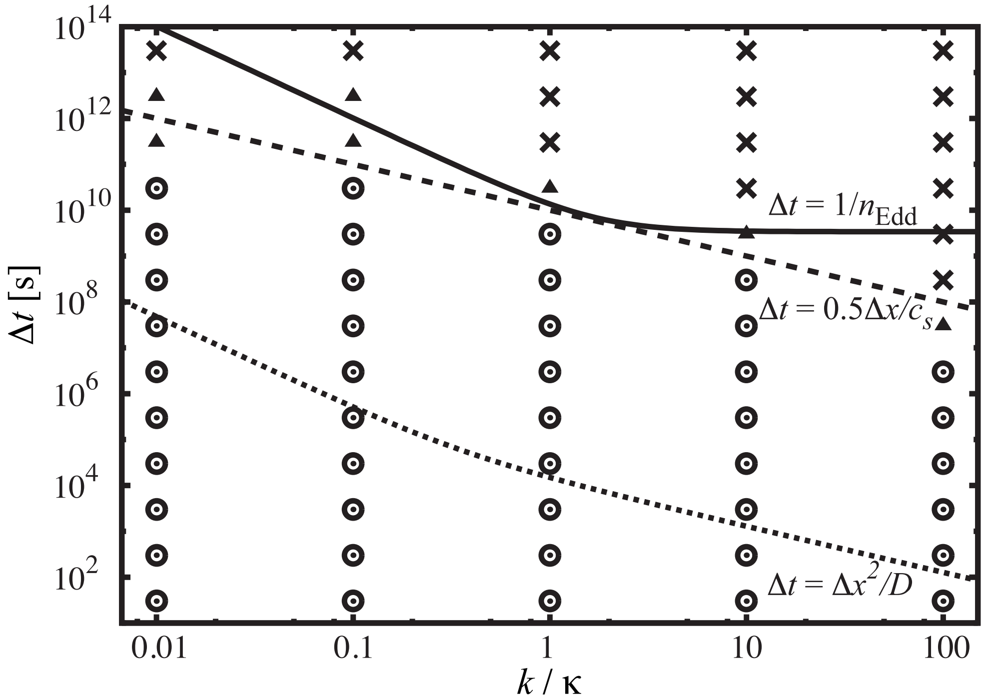

Figure 3.6: Results of the thermal relaxation mode. The marks are the same as those in figures 3.3 and 3.4. Here, LIN is used.

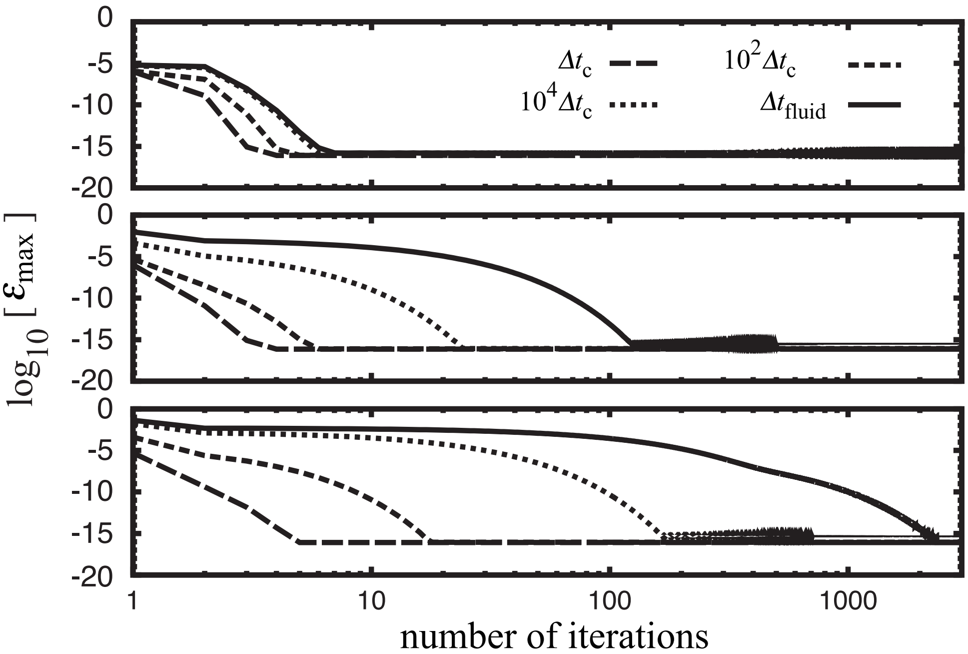

Figure 3.7: Convergence of the NR iteration. From the top panel to the bottom panel, the optically thick ($k/\kappa = 0.01$, $\Delta t_{\rm c} = 0.61 \times 10^8\,{\rm s}$, $\Delta t_{\rm fluid} = 0.74 \times 10^{12}\,{\rm s}$), intermediate ($k/\kappa = 1$, $\Delta t_{\rm c} = 0.61 \times 10^6\,{\rm s}, \Delta t_{\rm fluid} = 0.74 \times 10^{10}\,{\rm s}$), and thin ($k/\kappa = 100$, $\Delta t_{\rm c} = 0.61 \times 10^4\,{\rm s}, \Delta t_{\rm fluid} = 0.74 \times 10^8\,{\rm s}$) cases are plotted.

3.4.2 Radiating Shock Waves

A homogeneous radiating fluid, which initially moves along the positive direction to the negative direction along the x-axis one-dimensionally and uniformly, is considered. The fluid encounters a wall at $x = 0$ when $t = 0$ with a supersonic velocity v. According to previous works (e.g., Ensman, 1994), we choose $v = -6\ \mathrm{km\,s^{-1}}$ (called subcritical) and $v = -20\ \mathrm{km\,s^{-1}}$ (called supercritical). The calculation domain whose length is $7 \times 10^{10}\,\mathrm{cm}$ is initially filled with an ideal gas. The gas density and mean molecular weight are $7.78 \times 10^{-10}\,\mathrm{g\,cm^{-3}}$ and 0.5, respectively. The initial gas temperature is 85 K at $x = 0$ and 10 K at the outer boundary, and the profile between them is linear. The initial radiation energy is assumed to be in equilibrium with the matter. We assume a purely absorbing medium with a constant opacity of $3.1 \times 10^{-10}\,\mathrm{cm^{-1}}$; thus, the mean free path of a photon is about 5% of the domain size. We determine Δt using the fluid CFL condition. For the NR and LIN schemes, we use the time step size $\Delta t_{\mathrm{fluid}}$ that satisfies the fluid CFL condition (Stone & Norman, 1992). For SOS and DROS schemes, we also use $(1/32)\,\Delta t_{\mathrm{fluid}}$. The calculating domain is uniformly divided into 512 zones.

The time evolutions of the temperature profiles using the four schemes are shown in figures 3.8–3.13. In the present work we fix the grids; however, to compare our results with previous works directly, we rewrite $x - vt$ as x.

The results obtained by the NR scheme are shown in figure 3.8. The profiles exhibit good agreement with those obtained by ZEUS-MP (Hayes et al., 2006), which uses almost the same RHD algorithm based on the NR method and FLD. This problem is optically thick; thus, the NR iteration converges well, typically within several cycles. Figures 3.9 and 3.10 show the results for the SOS scheme. The expected interaction between the fluid and the radiation field is not reproduced because of the error due to operator splitting. To obtain solutions using the SOS scheme with a sufficiently correct accuracy, we have to shorten Δt to about $10\Delta x^2/D$ (Turner & Stone, 2001; Whitehouse & Bate, 2004). On the other hand, DROS exhibits better results than SOS, as shown in figures 3.11 and 3.12. If we use $\Delta t_{\mathrm{fluid}}$, nonphysical perturbations are formed. However, the perturbations become acceptably damped when decreasing Δt to $(1/32)\,\Delta t_{\mathrm{fluid}}$. The results obtained by the LIN scheme are shown in figure 3.13, which closely resemble those obtained by the NR scheme.

From the perspective of the numerical cost for this test problem, the LIN scheme is the most efficient scheme. The NR scheme, which requires several NR iterations, is the next best. DROS requires a calculation time that is about 10 times longer than the NR scheme because of the constraint on Δt, whereas SOS is practically useless.

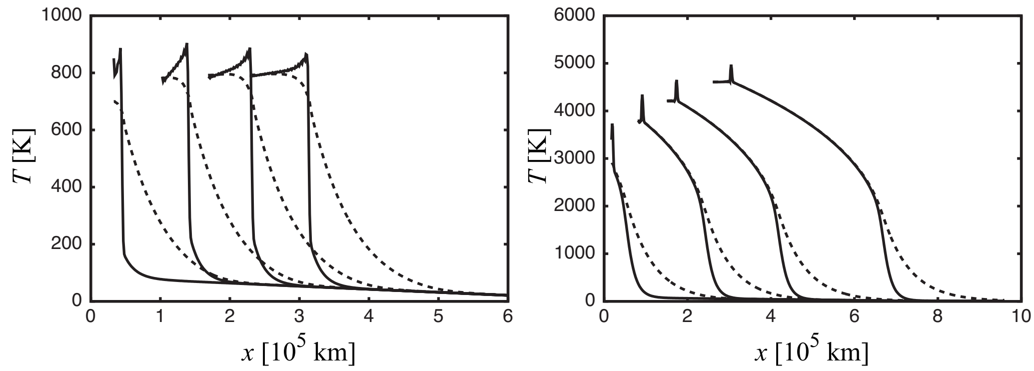

Figure 3.8: Gas (solid curves) and radiation (dashed curves) temperature profiles versus the comoving coordinate x for subcritical (left panel) and supercritical (right panel) radiating shocks. The times shown for the subcritical radiation shock are 5.4×10^3, 1.7×10^4, 2.8×10^4, and 3.8×10^4 s, and those for the supercritical radiation shock are 8.6×10^2, 4.0×10^3, 7.5×10^3, and 1.3×10^4 s. Here, the NR scheme is used, and the time step size is Δt_{fluid}.

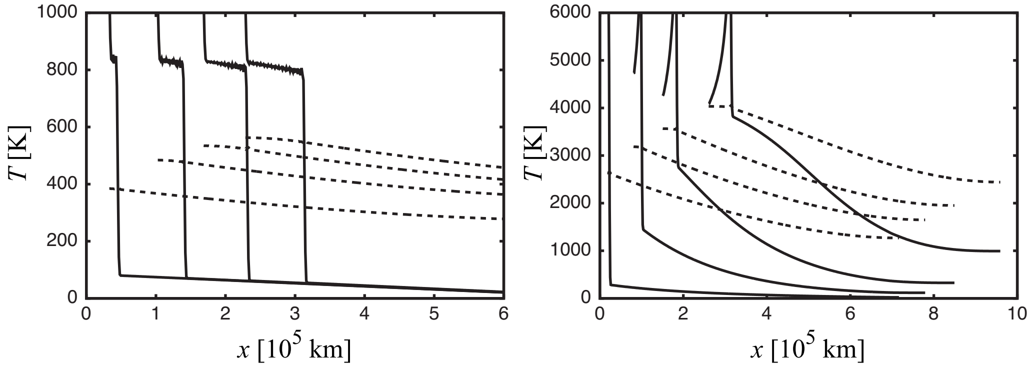

Figure 3.9: Gas (solid lines) and radiation (dashed lines) temperature profiles versus the comoving coordinate x for subcritical (left panel) and supercritical (right panel) radiating shocks. The times are the same as those in figure 3.8, but SOS is used.

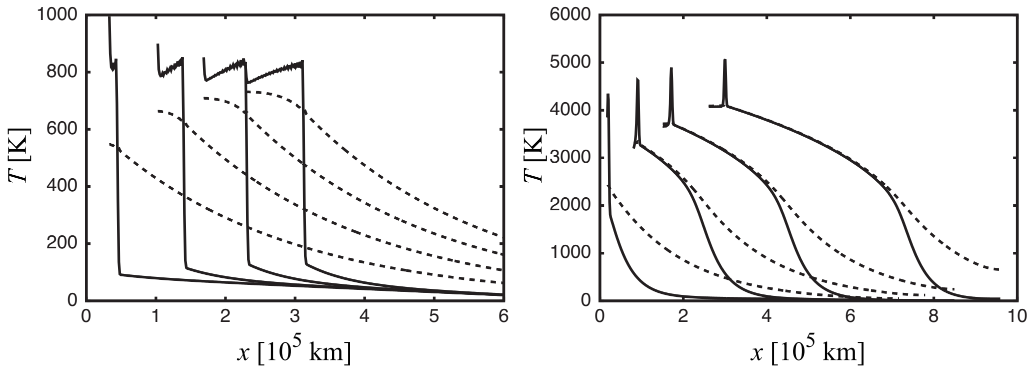

Figure 3.10: Gas (solid curves) and radiation (dashed curves) temperature profiles versus the comoving coordinate x for subcritical (left panel) and supercritical (right panel) radiating shocks. The times are the same as those in figure 3.8; however, SOS is used, and the time step size is $(1/32)\,\Delta t_{\text{fluid}}$.

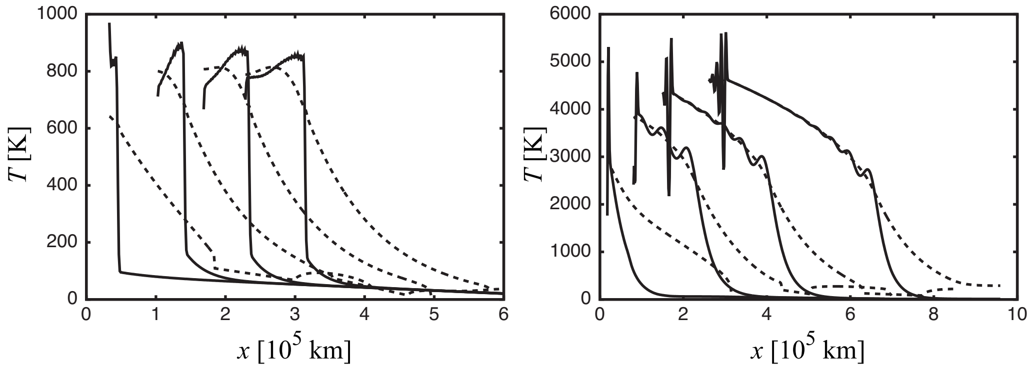

Figure 3.11: Gas (solid curves) and radiation (dashed curves) temperature profiles versus the comoving coordinate x for subcritical (left panel) and supercritical (right panel) radiating shocks. The times are the same as those in figure 3.8, but DROS is used.

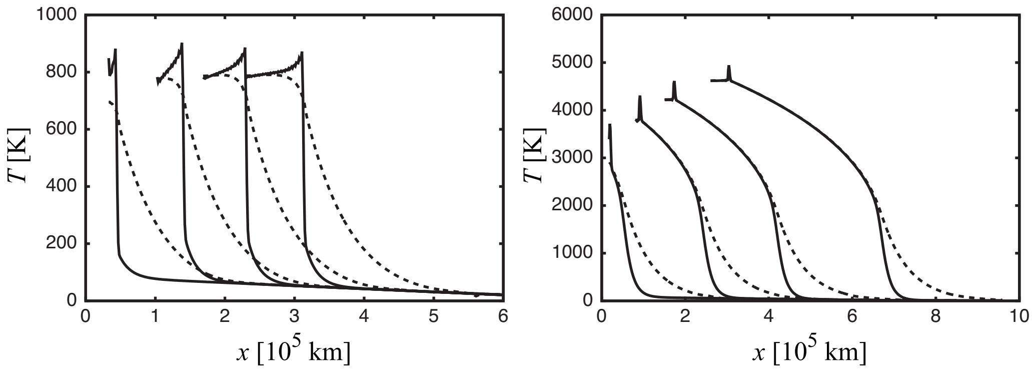

Figure 3.12: Gas (solid curves) and radiation (dashed curves) temperature profiles versus the comoving coordinate x for subcritical (left panel) and supercritical (right panel) radiating shocks. The times are the same as those in figure 3.8; however, DROS is used, and the time step size is $(1/32)\,\Delta t_{\mathrm{fluid}}$.

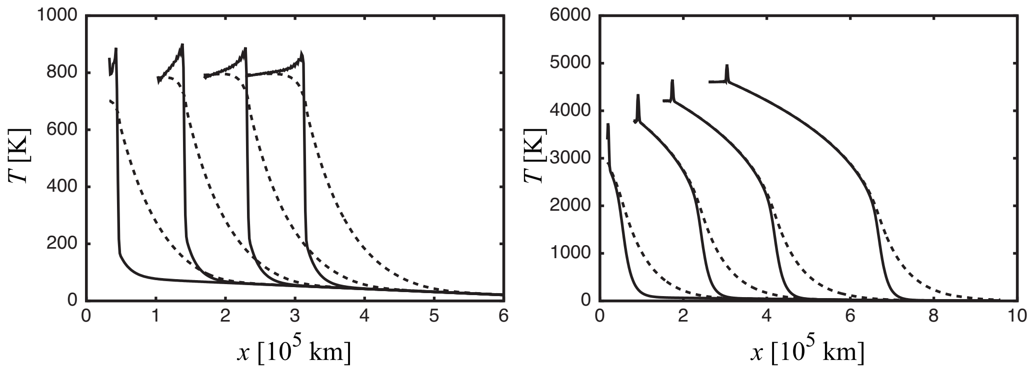

Figure 3.13: Gas (solid curves) and radiation (dashed curves) temperature profiles versus the comoving coordinate x for subcritical (left panel) and supercritical (right panel) radiating shocks. The times are the same as those in figure 3.8, but LIN is used.

3.5 Conclusion of This Chapter

In this study, four schemes for implicitly solving for the nonlinear simultaneous equations in the RHD equations with FLD, the NR method, SOS, DROS, and LIN, were compared from the perspective of the numerical cost performance. We evaluated the "numerical cost" based on whether or not an iteration is needed (and the number, if necessary) and the required size of the time step.

We performed two numerical tests to evaluate the cost. First, we solved the problem of the thermal relaxation mode, regarding the optical thickness and time step size as parameters. To obtain sufficiently correct solutions with the NR scheme, more than several iterations were needed in all cases; moreover, the convergence became worse if the wavelength of the perturbations was optically thin. Although SOS required an unrealistically small time step size to reduce the error due to operator splitting, DROS gave acceptable solutions if Δt was less than $\sim 0.001\Delta t_{\mathrm{fluid}}$. We could obtain correct solutions using LIN using $\Delta t_{\mathrm{fluid}}$. Second, we solved the problem of radiating shock. The NR iteration converged well because the assumed media was sufficiently optically thick; nonetheless, several iterations were needed. Any acceptable results for a practically large Δt was not obtained using SOS, however, correct results were obtained using DROS with $(1/32)\,\Delta t_{\mathrm{fluid}}$. Similar to the first test, LIN gave correct solutions using $\Delta t_{\mathrm{fluid}}$.

In both tests, LIN exhibited the best numerical cost performance. The CFL condition of the fluid automatically satisfied the constraint that the change in the temperature in one time step had to be small. If there are any heating/cooling processes whose time scales are much smaller than the hydrodynamical ones, a sufficiently small Δt seems to be needed, and then the cost of the scheme increases. The NR scheme exhibits comparable performance if the convergence is not a problem. The scheme requires fewer approximations than the other ones; thus, the produced results are more reliable. However, several iterations are needed in all cases, moreover, the convergence becomes much worse if the calculation domain involves extremely optically thin regions (namely, the opacity is small and/or the region is highly resolved). Although SOS is practically useless, DROS can lead to correct solutions with a realistic Δt. In the two tests presented in this paper, DROS is inferior to LIN in numerical cost. However, it can achieve comparably better performance if Δx is smaller (thus, $\Delta t_{\mathrm{fluid}}$ is also smaller). Additionally, DROS is even an operator splitting scheme that is first-order accurate in Δt. A high-order accurate operator splitting scheme based on a similar idea seems to reduce the error. Schemes based on operator splitting are very attractive because they drastically simplify the problems to be solved numerically; thus, their application to RHD algorithms might have significant potential.

	ITERATION	CONSTRAINT ON Δt	RECOMMENDATION (Best: 1)
NR	THICK: SEVERAL THIN: MANY	THICK: FLUID CFL THIN: RADIATION DIFFUSION	THICK: **2** THIN: **3**
SOS	UNNECESSARY	RADIATION DIFFUSION	**4**
DROS	UNNECESSARY	INTERMEDIATE	THICK: **3** THIN: **2**
LIN	UNNECESSARY	FLUID CFL	**1**

Figure 3.14: Our conclusions.

We strongly recommend using LIN to solve general RHD problems. After checking whether or not the results depend on Δt, the LIN approximation might be unsuitable if they do. In this case, either the use of LIN along with a reduction in Δt (i.e., increasing the calculation time) or the use of the other schemes may give a better solution. If the optical thickness of the region is sufficiently large, the alternative choices are DROS followed by the NR method. If the region is optically thin, on the other hand, DROS is better than the NR method. In figure 3.14, we present a table indicating our conclusions briefly.

The problems we want to solve include extremely optically thin region; therefore, we should choose LIN or DROS scheme. Because the implementation of DROS is easier than other schemes, we choose the scheme to perform 2D-RHD calculations in the next chapter. Although, the constraint on the time step size to obtain sufficiently correct solutions using DROS is known just empilically. Moreover, we have to assume a specific flux-limiter, which is not necessarily correct in optically intermediate region, to adopt the FLD approximation. Therefore the reliability of radiation energy flux is not guaranteed. To show the validity of our numerical approach in the problems of gravitationally contracting filaments, we compare the results of one-dimensional problems obtained using FLD with DROS to those obtained using VEF. The ρ_c–T_c evolutionary tracks are shown in figure 3.15. All the parameters are the same, except for the closure relation. Here, the time step size is defined as $(1/32)\Delta t_{\rm fluid}$ to reduce numerical perturbations. Although we do not refer to the detail in the present paper, the convergence of results is confirmed, namely smaller Δt gives almost same evolutionary tracks.

We regard the difference as negligible to investigate the appearance of two-dimensionality and adopt the scheme using FLD with DROS in the next chapter.

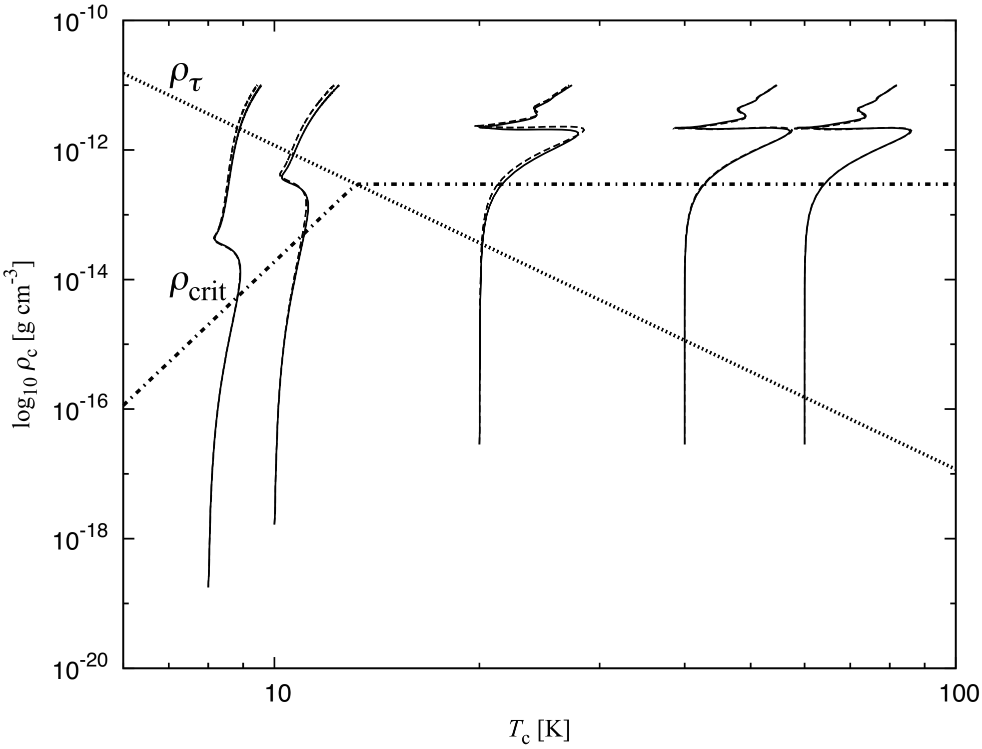

Figure 3.15: Evolutionary tracks of the central density and the central temperature of filamentary clouds heated by the external radiation. Same as Figure 2.9, but for the chosen RHD algorithm. Solid and broken curves denote the results of calculations using FLD and VEF, respectively.

Chapter 4

RADIAL CONTRACTION AND FRAGMENTATION

4.1 Introduction

In the chapter, we investigate the thermodynamic and dynamic evolution of filamentary clouds using one-dimensional RHD calculations. However, from the results, the answer to the question, "when the fragmentation occurs?" In particular, when the isothermality of filaments breaks down in the optically thin regime, the increase of the temperature is much moderate than in the optically thick regime. It is difficult to define the moment of fragmentation. Is it before, during, or after bounce?

In order to answer to the question, we perform two-dimensional RHD calculations with FLD using DROS scheme, which is introduced in chapter 3. Thanks to this scheme that is robust even in optically thin regime, we can efficiently solve the problem of the contraction and fragmentation of filamentary clouds.

4.2 Model

The assumed model is almost identical to one described in chapter 2. The white perturbations are put into the infinite filamentary clouds to induce the fragmentation process. Here, we assume $\beta = 2$, $h^2 = 2$, $\chi_{10} = 0.02\,\mathrm{cm}^2\,\mathrm{g}^{-1}$. The initial temperature is dealt as a parameter, namely $T_{\mathrm{init}} = 8$, 10, 20, 40, and 60 K. We show the results of radiation heated filaments.

4.3 Method

4.3.1 Numerical Scheme

We adopt ZEUS as the gravito-hydroynamics solver and FLD with DROS to obtain the closure relation.

4.3.2 Initial and Boundary Conditions

The two-dimensional cylindrical coordinates assuming axial symmetry are chosen. The imposed boundary conditions are axially periodic, and radially Neumann type (innermost) and Dirichlet type (outermost). The size of calculating area, axially $L_{\rm z}$ and radially $L_{\rm r}$, is determined semi-empirically as follows. The size of $L_{\rm z}$ is $8\,H_{\rm crit}$ ($T_{\rm init} < 13.3$K) and $32\,H_{\rm crit}$ ($T_{\rm init} > 13.3$K) to resolve the most unstable mode of fragmentation sufficiently, where $H_{\rm crit}$ is the scale height represented by equation (2.3), evaluated by the density at which the isothermality breakdown (see chapter 2). The size of $L_{\rm r}$ is four times larger than the initial scale height. The number of grids along the axial direction, $n_{\rm z}$, is 64. The number of grids along the radial direction, $n_{\rm r}$, is 200. While the grid interval in the axial direction is constant, in the radial direction is it is increases as $r_i = \epsilon r_{i-1}$ $(i = 1,\, 2,\, 3\cdots)$, where ϵ is a constant and $r_0 = 10^{12}$ cm to resolve the typical size of fragments. It is ascertained that the spatial resolution is sufficient to reproduce the Jeans instability without any artificial fragmentations (e.g., Truelove et al., 1997). Radiation energy density is fixed at outer boundary independently of time and place: here $E = aT_{\rm init}^4 = aT_B^4$.

In our new FLD algorithm that is based on Douglas-Rachford operator-splitting scheme, the convergence of calculations on the size of time step Δt is obtained only by the empirical approach. In the present work, we define the size of time step as $\Delta t_{\rm CFL}/32$, where $\Delta t_{\rm CFL}$ is the time step derived from the CFL condition of fluid in ZEUS-2D (Stone & Norman, 1992, see).

As initial conditions, unless particularly noted, we use following value,

$$\rho_{\rm c,init} = 10^{-4}\rho_{\rm crit}, \tag{4.1}$$

$$T_{\rm init} = 8, 10, 20, 40, \text{ and } 60\,{\rm K}, \tag{4.2}$$

$$h^2 = 2, \tag{4.3}$$

$$\delta\rho = 0.01\rho_{\rm c,init}, \tag{4.4}$$

and

$$\chi_{10} = 0.02\,{\rm g\,cm^{-3}}, \tag{4.5}$$

where $\rho_{\rm c,init}$ is the initial central density, $T_{\rm init}$ is the initial temperature $\delta\rho$ is the amplitude of the initial perturbation on density, and χ_{10} is the absolute value of the mean mass opacity when $T = 10\,{\rm K}$, respectively.

4.4 Results

To quantify when two-dimensionality appears, it is useful to apply Fourier analysis to the perturbations of the axial central density. The components of the discrete complex Fourier transform of the density at the axis of filaments are defined by

$$C_0 \equiv \frac{1}{n_{\rm z}} \sum_{n=0}^{n_{\rm z}-1} \rho_{\rm n}, \tag{4.6}$$

and for $k \neq 0$

$$C_{\rm k} \equiv \left| \frac{2}{n_{\rm z}} \sum_{n=0}^{n_{\rm z}-1} \rho_{\rm n} {\rm exp}\left(-2\pi kni/n_{\rm z}\right) \right|, \tag{4.7}$$

where $\rho_{\rm k}$ is the density at $r = 0$, $z = -L_{\rm z}/2 + L_{\rm z}n/n_{\rm z}$. Here k is the wave number of a mode, which is defined as L_k/λ, where λ is the wave length of the mode. Because there is no clear criterion as "appearance of two-dimensionality", namely fragmentation, we adopt somewhat arbitrary ones in order to define the appearance of two-dimensionality. Here $|C_{\rm max}/C_0| = 0.01\,{\rm and}\,0.1$ are chosen, where $C_{\rm max}$ and C_0 is the complex Fourier constants, which correspond to the mode that has the largest amplitude and mean central density, respectively. Hereafter, we call the density at which the perturbation exceeds one of two arbitrary criterion $\rho_{\rm frag}$.

The graphs, which represent the relation between $C_{\rm k}$ and the wave number $L_{\rm z}/\lambda$, are shown in figures 4.1 and 4.2, where the initial temperature is 10K and 40K respectively. It is shown that one mode, which has an finite wave length, is the most unstable. The fact is consistent to stability analysis (Larson, 1985; Inutsuka & Miyama, 1992).

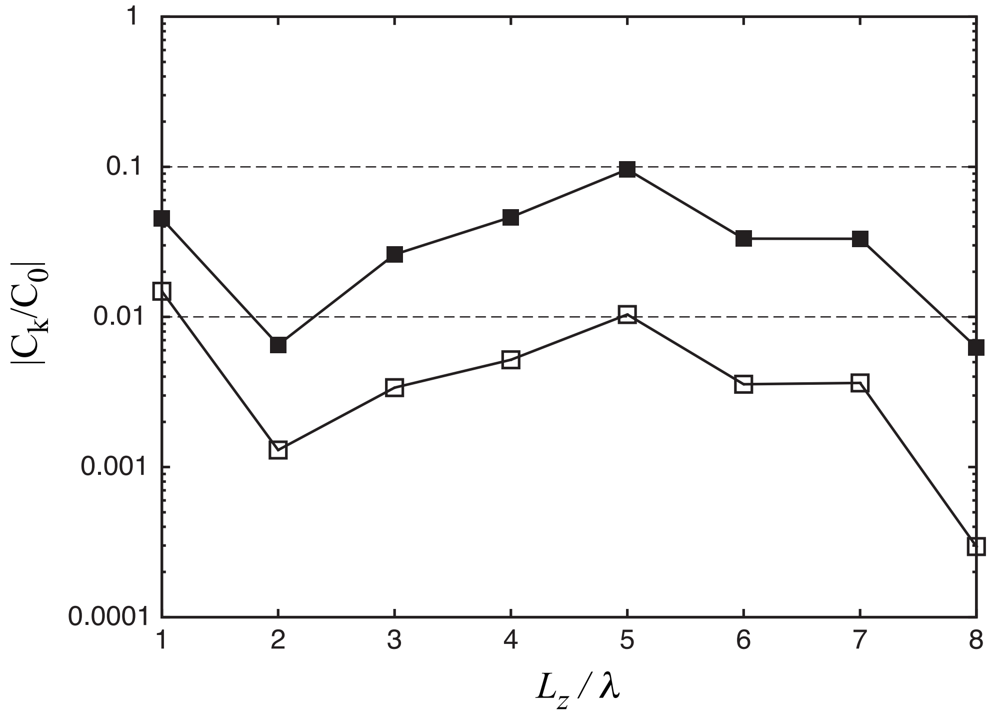

Figure 4.1: Evolution of complex Fourier coefficients. The assumed initial temperature is 10K. The horizontal axis denotes the wave number. The vertical axis denotes the absolute value of complex Fourier coefficients. Open and filled squares represent the snapshots when $|C_{\max}/C_0| = 0.01$ and 0.1.

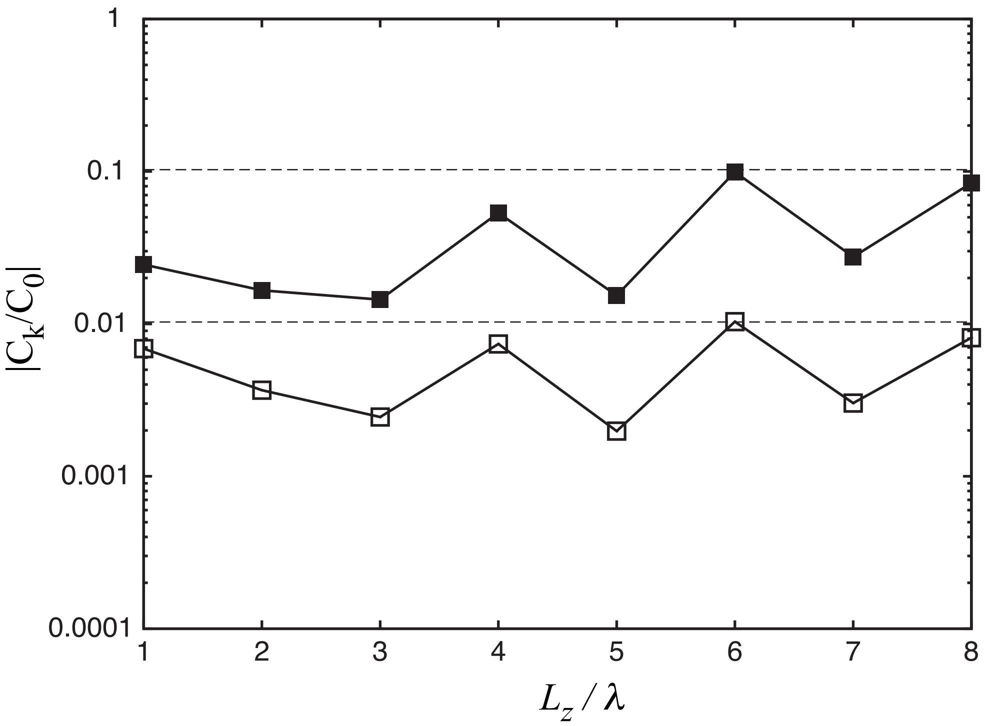

Figure 4.2: Evolution of complex Fourier coefficients. Same as Figure 4.1, except for the initial temperature, which is 40K.

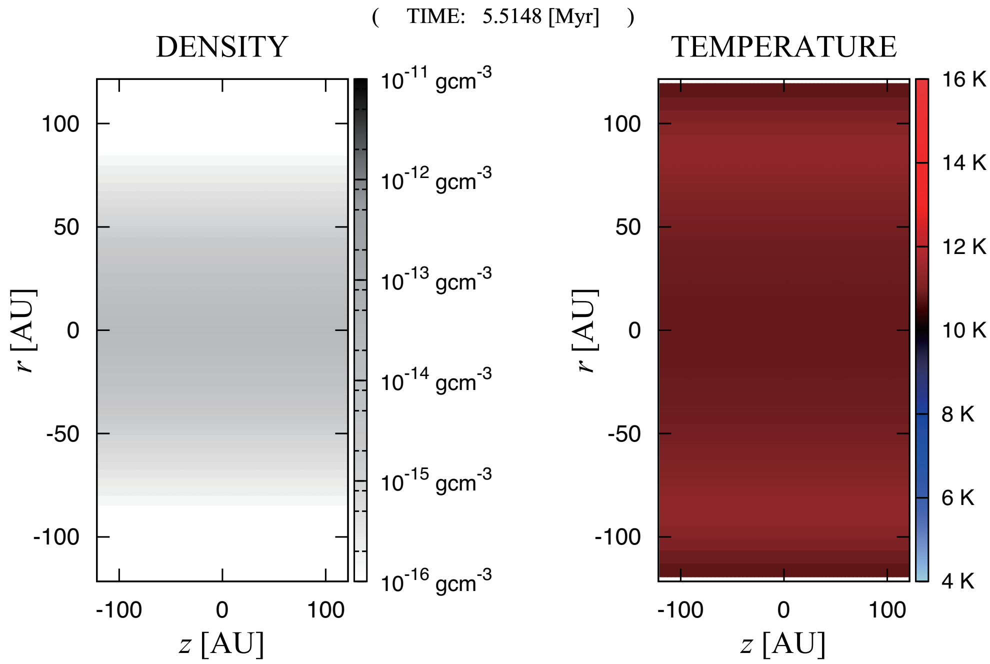

Figure 4.3: Evolution of the density (*left panel*) and the temperature map (*right panel*). The horizontal and the vertical axis are corresponding to the longitudinal and the radial direction of the filament, respectively. The assumed initial temperature is 10K. The snapshot when the mean central density is $\rho_{\rm crit}$ is shown. At this density, the increase of temperature is expected, and actually appears. On the other hand, the indication of the fragmentation is not seen.

The sequences of the density and temperature map in the case of $T_{\rm init} = 10$K are shown in figures 4.3 4.5. The snapshot when the mean central density is $\rho_{\rm crit}$ is shown in figure 4.3. The central region of the filament is warmer than initial condition; however, the contraction continues and the fragmentation does not appear. Snapshots when $|C_{\rm max}/C_0| = 0.01$ and $|C_{\rm max}/C_0| = 0.1$ are shown in 4.4 and 4.5, respectively. Fragmentations, namely the appearance of two-dimensionality can be seen.

The same figures except for initial temperature, namely $T_{\rm init} = 40$K, are shown in figures 4.6 - 4.9. In contrast to the case of $T_{\rm init} = 10$K, a clear bounce because of the breakdown of isothermality occurs.

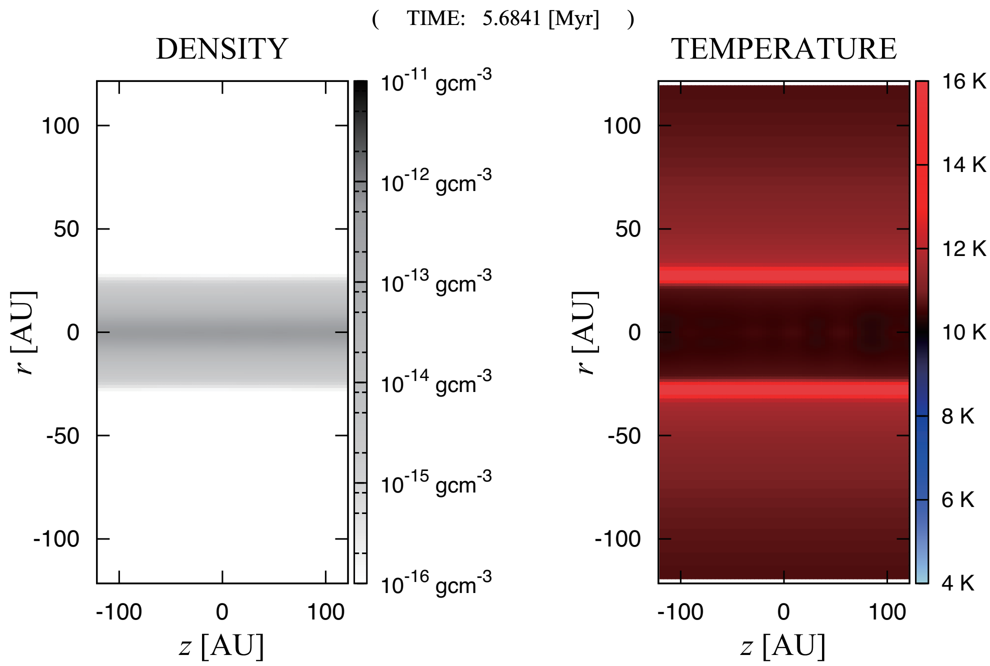

Figure 4.4: Evolution of the density and the temperature map. Same as Figure 4.3, but for the time of the snapshot. In this figure, the map when $|C_{\max}/C_0| = 0.01$ is shown. The fragmenting feature is expected, and shown as the vague colour contour. The shock wave front caused by the bounce appears in the temperature map, which is also shown in 1D calculation (Figure 2.4).

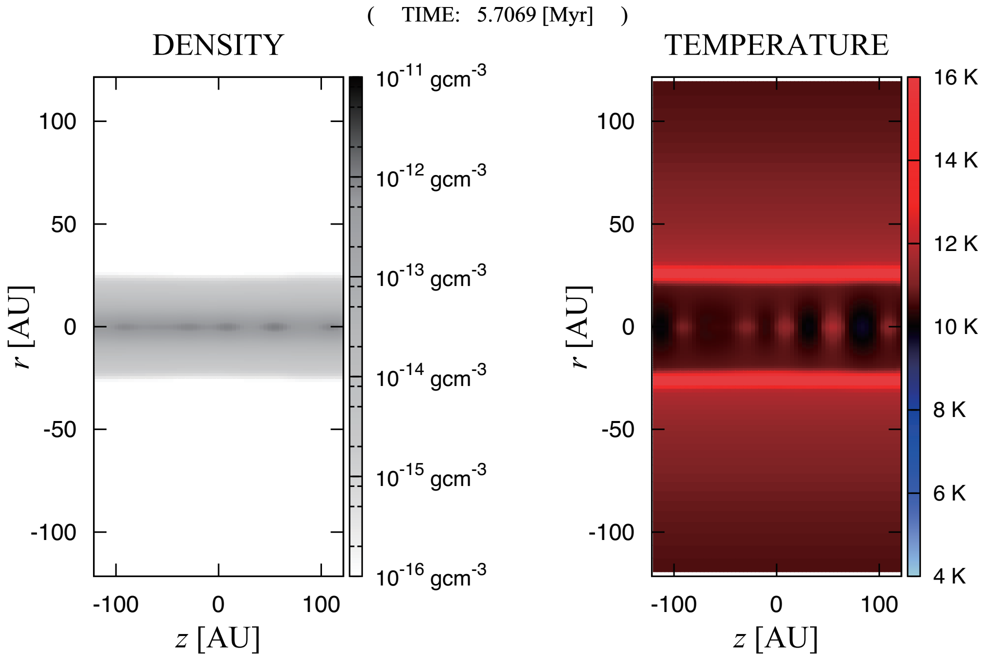

Figure 4.5: Evolution of the density and the temperature map. Same as Figure 4.3, but for the time of the snapshot. In this figure, the map when $|C_{\rm max}/C_0| = 0.1$ is shown. The fragmenting feature is expected, and shown as the clear colour contour. The shock wave front caused by the bounce appears in the temperature map, which is also shown in 1D calculation (Figure 2.4).

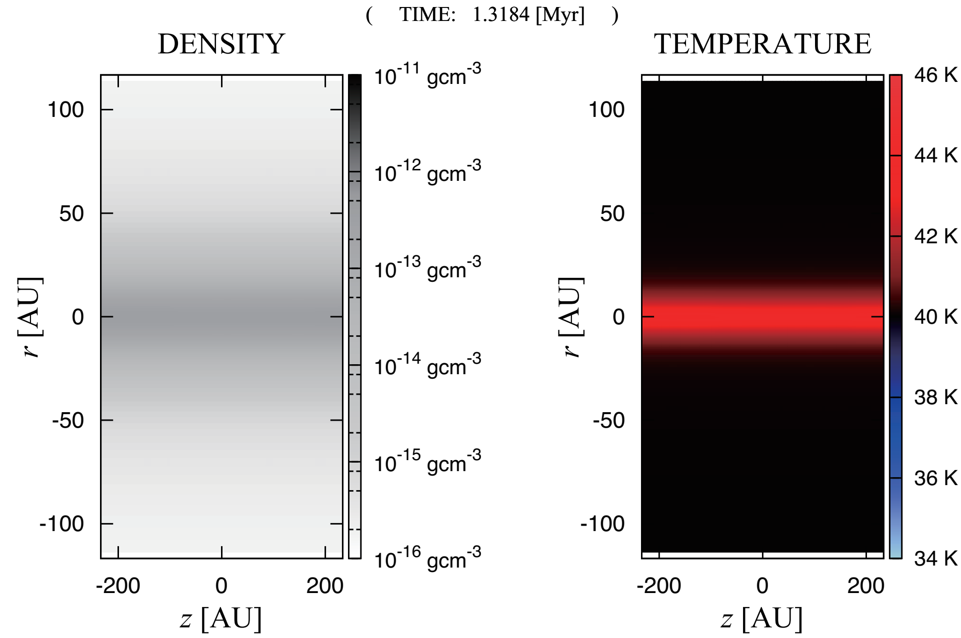

Figure 4.6: Evolution of the density (*left panel*) and the temperature map (*right panel*). The horizontal and the vertical axis are corresponding to the longitudinal and the radial direction of the filament, respectively. The assumed initial temperature is 40 K. The snapshot when the mean central density is $\rho_{\rm crit}$ is shown. Note that the aspect ratio is not identical to Figures 4.3 - 4.5. At this density, the increase of temperature is expected, and actually appears. On the other hand, the indication of the fragmentation is not seen.

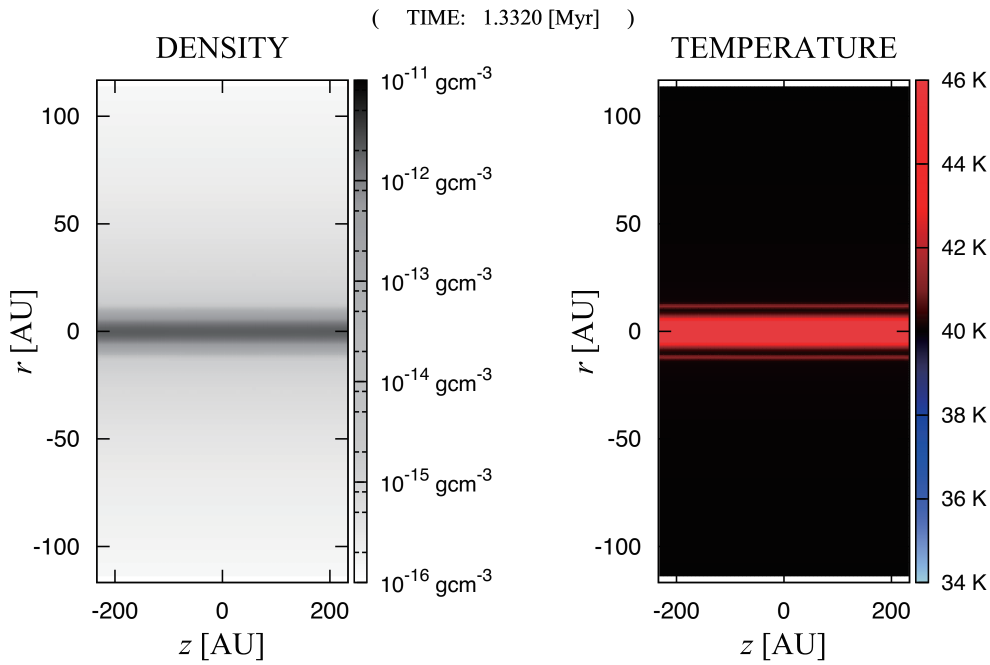

Figure 4.7: Evolution of the density and the temperature map. Same as Figure 4.6, but for the time of the snapshot. In this figure, the map when the expansion just occurs, namely $d\rho/dt|_{r=0} = 0$. The shock wave front caused by the bounce appears in the temperature map, which is also shown in 1D calculation (Figure 2.8).

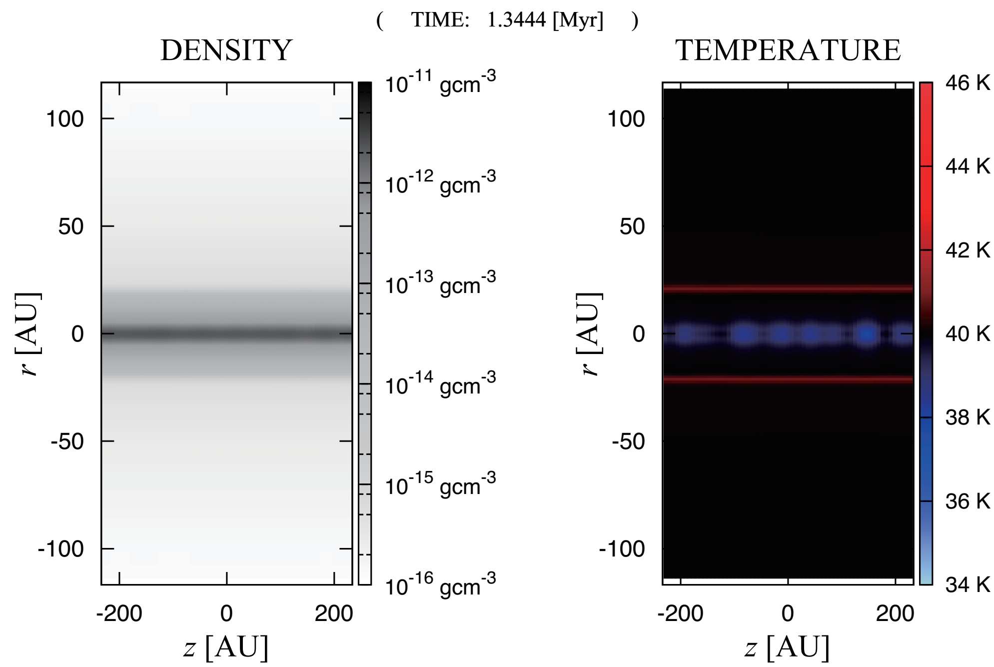

Figure 4.8: Evolution of the density and the temperature map. Same as Figure 4.6, but for the time of the snapshot. In this figure, the map when $|C_{\max}/C_0| = 0.01$ is shown. The fragmenting feature is expected, and shown as the vague colour contour. The shock wave front caused by the bounce also appears in the temperature map. Contrary to the case of 10K, because of the expansion, there is the region in which the temperature is lower than the initial value. The feature is also seen in 1D calculation (Figure 2.8).

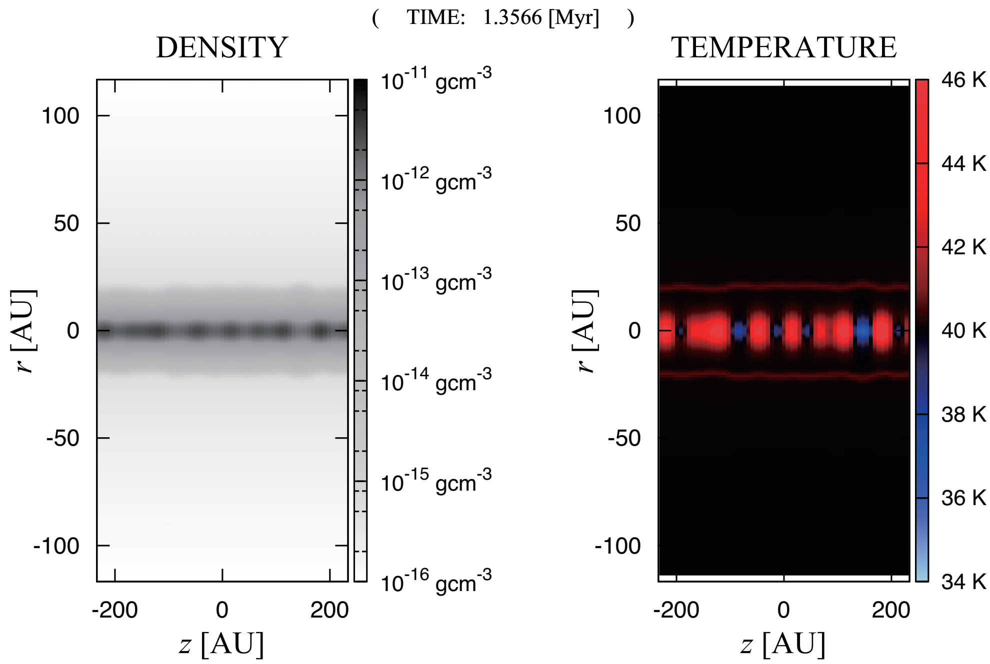

Figure 4.9: Evolution of the density and the temperature map. Same as Figure 4.6, but for the time of the snapshot. In this figure, the map when $|C_{\rm max}/C_0| = 0.1$ is shown. The fragmenting feature is expected, and shown as the clear colour contour.

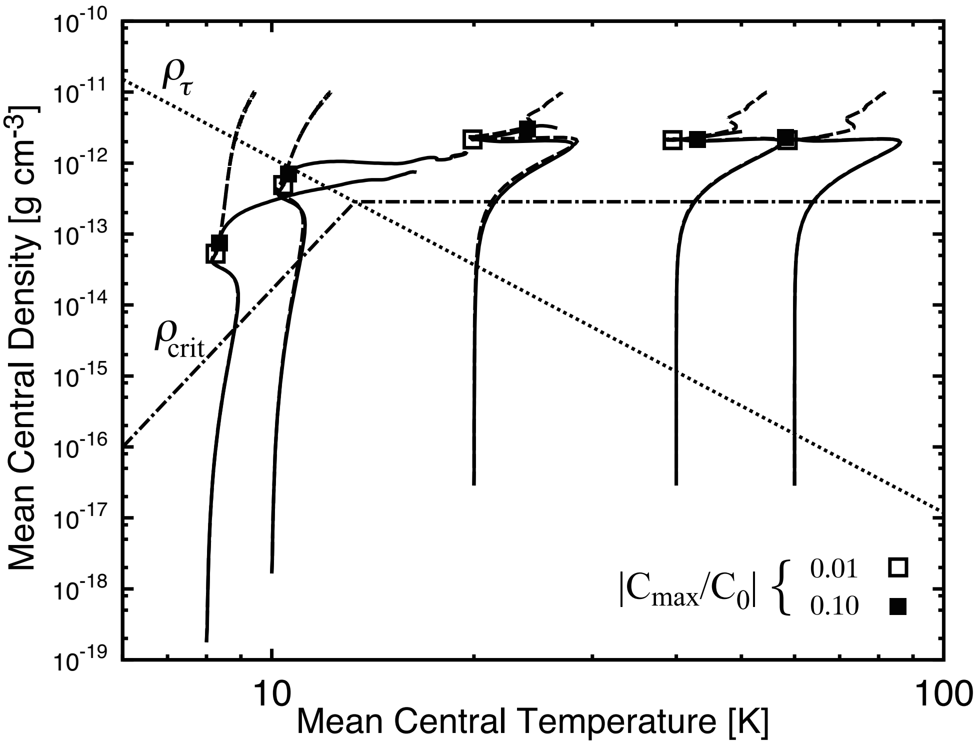

Figure 4.10: Evolution tracks of the mean central density and the mean central temperature of filamentary clouds. White and black squares denote the points $(T_{\rm frag}, \rho_{\rm frag})$, when $|C_{\rm max}/C_0| = 0.01$ and 0.1. Solid and dashed curves represent the tracks obtained by our 2D and 1D simulations, respectively.

In figure 4.10, evolution tracks of the mean central density and the mean central temperature are plotted. It is seen that there is non-negligible difference between $\rho_{\rm frag}$ and $\rho_{\rm crit}$. Figure 4.10 also shows the tracks of our 1D calculation. The junction at which the tracks of 2D calculation depart from ones of 1D suggests that $|{\rm C}_{\rm max}/{\rm C}_0| = 0.1$ is more appropriate than 0.01 as the criterion of the appearance of two-dimensionality.

To directly compare the results to the analytically estimated the mass of fragments (see chapter 2), we substitute $\rho_{\rm frag}$ into the equation (2.40) and the values are shown in figure 4.11. The minimal value reaches at least several Jupiter mass. The difference from the estimated one using $\rho_{\rm crit}$ is not negligible.

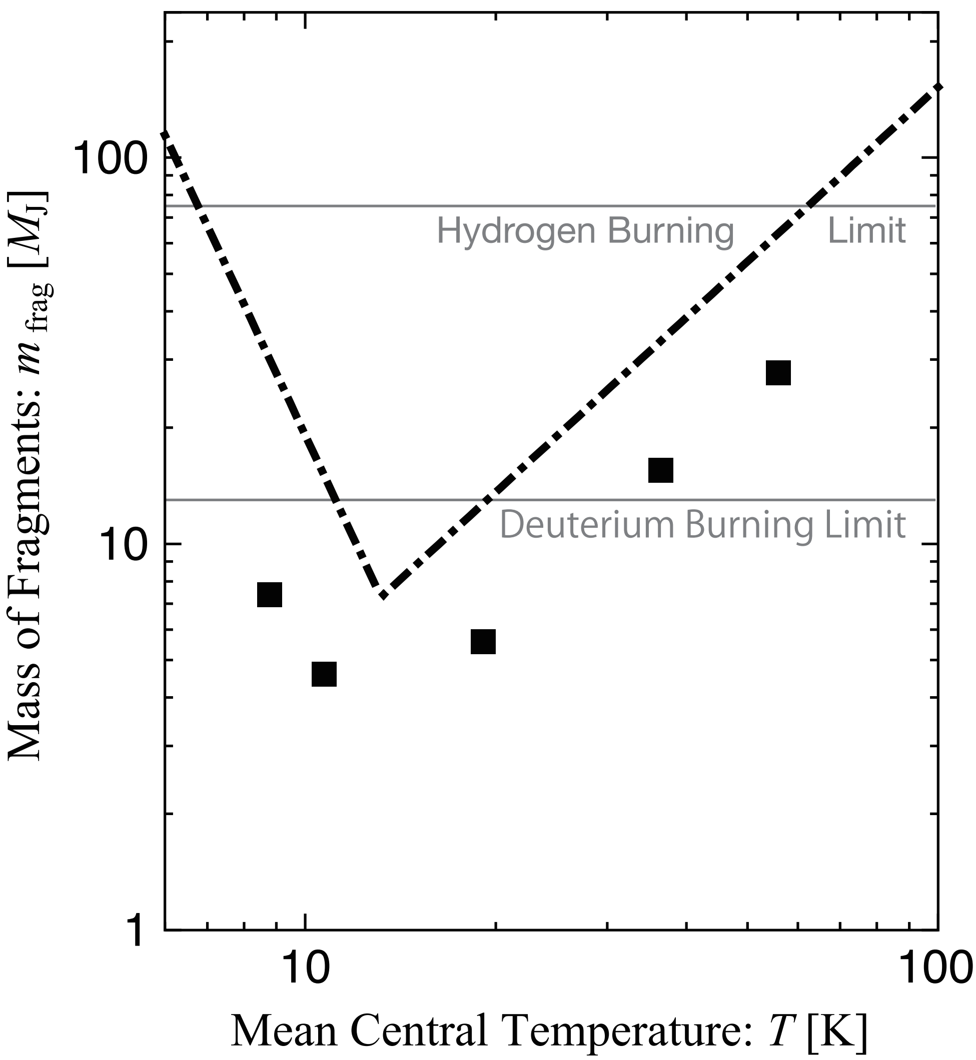

Figure 4.11: Estimated mass of fragments. The horizontal axis represents the initial central temperature and the vertical axis means the estimated mass. The dot-dashed line and squares are same to figure 4.10. Masses that correspond to the hydrogen burning limit and the deuterium burning limit are shown by horizontal lines, respectively.

4.5 Discussion

As Low Mass Object Formation Process

Our 2D RHD calculations uncover the fragmentation processes in detail. The filament, whose initial temperature is higher than T_s, fragments during the bounce. On the other hand, the filaments whose initial temperature is lower than T_s, continues the contraction during the bounce without fragmentation. And then, namely after the bounce, the appearance of fragmentation occurs. This fact indicates that the previous understanding, in which $\rho_{\rm crit}$ is the density at which fragmentation occurs, overestimates the mass of fragments. Although the parameter we assumed is limited, the value is typical one in realistic star formation regions; thus, this result should have important meanings. The fact that $\rho_{\rm crit} < \rho_{\rm frag}$ should be noted to define the appropriate initial conditions to investigate the fragmentation and the processes after that.

The purpose of the present work is not to understand the formation process of any specific objects. However, essentially, the fragments correspond so-called first hydrostatic cores (Larson, 1969; Masunaga et al., 1998). If the star formation process is started from the ideal initial condition assumed in the present paper, the first core can be formed along filamentary clouds. Because the life time of the cores is very short, it is difficult to find them in filamentary clouds, even if they actually exist. However, recent observations with ALMA are finding such rare objects. Tokuda et al. (2014) reported ALMA and Spitzer observations toward MC27 or L1521F, which is considered to be very close to the first core phase. Their mass are about Jupiter mass, the interval is several hundred AU, and there are several cores with an arc-like structure, which is considered as the remnant of the parent filament. The scale of the mass and the interval is very similar to the results of our calculations; thus, to understand the origin of the observed structure, the insight of the fragmentation process we have revealed in detail may be utilized.

Again, the fragments formed in the calculations have several Jupiter mass. The magnetic field, the turbulence, and the rotation, which is ignored in the present paper, would prevent the filaments from the contraction. These factors inhibit the filaments from the radial contraction; thus, they should increase the mass of fragments. The magnetic field and the turbulence also reduce the mass of fragments as the bipolar outflow, binary formation, end so forth. Nevertheless, the mass loss due to these processes do not significantly decrease the mass of cores (e.g., $\sim 50\%$, for binary formation (Machida et al., 2009)); thus, the eventual mass might be comparable to those of fragments. Additionally, the mass accretion after first core formation is less effective than the spherical collapse. If we assume the spherical cloud as initial condition, the large part of mass is finally accreted into the central core. On the other hand, if we assume the filamentary cloud, a lot of cores are formed along the axis and the mass of the parental cloud is divided into respective cores. In this meaning, we may regard the fragmentation process of filamentary clouds as the process that forms a larger number of low mass cores than spherical ones.

On the other hand, faint objects have become detectable thanks to the improvement of observational technology. Recent observations tell us that the detected mass of low-mass objects is as low as about $0.01\,M_{\odot}$ (e.g., Luhman, 2012). For example, the mass of an extremely red object is estimated to be about $0.007M_{\odot}$ (Liu et al., 2013), which is similar to the minimum fragment mass obtained in previous work (Masunaga & Inutsuka, 1999). A pre-brown dwarf object is also identified, and its mass is estimated to be about $0.02M_{\odot}$ (André et al., 2012). Although it is difficult to say clearly something about the minimum mass of objects formed through the gravitational collapse of clouds based on observational data, masses of objects observed so far seem to be consistent with their consideration. Additionally, Sumi et al. (2011) reported the discovery of a population of unbound or distant Jupiter-mass objects, which are almost twice as common as main-sequence stars, based on gravitational microlensing survey observations. They guess the abrupt change in the mass function favours the idea that their formation process is different from that of stars and brown dwarfs and they formed in proto-planetary disk. However, based on our calculations, a lot of small-mass objects can be formed along a filament from molecular clouds directly. The insights we proposed in the present paper suggest the another way to produce a number of Jupiter mass objects.

Influence of Magnetic Field

One of the important but neglected factor is the magnetic field, which penetrates and supports the filamentary structure. The influence of the magnetic field on the dynamical evolution of filaments is determined by the penetrating direction.

The theoretical approach to investigate the impact of the magnetic field on the structure of filaments can be roughly decided into the stability analysis and the numerical calculations. Both kinds of study has uncovered that,

1. the toroidal magnetic fields enhances the fragmentation processes and shorten the fragmentation interval slightly; however, it does not restrain strongly the radial contraction. Thus, the time scale of the radial contraction is shorter than one of the fragmentation, which is same as the case without the magnetic field (Tilley & Pudritz, 2003; Shadmehri, 2005).

2. On the other hand, the longitudinal field strongly supports the structure of filaments and fragments into disk-like structures, which is perpendicular to the axis (Tomisaka, 1996; Nakamura et al., 1999).

3. The magnetic field that laterally penetrates filaments also supports the clouds against radial contraction. However, if filaments have sufficiently large line mass, which corresponds to several times larger value than the thermally critical one, they can gravitationally collapse against the magnetic support (Tomisaka, 2014).

According to observations, the filaments, in which stars are formed, are generally penetrated by the magnetic field with the lateral direction (e.g., Palmeirim et al., 2013). This fact is consistent with the theoretical scenario of the filament formation in the presence of magnetic field (Nagai et al., 1998). Therefore, in star-forming filamentary molecular clouds that have sufficiently high mass, magnetic fields should not prevent them from the radial contraction.

On the other hand, magnetic field that laterally penetrates filaments should not significantly affect the fragmentation process, either. The filaments that can radially contract have larger gravitational energy than magnetic energy. Mass–flux ratio tends to monotonously increase through the radial contraction. Moreover, the time scale of the bipolar diffusion in the fragmenting region is expected to be comparable with free fall time because the typical density $\rho_{\rm frag}$ is sufficiently high (Nakano et al., 2002).

Thus, in the radial contraction and fragmentation processes of typical low-mass star forming filaments, the influence of magnetic field seems not to appear remarkably, and the fragmentation whose time and space scale is similar to ones shown in the present paper is expected.

Chapter 5

SUMMARY

Observations favour a theoretical scenario in which fragmentation of radially contracting filaments takes place due to the breakdown of isothermality. On the other hand, although the filament formation and fragmentation of static filaments have been studied in detail, there is a theoretical gap between the radially contracting filament and the fragmentation. The purpose of this work is to fill and understand the theoretical gap in the context of uncovering the role of radiative transfer.

In the chapter 2, we showed the results of one-dimensional RHD calculations with VEF. As a result, the critical density, which is analytically presented by Masunaga & Inutsuka (1999), and at which the isothermality is expected to break down, is confirmed qualitatively. However, the analysis involves considerable uncertainty to regard the critical density as the density at which fragmentations take place.

Therefore, in order to understand the fragmentation process, two-dimensional RHD calculations are needed. The VEF method is too computationally expensive to perform multi-dimensional RHD calculations; thus we FLD, which is computationally lower-cost, should be chosen. However, However, traditional numerical approach based on Newton-Raphson method has a computational drawback of the stability especially in the optically thin regime. To find out more effective scheme than NR method, four schemes for implicitly solving for the nonlinear simultaneous equations in the RHD equations with FLD, the NR method, SOS, DROS, and LIN, were compared from the perspective of the numerical cost performance. The results are shown in chapter 3.

Based on the results, we chose DROS scheme to perform two-dimensional RHD calculations because of the easiness to be implemented. Using the new scheme, we performed two-dimensional RHD calculations with FLD approximation to investigate the fragmentation process of radially contracting filamentary clouds. As a result, we defined the criteria for judging the appearance of two-dimensionality using the mean central density, which was approximately one order of magnitude higher than previous understandings. In the theoretical gap between the radial contraction and fragmentation process, there was such non-negligible uncertainty. Previously estimated mass of fragments are several times smaller than one, which is obtained by comprehensive RHD simulations.

Our work uncovered the role of radiative transfer in the process of the contraction and the fragmentation of filamentary clouds. Based on the knowledge, the formation process of real astronomical objects, e.g., stars, brown dwarves, planetary mass objects, etc., along the filamentary structures in molecular clouds will be understood in the future works.

APPENDIX A SIMPLIFICATION OF MEAN OPACITY

In the present paper, we assume that $\chi_E = \chi_F = \chi_P$ in order to simplify moment equations, In this appendix, we assess the validity of this assumption and present some drawbacks which should be dealt carefully.

First, in the problems we want to solve, i.e. the gravitationally contracting molecular clouds, we can usually ignore the precise feature of χ_F because the radiation energy distribution is highly uniform and the absolute value of terms including F is substantially smaller than other terms in basic equations. Furthermore, if radiation energy flux cannot be ignored because of optical thinness (e.g. $F \sim cE$ in streaming limit), radiation force hardly affect gas dynamics directly. This fact can be explained using an parameter R defined by Mihalas & Mihalas (1984) as

$$R \equiv \frac{\rho c_v T}{aT^4} \sim 7.1 \left(\frac{\rho}{10^{-18}\,\mathrm{g\,cm^{-3}}}\right) \left(\frac{T}{10\,\mathrm{K}}\right)^{-3}. \tag{5.1}$$

The parameter R represents the ratio of gas inertial energy density to radiation energy density at the thermal equilibrium state. In the range of ρ and T considered in present study, especially when $\rho \sim \rho_{\mathrm{crit}}$, the value of R substantially exceeds unity. The ratio of gas pressure gradient force to radiation force can be estimated as

$$\left|-\frac{1}{\rho}\nabla p\right| \Big/ \left|\frac{\chi_{\mathrm{F}}}{c}\boldsymbol{F}\right| \sim \frac{p}{\rho \chi_{\mathrm{F}} H E} \sim \frac{R}{\tau} \propto \rho^{\frac{1}{2}} T^{-\frac{1}{2}} \tag{5.2}$$

when clouds are optically thin. The value is larger than unity and monotonously increase with increasing density, therefore χ_F does not have important roll in dynamics.

On the other hand, the assumption $\chi_E = \chi_P$ should be assessed carefully. Strictly speaking, these coincide with each other when photons are in thermal equilibrium, namely $E_\nu = B_\nu$. However, this condition might not be valid, e.g., when the temperature of clouds (typically $\sim$ 10K) is established through the equilibrium between ultraviolet radiation heating from surrounding stars and infrared thermal emission from dusts included in clouds. The purpose of this assumption is merely simplifying problems and extracting some essential features. In order to reproduce more realistic thermal evolution processes, more careful treatment might be needed.

Meanwhile, we regard Rosseland mean opacity as $\chi_R \sim \chi_P$ to obtain $\rho_{\rm crit}^{\rm Rad}$ analytically. If specific opacity χ_ν obey the relation $\chi_\nu = \chi_0 \nu^\beta$, Planck mean opacity and Rosseland mean opacity can be written as

$$\chi_P \equiv \frac{\int_0^\infty \chi_\nu B_\nu d\nu}{\int_0^\infty B_\nu d\nu} = \chi_0 \left(\frac{k_B T}{h}\right)^\beta \frac{\int_0^\infty x^{\beta+3}/\left(e^x-1\right)dx}{\int_0^\infty x^3/\left(e^x-1\right)dx} \tag{5.3}$$

and

$$\chi_R^{-1} \equiv \frac{\int_0^\infty \chi_\nu^{-1}\left(\partial B_\nu/\partial T\right)d\nu}{\int_0^\infty \left(\partial B_\nu/\partial T\right)d\nu} = \chi_0^{-1}\left(\frac{k_B T}{h}\right)^{-\beta} \frac{\int_0^\infty x^{4-\beta}/\left(e^x-1\right)^2 dx}{\int_0^\infty x^4/\left(e^x-1\right)^2 dx} \tag{5.4}$$

respectively, where k_B is Boltzmann constant. Therefore the ratio of χ_P to χ_R can be easily calculated using some specific values of the Riemann zeta function. The value is 50/21 if $\beta = 2$; thus, our analysis assuming $\chi_R \sim \chi_P$, which is described in Chapter 2, is valid. On the other hand, because the thermal relaxation time scale can be affected by the approximation, the results obtained through RHD calculations with FLD should be analyzed carefully.

APPENDIX B DEPENDENCE ON RADIAL SPATIAL RESOLUTION

In this section, the dependence of our numerical results on the radial spatial resolution is shown. In the present paper, to resolve scale height both at $\rho_c = \rho_{\text{crit}}$

$$H_{\text{crit}} = H(\rho_{\text{crit}}, T_{\text{init}}) = \begin{cases} H_s \left(\frac{T_{\text{init}}}{T_s}\right)^{\frac{1}{2}} & \text{for } T_{\text{init}} \leq T_s, \\ H_s \left(\frac{T_{\text{init}}}{T_s}\right)^{-\frac{9}{2}} & \text{for } T_{\text{init}} \geq T_s, \end{cases} \tag{5.5}$$

where

$$H_s \equiv \left(\frac{2RT_{\text{s}}}{\pi G \rho_s \mu}\right)^{\frac{1}{2}} = 4.0 \times 10^{14}\text{cm} \tag{5.6}$$

and at $\rho_c = \rho_{\text{init}} = 10^{-4}\rho_{\text{crit}}$

$$H_{\text{init}} = H(\rho_{\text{init}}, T_{\text{init}}) = 100 H_{\text{crit}} \tag{5.7}$$

sufficiently, the interval of grid is determined using a geometrical progression. The minimum interval is chosen as 10^{12} cm at center and total calculation area is $10hH_{\text{init}}$; therefore, a remaining free parameter to determine grid interval is the number of grids. We check dependence of results on number of grids focusing on radial profile evolution and critical density.

Dependence of the profile evolution on the number of grids are shown in figure B.1. We can see that in order to resolve the shock wave more than ~ 200 grids are needed.

On the other hand, in figure B.2, evolution tracks of central temperature and central density with various number of grids are shown. We can see that more than 200 grids is needed to make results well converge. Note that, the spatial resolution does not affect on the density at which temperature increase steeply ("critical density" reproduced by calculations), even if only 50 grids are settled.

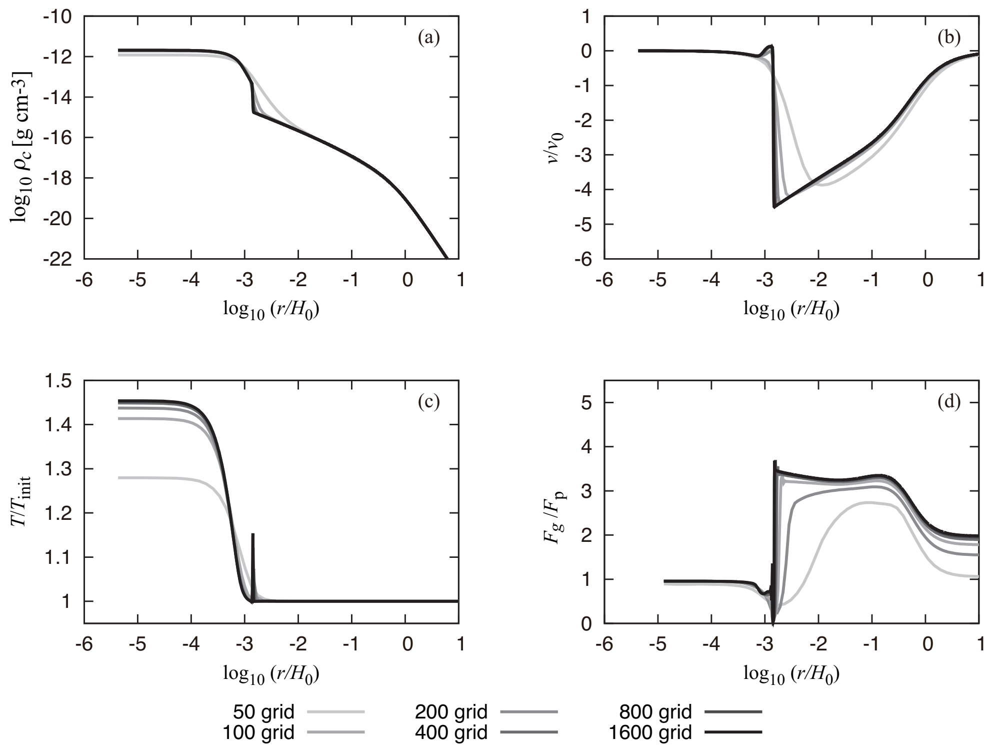

Figure B.1: Radial profile of some physical quantities. Thicker lines represent higher-resolution. See also the legend of figure 2.4.

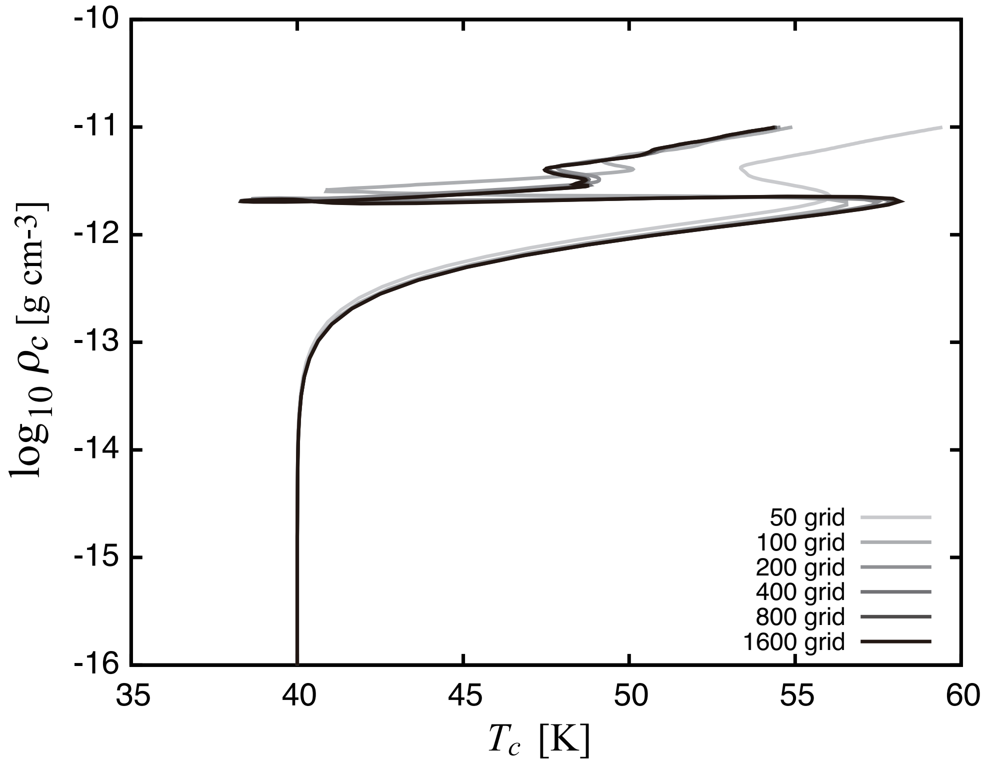

Figure B.2: Evolution tracks of filamentary clouds heated by the external radiation. The initial central temperature of the clouds is 40K. Thicker lines represent higher-resolution. See also the legend in figure 2.9.

APPENDIX C RADIATION TRANSFER TEST (VEF)

In this section, results of a test problem that is used to asses the accuracy of the radiation transfer solver, which is used in the VEF algorithm used in chapter 2. Through this test, it is shown that azimuthal difference on tangent planes are adequately performed therefore Eddington factor is calculated correctly.

Consider that an axisymmetric, extremely optically thick, and uniform cylinder that has unit diameter is in vacuum. Assuming such a situation, we can analytically obtain the rr element of Eddington factor tensor at a point r from the center of cylinder;

$$f_{rr} = \begin{cases} \frac{1}{3}\left[1 + \xi(1-\xi^2)^{\frac{1}{2}}/\sin^{-1}\xi\right] & \text{for } 0 < \xi \leq 1 \\ \frac{1}{3} & \text{for } 1 < \xi \end{cases} \tag{5.8}$$

where

$$\xi = \frac{1}{r}. \tag{5.9}$$

Comparing this analytical solution, a numerical result using our Radiation Transfer Solver is shown in figure C.1. Numerical results show good agreements with analytical ones.

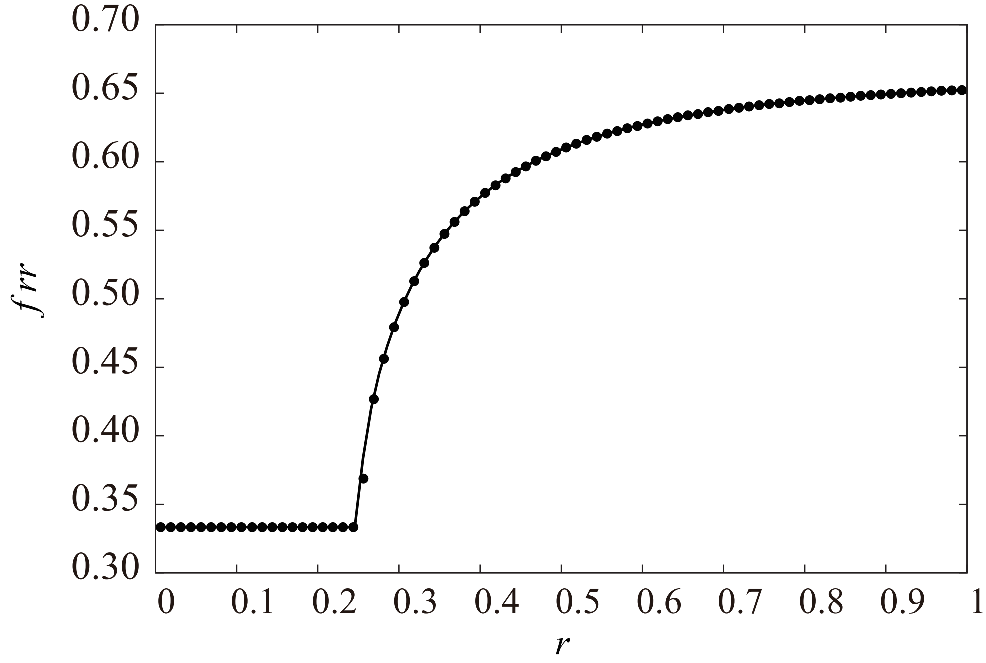

Figure C.1: Radial profile of f_{rr}. The solid curve corresponds to the analytical solution and filled circles denote numerical solutions. The number of grids is 80 and the interval is uniform.

APPENDIX D
MOMENT EQUATION SOLVER TEST (VEF)

It is needed for our VEF calculations to obtain the Eddington factor tensor correctly in cylindrical geometry. In order to show that moment equations are solved correctly using Eddington factor tensor obtained in radiation transfer solver, "thermal relaxation mode" (Unno & Spiegel, 1966) is reproduced numerically. We assume that the material is static and the density is homogeneous. Small fluctuations that has a pattern of the zeroth order Bessel function is added into gas temperature. It is also assumed that radiation field is in equilibrium with the matter. See also the identical test described in chapter 3.

In this test, we adopt the Eddington approximation. Therefore, relaxation rate is

$$n(k) = \frac{\nu}{1 + 3\left(\rho\chi_0/k\right)^2} \tag{5.10}$$

$$\nu = \frac{16\sigma\rho\chi_0 T_0^3}{\rho c_v}, \tag{5.11}$$

where mass density, opacity, gas temperature, heat capacity at constant volume is $\rho = 1.65\times10^{-14}\,\mathrm{g\,cm^{-3}}$, $\chi_0 = (0.02\,\mathrm{cm^2\,g^{-1}})$, $T_0 = 10\,\mathrm{K}$, and $c_v = R/\{\mu(\gamma-1)\}$, respectively. The numerical results show a good agreement with equation (5.10) in figure D.1.

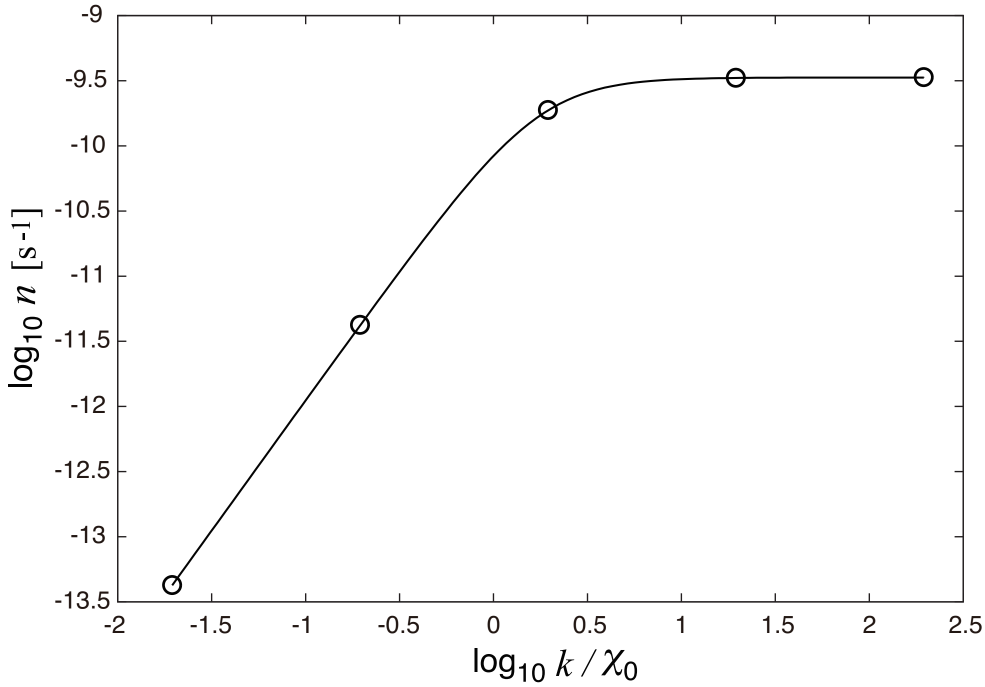

Figure D.1: Dispersion relation for the thermal relaxation mode of the radiation under the Eddington approximation. The solid curve corresponds to the analytical solution and open circles represent numerical solutions.

APPENDIX E CONVERGENCE OF THE NEWTON–RAPHSON ITERATION

The convergence of the NR method is quadratic if the prediction of the solution is sufficiently accurate. However, if not, the convergence is not always guaranteed. In this section, we evaluate the sufficient condition for convergence of the NR method, assuming RHD equations with FLD.

On the basis of the nonlinear simultaneous equations in equations (3.22) and (3.23), we define an iterated function $\boldsymbol{g}(\boldsymbol{x})$ as $\boldsymbol{x}-\mathsf{J}_f^{-1}(\boldsymbol{x})\,\boldsymbol{f}(\boldsymbol{x})$ and $\mathbf{G}(\boldsymbol{x})$ as the Jacobian matrix of $\boldsymbol{g}$. A sufficient condition for convergence is $\|\mathbf{G}\|_\infty < 1$. If Δt is sufficiently small (the criterion is $\sim \Delta x^2/D$), the R.H.S. of equations (3.22) and (3.23) are asymptotically close to the linear equations of e and E, and the NR iteration converges. If Δt is large, on the other hand, it is difficult to evaluate the exact value of $\|\mathbf{G}\|_\infty$. Therefore, we presume that if the relation

$$\mathcal{G} \equiv \max_{a,b,c} \left| \frac{f^{(a)} f''^{(b)}}{\left(f'^{(c)}\right)^2} \right| < 1 \tag{5.12}$$

is established, the iterations converge. Here, a, b, and c mean 1 or 2, and the differentials are with respect to e or E. Using all combinations, we evaluate the value of $\mathcal{G}$. For the sake of simplicity, we explicitly deal with κ. The dependence on the position is ignored, supposing that the values of the terms are represented by the typical ones. We replace $|\boldsymbol{\nabla} \cdot \boldsymbol{F}|$ with $DE/\Delta x^2$. Thus, we obtain

$$\max|f''| = 4\pi\kappa \frac{\partial^2 B}{\partial e^2}\Delta t, \tag{5.13}$$

$$\min|f'| = \min\left[4\pi\kappa \frac{\partial B}{\partial e}\Delta t, c\kappa\Delta t\right], \tag{5.14}$$

and

$$\max|f| = \max\left[4\pi\kappa B\Delta t, c\kappa E\Delta t, \frac{DE}{\Delta x^2}\Delta t\right]. \tag{5.15}$$

Additionally, we assume that $4\pi\kappa B \sim c\kappa E$, $e \gg E$, and the media is optically thin, which is achieved, e.g., in collapsing molecular clouds. Thus, we obtain

$$4\pi\kappa\frac{\partial B}{\partial e}\Delta t \ll 4\pi\kappa\frac{B}{E}\Delta t \sim c\kappa\Delta t, \tag{5.16}$$

and

$$4\pi\kappa B\Delta t \sim c\kappa E\Delta t \ll \frac{DE}{\Delta x^2}\Delta t. \tag{5.17}$$

Substituting equations (5.13)–(5.17) into equation (5.12), we expect convergence if

$$\mathcal{G} \sim \left(\frac{1}{\Delta\tau}\right)^2 \lambda \tag{5.18}$$

is smaller than a unit, where $\Delta\tau \equiv \kappa\Delta x$. The result suggests that the convergence is worse if the optical thickness of a region is smaller, which is consistent with the results presented in chapter 3.

APPENDIX F TRUNCATION ERROR OF LINEARIZATION

To assess the condition for applying the linearization approximation to the Planck function in the thermal relaxation process between matter and radiation, we perform a simple numerical test for the "heating and cooling terms" presented by Turner & Stone (2001).

We consider a static absorbing fluid initially out of thermal balance. Assuming that the internal energy density of the gas is much larger than the radiation energy density, we regard E as constant. The time evolution of e is written as

$$\frac{de}{dt} = -4\pi\kappa B\left(e\right) + c\kappa E. \tag{5.19}$$

A comparison of the results obtained with/without linearizing B is shown in figure F.1. According to Turner & Stone (2001), we assume that $\rho = 10^{-7}\,\mathrm{g\,cm^{-3}}$, $\kappa = 4\times10^{-8}\,\mathrm{cm^{-1}}$, $\mu = 0.6$, $\gamma = 5/3$, and $E = 10^{12}\,\mathrm{erg\,cm^{-3}}$. Initially, $e = 10^{2}$ or $10^{10}\,\mathrm{erg\,cm^{-3}}$, which correspond to $T_{\mathrm{gas}} < T_{\mathrm{rad}}$ and $T_{\mathrm{gas}} > T_{\mathrm{rad}}$, respectively. We regard Δt as a parameter and equal to $10^{-10}\,\mathrm{s}$ for $e = 10^{2}\,\mathrm{erg\,cm^{-3}}$ and $10^{-14}, 10^{-12}, 10^{-10}$, and $10^{-8}\,\mathrm{s}$ for $e = 10^{10}\,\mathrm{erg\,cm^{-3}}$.

If $e = 10^{2}\,\mathrm{erg\,cm^{-3}}$, the numerical solutions with and without linearization are in good agreement with analytical solutions. This is reasonable because the radiation heating $c\kappa E$ is not dependent on B. If $e = 10^{10}\,\mathrm{erg\,cm^{-3}}$, values of Δt smaller than $e/4\pi\kappa B$ $(= 2\times10^{-14}\,\mathrm{s})$ give correct solutions with and without linearization. On the other hand, the solutions obtained with linearization depart from the analytical solutions more remarkably than those without. Without linearization, the gas is rapidly cooled in the first time step and then reaches the analytical solution in several time steps. On the other hand, with linearization, the gas is cooled more slowly, and more than 10 time steps are required to converge to the analytical solution. In other words, a value of Δt that is too large makes the cooling process artificially duller. The additional truncation

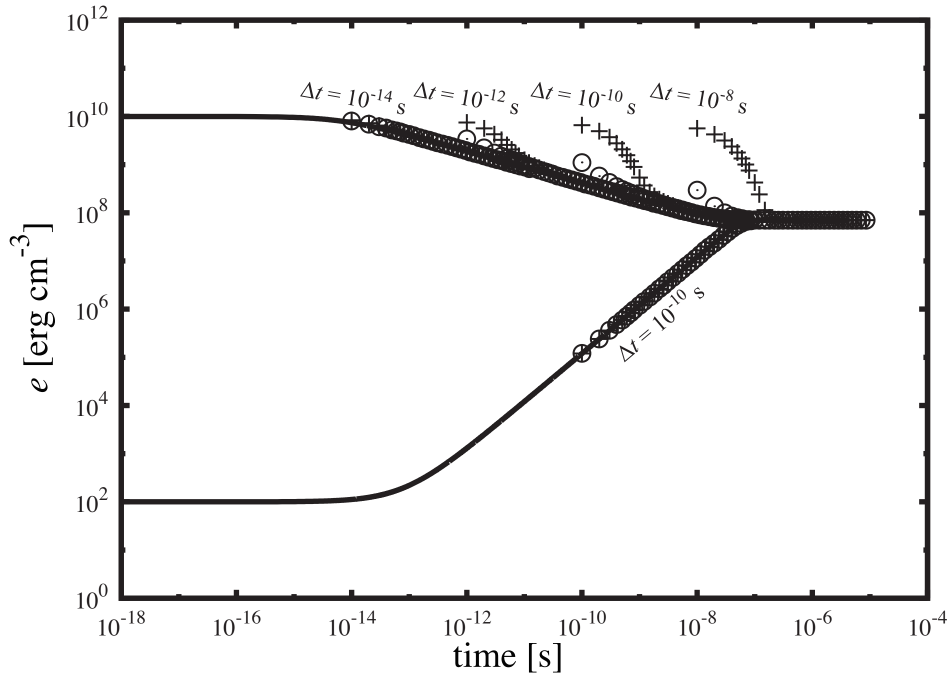

Figure F.1: Time evolution of the internal energy density of the gas. The solid curves represent the analytical solutions, whereas the crosses and open circles indicate the numerical solutions with and without linearizing the Planck function, respectively.

error of linearization seems to cause this difference.

When linearization is used with a large Δt, the influence of such error should be considered carefully.

APPENDIX G
RATIO OF GRAVITATIONAL FORCE TO PRESSURE GRADIENT FORCE

Whether or not the polytropic and self-gravitationally bound gas continues the collapse can be evaluated using the polytrope index γ_p.

We assume the polytropic relation as follows:

$$p \propto \rho^{\gamma_p}. \tag{5.20}$$

Here the model parameter γ_p, which is called polytrope index, is unity when the gas is isothermal, γ when the gas is adiabatic, and the intermediate value when the gas is in the intermediate condition. Consider a gas cloud that collapse one-dimensionally. Describing the radius using R, the dependence of mean density of the gas on R can be written as

$$\rho \propto R^{-d}, \tag{5.21}$$

where d denotes the geometry of the gas. For the case of a sphere $d = 3$ and for the case of a filament $d = 2$.

The dependence of the force of pressure gradient per unit mass on R can be estimated as follows:

$$|F_p| = \left|\frac{1}{\rho}\frac{\partial p}{\partial r}\right| \sim \frac{1}{\rho}\frac{p}{R} \propto R^{d(1-\gamma_p)-1}, \tag{5.22}$$

while the dependence of the gravitational force per unit mass is

$$|F_g| \propto R^{-d+1}. \tag{5.23}$$

Using them, the ratio of these forces around $R = H$ is estimated as

$$\left|\frac{F_g}{F_p}\right| = R^{d(\gamma_p-2)+2}. \tag{5.24}$$

We can define a critical polytrope index as $\gamma_{\rm crit} \equiv (2d-2)/d$. If $\gamma_p < \gamma_{\rm crit}$, gas experiences so-called "run away collapse," namely the rate of forces increases monotonously and infinitely during the contraction. On the other hand, if $\gamma_p > \gamma_{\rm crit}$, the gas cannot continue the gravitational collapse. If $\gamma_p = \gamma_{\rm crit}$, the gas that have sufficient mass can contract roughly keeping the balance of forces.

For the spherical geometry $\gamma_{\rm crit} = 4/3$ and for cylindrical geometry $\gamma_{\rm crit} = 1$. Therefore, the isothermal filament that has sufficient mass to gravitationally collapse continues the contraction infinitely. The fact that whether or not the gas is isothermal determines the dynamics of the clouds is the characteristic feature of filamentary structures.

APPENDIX H
ISOTHERMAL BOUNCE

A filament, which radially contracts with the self-gravity, can bounce keeping its isothermality due to the artificial initial density distribution. In this section, we describe this phenomenon that is called "isothermal bounce" in the present paper.

The inner region of an isothermal filament, which has sufficient mass to make itself gravitationally unstable, results in a self-similar collapse (Inutsuka & Miyama, 1992; Kawachi & Hanawa, 1998). The resultant self-similar collapse is independent of the initial condition. The stage of transition from an artificial initial condition to the physically determined self-similar collapse appears as "bounce." A spherical gas also shows similar behaviour (Tsuribe & Inutsuka, 1999).

The result of a one-dimensional calculation is shown in figures H.1 and H.2. The assumed model is identical to one shown in chapter 2, except for the isothermality. The chosen parameters are as following: $\rho_{\rm c,init} = 10^{-18}\,{\rm g\,cm^{-3}}$, $T = 10\,{\rm K}$, and $h^2 = 2$. After $\sim t_{\rm ff}$ from the initial condition, the density at the center of the filament increases to $\sim 10^7 \rho_{\rm c,init}$, then decreases to $\sim 10^5 \rho_{\rm c,init}$, and finally increases again.

The density at the center increase to $\sim 10^7 \rho_{\rm c,init}$ before isothermal bounce appears because a finite time is needed for sound waves to cross the initial scale height H_0. In order to avoid confusing this artificial bounce with the intrinsic one, in the chapter 2 and 4, we define the initial density at center as $\rho_{\rm c,init} = 10^{-4} \rho_{\rm crit}$. A bounce that appears when $\rho_{\rm c} \sim \rho_{\rm crit}$ is expected to be caused by the breakdown of isothermality.

In order to discriminate two kind of bounces, it is also possible to adopt the much lower initial density, e.g., $\rho_{\rm c,init} = 10^{-8} \rho_{\rm crit}$ (of course such sparse molecular clouds do not exist). The results are shown in figure H.3. In this case, first, an isothermal bounce occurs. And next, after a re-contraction, the bounce because of the breakdown of isothermality occurs.

Both initial conditions can be adopted to reproduce and understand the breakdown of isothermality, the relative timing of these bounces is not important. The reason why we adopt $\rho_{\rm c,init} = 10^{-4}\rho_{\rm crit}$ is just for the sake of expediency, namely to increase space resolution and to reduce computational time.

The isothermal bounce is caused by an artificial initial condition. A more realistic filament, which is formed along a feasible scenario e.g., the gravitational fragmentation of sheet-like clouds (e.g., Miyama et al., 1987a,b; Nagai et al., 1998), should be contracting self-similarly at the early stage of the formation. Such filaments may not experience isothermal bounce, at least when $\rho_{\rm c} \sim \rho_{\rm crit}$.

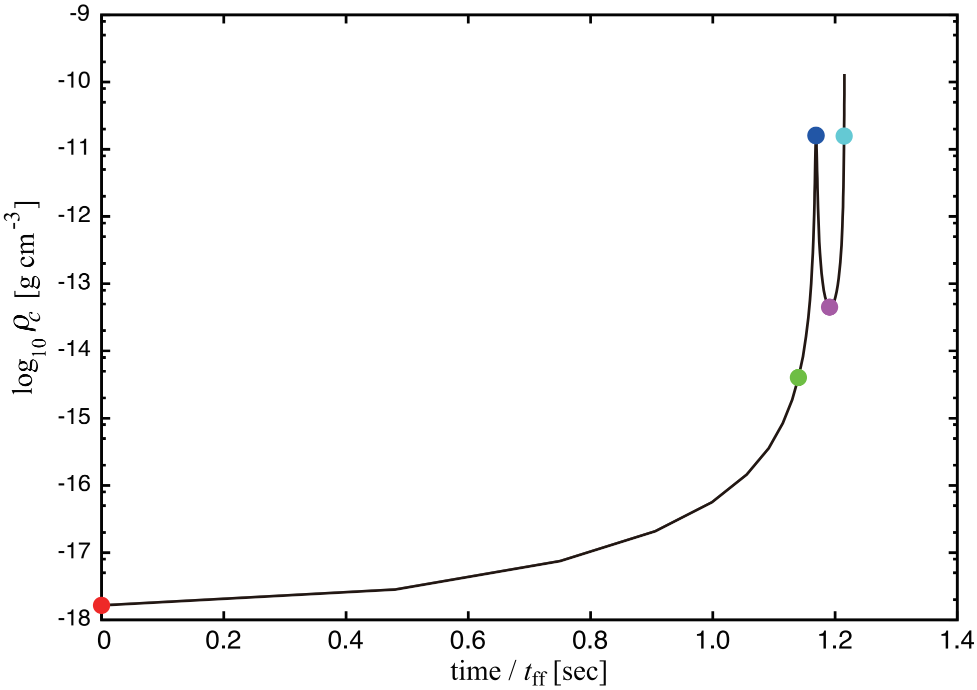

Figure H.1: Result of the isothermal collapse. Color Points indicate the color of curves shown in figure H.2.

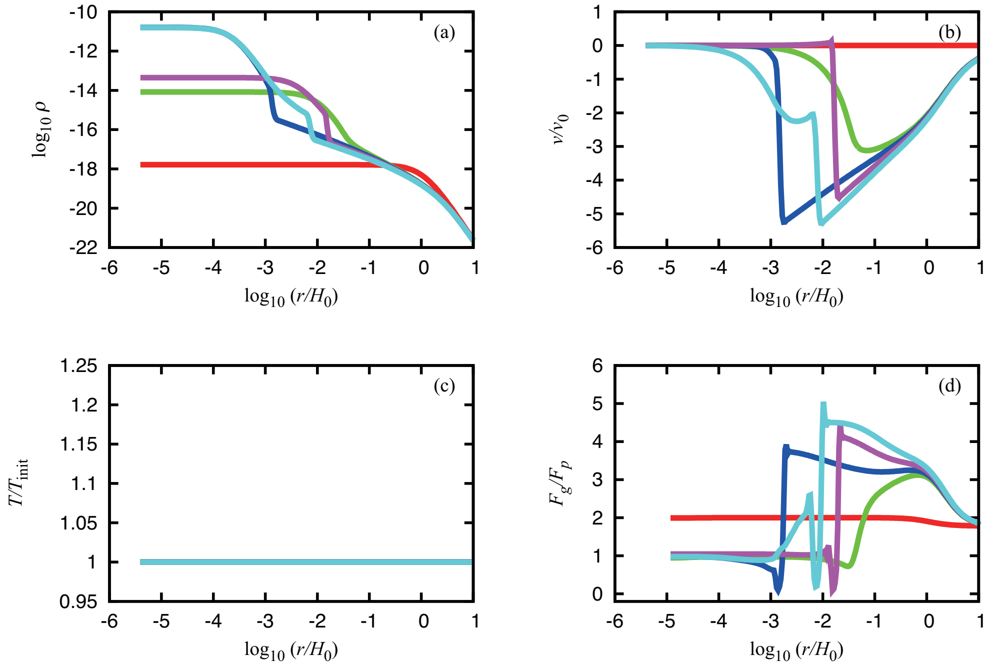

Figure H.2: Result of the isothermal collapse. The color of curves is identical to the color of points shown in figure H.1.

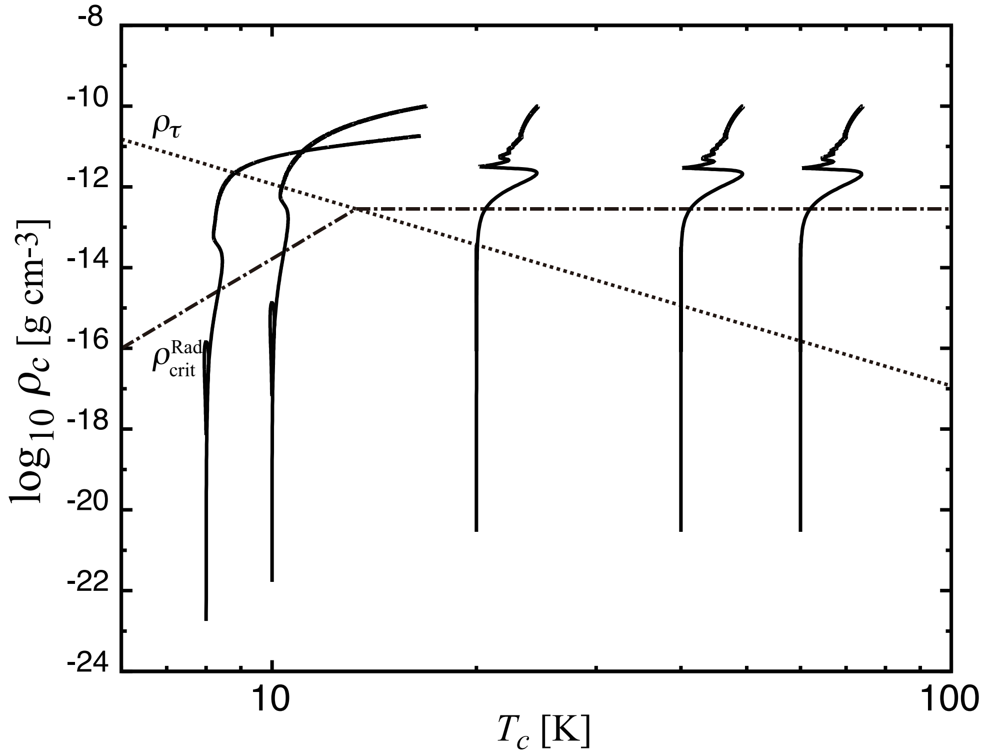

Figure H.3: Evolution tracks of the central density and the central temperature of filamentary clouds heated by external radiation. Initial density at the center is $10^{-8}\rho_{\rm crit}$. See also figure 2.9.

Bibliography

Alme, M. L., & Wilson, J. R. 1974, ApJ, 194, 147

André, P., Di Francesco, J., Ward-Thompson, D., et al. 2014, Protostars and Planets VI, 27

André, P., Ward-Thompson, D., & Greaves, J. 2012, Science, 337, 69

André, P., Men'shchikov, A., Bontemps, S., et al. 2010, A&A, 518, L102

Arzoumanian, D., André, P., Didelon, P., et al. 2011, A&A, 529, L6

Bate, M. R. 2010, MNRAS, 404, L79

—. 2011, MNRAS, 417, 2036

Beckwith, S. V. W., & Sargent, A. I. 1991, ApJ, 381, 250

Bryan, G. L., Norman, M. L., O'Shea, B. W., et al. 2014, ApJS, 211, 19

Ciarlet, P., & Lions, J. 1990, Handbook of Numerical Analysis: Numerical methods for fluids (pt. 3), Handbook of Numerical Analysis (North-Holland)

Commerçon, B., Debout, V., & Teyssier, R. 2014, A&A, 563, A11

Commerçon, B., Teyssier, R., Audit, E., Hennebelle, P., & Chabrier, G. 2011, A&A, 529, A35

Douglas, J., & Rachford, H. H. 1956, Transactions of the American Mathematical Society, 82, 421

Draine, B. T., & Lee, H. M. 1984, ApJ, 285, 89

Dubroca, B., & Feugeas, J.-L. 1999, Comptes Rendus de l'Acad é mie des Sciences - Series I - Mathematics, 329, 915

Ensman, L. 1994, ApJ, 424, 275

Fischera, J., & Martin, P. G. 2012, A&A, 547, A86

Gehman, C. S., Adams, F. C., Fatuzzo, M., & Watkins, R. 1996a, ApJ, 457, 718

Gehman, C. S., Adams, F. C., & Watkins, R. 1996b, ApJ, 472, 673

Gnedin, N. Y., & Abel, T. 2001, New A, 6, 437

Goldsmith, P. F., & Langer, W. D. 1978, ApJ, 222, 881

González, M., Audit, E., & Huynh, P. 2007, A&A, 464, 429

González, M., Vaytet, N., Commerçon, B., & Masson, J. 2015, A&A, 578, A12

Hanawa, T., & Audit, E. 2014, J. Quant. Spec. Radiat. Transf., 145, 9

Hayes, J. C., & Norman, M. L. 2003, ApJS, 147, 197

Hayes, J. C., Norman, M. L., Fiedler, R. A., et al. 2006, ApJS, 165, 188

Hennebelle, P. 2003, A&A, 397, 381

Holden, L., Hoppins, K., Baxter, B., & Fatuzzo, M. 2009, PASP, 121, 485

Iliev, I. T., Ciardi, B., Alvarez, M. A., et al. 2006, MNRAS, 371, 1057

Iliev, I. T., Whalen, D., Mellema, G., et al. 2009, MNRAS, 400, 1283

Inutsuka, S.-I., & Miyama, S. M. 1992, ApJ, 388, 392

Inutsuka, S.-i., & Miyama, S. M. 1997, ApJ, 480, 681

Kawachi, T., & Hanawa, T. 1998, PASJ, 50, 577

Klein, R. I., & Woods, D. T. 1998, ApJ, 497, 777

Kolb, S. M., Stute, M., Kley, W., & Mignone, A. 2013, A&A, 559, A80

Könyves, V., André, P., Men'shchikov, A., et al. 2010, A&A, 518, L106

Koyama, H., & Inutsuka, S.-I. 2000, ApJ, 532, 980

Krumholz, M. R., Klein, R. I., McKee, C. F., & Bolstad, J. 2007, ApJ, 667, 626

Larson, R. B. 1969, MNRAS, 145, 271

—. 1985, MNRAS, 214, 379

Levermore, C. D., & Pomraning, G. C. 1981, ApJ, 248, 321

Lis, D. C., Serabyn, E., Keene, J., et al. 1998, ApJ, 509, 299

Liu, M. C., Magnier, E. A., Deacon, N. R., et al. 2013, ApJ, 777, L20

Luhman, K. L. 2012, ARA&A, 50, 65

Machida, M. N., Inutsuka, S.-i., & Matsumoto, T. 2009, ApJ, 699, L157

Masunaga, H., & Inutsuka, S.-i. 1999, ApJ, 510, 822

—. 2000, ApJ, 531, 350

Masunaga, H., Miyama, S. M., & Inutsuka, S.-i. 1998, ApJ, 495, 346

Matsumoto, T., Hanawa, T., & Nakamura, F. 1997, ApJ, 478, 569

Matsumoto, T., Nakamura, F., & Hanawa, T. 1994, PASJ, 46, 243

Mihalas, D., & Mihalas, B. W. 1984, Foundations of radiation hydrodynamics (Oxford Univ Pr)

Miyake, K., & Nakagawa, Y. 1993, Icarus, 106, 20

—. 1995, ApJ, 441, 361

Miyama, S. M., Narita, S., & Hayashi, C. 1987a, Progress of Theoretical Physics, 78, 1051

—. 1987b, Progress of Theoretical Physics, 78, 1273

Nagai, T., Inutsuka, S.-i., & Miyama, S. M. 1998, ApJ, 506, 306

Nagasawa, M. 1987, Progress of Theoretical Physics, 77, 635

Nakamoto, T., Umemura, M., & Susa, H. 2001, MNRAS, 321, 593

Nakamura, F. 1998, ApJ, 507, L165

Nakamura, F., Hanawa, T., & Nakano, T. 1993, PASJ, 45, 551

Nakamura, F., Matsumoto, T., Hanawa, T., & Tomisaka, K. 1999, ApJ, 510, 274

Nakamura, F., & Umemura, M. 2001, ApJ, 548, 19

Nakano, T., Nishi, R., & Umebayashi, T. 2002, ApJ, 573, 199

Nayakshin, S., Cha, S.-H., & Hobbs, A. 2009, MNRAS, 397, 1314

Ogochi, K. 2000, PhD thesis, University of Tsukuba

Ostriker, J. 1964, ApJ, 140, 1056

Padoan, P., Juvela, M., Goodman, A. A., & Nordlund, Å. 2001, ApJ, 553, 227

Palmeirim, P., André, P., Kirk, J., et al. 2013, A&A, 550, A38

Petkova, M., & Springel, V. 2009, MNRAS, 396, 1383

Pilbratt, G. L., Riedinger, J. R., Passvogel, T., et al. 2010, A&A, 518, L1

Pon, A., Johnstone, D., & Heitsch, F. 2011, ApJ, 740, 88

Rees, M. J. 1976, MNRAS, 176, 483

Reynolds, D. R., Hayes, J. C., Paschos, P., & Norman, M. L. 2009, Journal of Computational Physics, 228, 6833

Shadmehri, M. 2005, MNRAS, 356, 1429

Shadmehri, M., & Ghanbari, J. 2001, Ap&SS, 278, 347

Silk, J. 1977, ApJ, 214, 152

Skinner, M. A., & Ostriker, E. C. 2013, ApJS, 206, 21

Spiegel, E. A. 1957, ApJ, 126, 202

Springel, V. 2005, MNRAS, 364, 1105

Stone, J. M., Mihalas, D., & Norman, M. L. 1992, ApJS, 80, 819

Stone, J. M., & Norman, M. L. 1992, ApJS, 80, 753

Sumi, T., Kamiya, K., Bennett, D. P., et al. 2011, Nature, 473, 349

Teyssier, R. 2002, A&A, 385, 337

Tilley, D. A., & Pudritz, R. E. 2003, ApJ, 593, 426

Tokuda, K., Onishi, T., Saigo, K., et al. 2014, ApJ, 789, L4

Tomida, K., Tomisaka, K., Matsumoto, T., et al. 2013, ApJ, 763, 6

Tomisaka, K. 1995, ApJ, 438, 226

—. 1996, PASJ, 48, 701

—. 2014, ApJ, 785, 24

Truelove, J. K., Klein, R. I., McKee, C. F., et al. 1997, ApJ, 489, L179

Tsuribe, T., & Inutsuka, S.-i. 1999, ApJ, 526, 307

Turner, N. J., & Stone, J. M. 2001, ApJS, 135, 95

Unno, W., & Spiegel, E. A. 1966, PASJ, 18, 85

van de Hulst, H. C. 1957, Light Scattering by Small Particles (Oxford Univ Pr)

Whitehouse, S. C., & Bate, M. R. 2004, MNRAS, 353, 1078

Whitehouse, S. C., Bate, M. R., & Monaghan, J. J. 2005, MNRAS, 364, 1367

Wolfire, M. G., Hollenbach, D., McKee, C. F., Tielens, A. G. G. M., & Bakes, E. L. O. 1995, ApJ, 443, 152

Yang, X., & Yuan, F. 2012, PASJ, 64, 69